

Aus der Neurologischen Klinik und Poliklinik
Klinik der Universität München
Direktor: Prof. Dr. Günter U. Höglinger, FEAN

Bildgebung im
zentralen und peripheren vestibulären System

Dissertation
zum Erwerb des Doktorgrades der Medizin
an der Medizinischen Fakultät
der Ludwig-Maximilians-Universität zu München






vorgelegt von
Emilie-Louis Eva Theresia Kierig
aus
Stuttgart

Jahr
2024

Mit Genehmigung der Medizinischen Fakultät
der Universität München

Berichterstatter:	Prof. Dr. Marianne Dieterich, FANA, FEAN
Mitberichterstatter:	PD Dr. Robert Forbrig, MHBA Prof. Dr. Sophia Stöcklein
Mitbetreuung durch den promovierten Mitarbeiter:	Dr. Valerie Kirsch
Dekan:	Prof. Dr. Thomas Gudermann
Tag der mündlichen Prüfung:	14.03.2024

Affidavit

	LUDWIG- MAXIMILIANS- UNIVERSITÄT MÜNCHEN	Promotionsbüro Medizinische Fakultät	 
Eidesstattliche Versicherung			

Emilie-Louis Eva Theresia Kierig

Name, Vorname

Ich erkläre hiermit an Eides statt, dass ich die vorliegende Dissertation mit dem Titel:

Bildgebung im zentralen und peripheren vestibulären System.....

selbständig verfasst, mich außer der angegebenen keiner weiteren Hilfsmittel bedient und alle Erkenntnisse, die aus dem Schrifttum ganz oder annähernd übernommen sind, als solche kenntlich gemacht und nach ihrer Herkunft unter Bezeichnung der Fundstelle einzeln nachgewiesen habe.

Ich erkläre des Weiteren, dass die hier vorgelegte Dissertation nicht in gleicher oder in ähnlicher Form bei einer anderen Stelle zur Erlangung eines akademischen Grades eingereicht wurde.

München, den 18.03.2024

Ort, Datum

Emilie-Louis Eva Theresia Kierig

Unterschrift Doktorandin bzw. Doktorand

Inhaltsverzeichnis

Affidavit	3
Inhaltsverzeichnis	4
Abkürzungsverzeichnis	5
Publikationsliste	6
Beitrag zu den Publikationen	7
Beitrag zur Publikation I	7
Beitrag zur Publikation II	7
1. Einleitung	8
1.1 Das vestibuläre System	8
1.1.1 Das periphere vestibuläre System	8
1.1.2 Das zentrale vestibuläre System	12
1.1.2.1 Hirnstamm und Thalamus	12
1.1.2.2 Kortex	13
1.2 Vestibularisparoxysmie	14
2. Magnetresonanztomographie	17
2.1 Funktionelle Magnetresonanztomographie	17
2.1.1 BOLD Kontrast	17
2.1.2 Funktionelle Parzellierung mittels Ruhenetzwerken	18
2.2 Strukturelle Magnetresonanztomographie	20
2.2.1 Beurteilung der Nervenintegrität mittels Diffusion Tensor Imaging	20
2.2.2 Darstellung des Endolymphatischen Raums mittels kontrastmittel-verstärktem MRT	21
3. Zusammenfassung	22
4. Abstract	23
5. Publikation I - Handedness-dependent functional organizational patterns within the bilateral vestibular cortical network revealed by fMRI connectivity based parcellation	24
6. Publikation II - Vestibular paroxysmia entails vestibular nerve function, microstructure and endolymphatic space changes linked to root-entry zone neurovascular compression	39
Literaturverzeichnis	59
Abbildungsverzeichnis	66
Danksagung	67

Abkürzungsverzeichnis

ADC	<i>Apparent Diffusion Coefficient</i>
BOLD	<i>Blood Oxygenation Level Dependent</i>
DTI	<i>Diffusion Tensor Imaging</i>
FA	<i>Fractional anisotropy</i>
FLAIR	<i>Fluid-Attenuated Inversion Recovery</i>
fMRT	<i>Funktionelle Magnetresonanztomographie</i>
ICA	<i>Independent Component Analysis</i>
IR	<i>Inversion Recovery</i>
MRT	<i>Magnetresonanztomographie</i>
PIVC	<i>parieto-insulärer vestibulärer Kortex</i>
RSN	<i>resting state network</i>
VOLT	<i>Volumetric Local Thresholding</i>

Publikationsliste

2023 Dieterich M, Hergenroeder T, Boegle R, Gerb J, **Kierig E**, Stöcklein S, Kirsch V. Endolymphatic space is age-dependent. *J Neurol*. 2023 Jan;270(1):71-81. doi: 10.1007/s00415-022-11400-8.

Kierig E, Gerb J, Boegle R, Ertl-Wagner B, Dieterich M, Kirsch V. Vestibular paroxysmia entails vestibular nerve function, microstructure and endolymphatic space changes linked to root-entry zone neurovascular compression. *J Neurol*. 2023 Jan;270(1):82-100. doi: 10.1007/s00415-022-11399-y.

2021 Boegle R, Gerb J, **Kierig E**, Becker-Bense S, Ertl-Wagner B, Dieterich M, Kirsch V. Intravenous Delayed Gadolinium-Enhanced MR Imaging of the Endolymphatic Space: A Methodological Comparative Study. *Front Neurol*. 2021 Apr 22;12:647296. doi: 10.3389/fneur.2021.647296.

2020 Gerb J, Ahmadi SA, **Kierig E**, Ertl-Wagner B, Dieterich M, Kirsch V. VOLT: a novel open-source pipeline for automatic segmentation of endolymphatic space in inner ear MRI. *J Neurol*. 2020 Dec;267(Suppl 1):185-196. doi: 10.1007/s00415-020-10062-8.

2019 Kirsch V, Boegle R, Keeser D, **Kierig E**, Ertl-Wagner B, Brandt T, Dieterich M. Beyond binary parcellation of the vestibular cortex - A dataset. *Data Brief*. 2019 Jan 22;23:103666. doi: 10.1016/j.dib.2019.01.014.

2018 Kirsch V, Boegle R, Keeser D, **Kierig E**, Ertl-Wagner B, Brandt T, Dieterich M. Handedness-dependent functional organizational patterns within the bilateral vestibular cortical network revealed by fMRI connectivity based parcellation. *Neuroimage*. 2018 Sep;178:224-237. doi: 10.1016/j.neuroimage.2018.05.018.

Kirsch V, Becker-Bense S, Berman A, **Kierig E**, Ertl-Wagner B, Dieterich M. Transient endolymphatic hydrops after an attack of vestibular migraine: a longitudinal single case study. *J Neurol*. 2018 Oct;265(Suppl 1):51-53. doi: 10.1007/s00415-018-8870-3.

Beitrag zu den Publikationen

Beitrag zur Publikation I

Im Rahmen der Veröffentlichung „Handedness-dependent functional organizational patterns within the bilateral vestibular cortical network revealed by fMRI connectivity based parcellation“ führte ich als Co-Autor eine umfassende Literaturrecherche sowie die eigenständige Erhebung und Auswertung der elektrophysiologischen, behavioralen und bildgebenden Daten durch. Dies umfasste insbesondere die Datenerhebung mittels Rekrutierung von Probanden, die Durchführung von funktionellen Tests des vestibulären Systems (Kopf-Impuls-Test, Subjektive Visuelle Vertikale) und die kernspintomographische Untersuchung. Darüber hinaus übernahm ich die Vorverarbeitung der MRT Daten mit Hilfe der Software SPM12 und MATLAB und unterstützte bei der Auswertung mittels unabhängiger Komponentenanalyse und statistischer Analyse. Außerdem trug ich zur Verfassung und Überarbeitung des Manuskripts sowie zur Erstellung der Abbildungen bei.

Beitrag zur Publikation II

Im Rahmen der geteilten Erstautorenschaft für das Paper “Vestibular paroxysmia entails changes in vestibular nerve microstructure and endolymphatic space“ bestand mein Beitrag in der Selektion und Rekrutierung der passenden Probanden (insbesondere der Patienten mit Vestibularisparoxysmie), der eigenständigen Durchführung der klinisch-funktionellen Tests und MRT Messungen, sowie ein Teil der statistischen und kernspintomographischen Datenauswertung (CISS, T1). Der zweite Erstautor, Herr Gerb, wertete den anderen Teil der MRT-Daten (DTI, T2) aus und unterstützte mich zum Teil bei der Messung der Probanden. Zusätzlich verfasste ich das Manuskript, erstellte die Abbildungen und fügte die Überarbeitungen der beteiligten Co-Autoren ein.

1. Einleitung

Die beiden Publikationen dieser kumulativen Dissertation untersuchen einerseits die funktionelle Organisation der Kortexareale im zentralen vestibulären System und andererseits strukturelle Veränderungen einer Pathologie im peripheren vestibulären System mittels Magnetresonanztomographie (MRT). Im Folgenden werden das zentrale und periphere vestibuläre System (siehe Kapitel 1.1) und die Vestibularisparoxysmie (siehe Kapitel 1.2) beschrieben. Das anschließende Kapitel erläutert die verwendete Bildgebung (siehe Kapitel 2).

1.1 Das vestibuläre System

Das vestibuläre System zählt zu den ältesten Sinnessystemen, das bereits vor 600 Millionen Jahren bei wirbellosen Tieren in Form des Statozysten zur Wahrnehmung der Schwerkraft existierte (Wolbarsht, 1966). Die meisten Aufgaben des vestibulären Systems werden unbewusst ausgeführt, sodass dessen Bedeutung häufig erst bei einem Ausfall wahrgenommen wird. Die verschiedenen Funktionen des vestibulären Systems lassen sich bestimmten anatomischen Ebenen zuordnen (Dieterich and Brandt, 2015). Nachfolgend werden der Aufbau und die Funktion des peripheren und zentralen vestibulären Systems dargestellt.

1.1.1 Das periphere vestibuläre System

Das Gleichgewichtsorgan, auch Vestibularorgan genannt, ist Teil des Innenohrs und befindet sich zusammen mit der Hörschnecke, der Cochlea, im knöchernen Labyrinth in der pars petrosa des Felsenbeins. Die cochleären Anteile liegen vorne medial, während drei Bogengänge (Ducti semicirculares) hinten lateral angeordnet sind (siehe Abbildung 1).

Im Inneren des knöchernen Labyrinths ist das häutige Labyrinth zu finden, das aus Epithelschläuchen besteht und zwei voneinander getrennte Flüssigkeiten, Endo- und

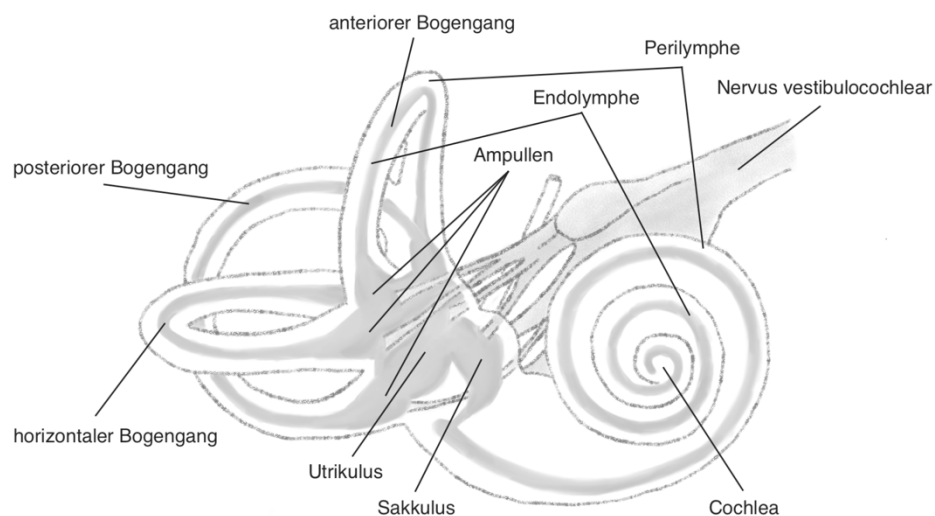


Abbildung 1: Das Innenohr besteht neben der Cochlea aus den drei Bogengängen sowie dem Sakkulus und Utrikulus. In Anlehnung an Abb. 14.19 aus [Feigenspan, 2017].

Perilymphe, enthält. Die Endolymphe enthält eine hohe Kaliumkonzentration (ca. 150 mmol/l), während die Perilymphe eine hohe Natriumkonzentration (ca. 150 mmol/l) aufweist. Hierdurch entsteht eine elektrische Spannungsdifferenz zwischen den beiden Flüssigkeiten. Diese ist für die Erzeugung eines elektrischen Signals entscheidend. Die Endolymphe wird von der Stria vascularis im Ligamentum spirale produziert. Der endolymphatische Raum bezeichnet die Flüssigkeitsräume im Innenohr, die die Endolymphe enthalten. Hierzu zählen unter anderem der Ductus cochlearis, Sakkulus, Utriculus, die Bogengänge, Ductus utriculosaccularis, Ductus reuniens, Ductus endolymphaticus und Saccus endolymphaticus. Eine pathologische Zunahme der Endolymphe im endolymphatischen Raum wird endolymphatischer Hydrops genannt, der mit einem Druckanstieg im endolymphatischen Raum einhergeht. Die Reissner- und Basilarmembran werden gedehnt, was zu Hörminderung, Schwindel oder Hörverlust bei Ruptur der Membran führen kann (Kimura and Schuknecht, 2010). Bei der Volumenregulation der Endolymphe spielt der Saccus endolymphaticus eine wichtige Rolle, da er durch Sekretion und Resorption die Endolymphmenge beeinflusst. Darüber hinaus fungiert der Ductus endolymphaticus ähnlich einem Ventil und transportiert überschüssige Endolymphe in den Saccus endolymphaticus (Bagger-Sjöbäck, Friberg and Rask-Anderson, 1986; Inamoto *et al.*, 2009; Salt and Plontke, 2010; Gürkov *et al.*, 2016). Initial wurde der endolymphatische Hydrops bei Morbus Menière beschrieben, er kann aber auch bei anderen Erkrankungen auftreten. So wurde ein Hydrops auch bei vestibulärer Migräne beobachtet (Valerie Kirsch *et al.*, 2018) oder kann sekundär nach Traumata oder Entzündungen (Chen and Young, 2016; Ferster *et al.*, 2017; Okazaki *et al.*, 2017; V Kirsch *et al.*, 2018) entstehen. In der zweiten Publikation wird dieser endolymphatische Raum mittels kontrastmittelverstärktem MRT zur untersucht (siehe Kapitel 2.2.2).

Eine Funktion des vestibulären Systems ist die Registrierung von Kopf- und Körperposition sowie Eigenbewegung. Anhand der Bogengänge und Makulaorgan wird eine mechanische Bewegung in ein elektrisches Signal umgewandelt, welches dem Gehirn Informationen über Linear- und Drehbeschleunigung liefert. Die Bogengänge nehmen dabei die Bewegungen in den drei Raumrichtungen wahr, während die Makulaorgane die lineare Beschleunigung in der Horizontalen und Vertikalen messen.

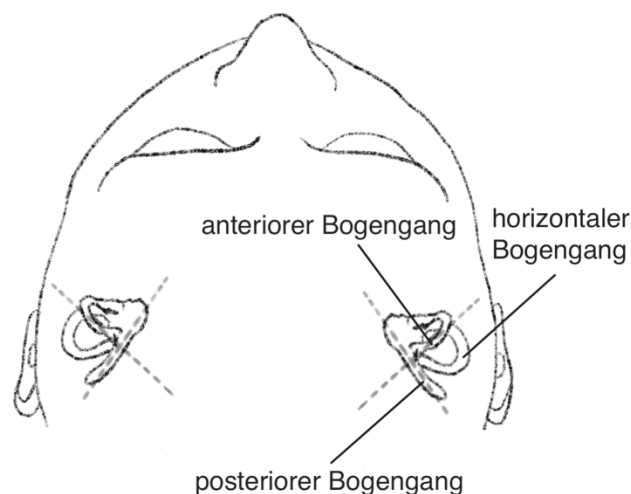


Abbildung 2: Lage und Anordnung der Bogengänge. Beachtenswert ist, dass der anteriore Bogengang der einen Seite in einer Achse liegt mit dem posterioren Bogengang der anderen Seite. In Anlehnung an [Fetter, 2010].

Die Bogengänge beinhalten Rezeptoren zur Messung von Drehbeschleunigung und sind zueinander wie ein Koordinatensystem angeordnet, um Bewegungen in den drei Raumachsen zu detektieren. Der horizontale Bogengang steht in einem 60°-Winkel zur aufrechten Körperachse. Der anteriore und posteriore Bogengang stehen vertikal und sind rechtwinklig zueinander ausgerichtet (siehe Abbildung 2). Somit steht der anteriore Bogengang einer Seite mit dem posterioren Bogengang der Gegenseite in einer Achse, wodurch sie immer in entgegengesetzte Richtungen gereizt werden. Die Bogengänge bestehen aus einem kreisförmigen, geschlossenen Kanal und einer Erweiterung, der sogenannten Ampulla. In der Ampulla befindet sich das Sinnesepithel, die Crista, umgeben von der Endolymphe. Die Crista besteht aus Typ-I- und Typ-II-Haarzellen, deren Spitzen, die Stereozilien sowie ein längeres Kinozilium, in eine gallertige Struktur namens Cupula ragen. Die Haarzellen sind mechanosensorische Rezeptoren, die eine mechanische Bewegung in elektrische Signale, eine sogenannte mechano-elektrische Transduktion, auslösen. Bei einer Drehung des Kopfes dreht sich der Kopf mit der Cupula gegen die träge, stehende Endolymphe, wodurch die Stereozilien im Sinne einer Scherbewegung ausgelenkt werden. Bei Auslenkung in Richtung der neben den Stereozilien positionierten Kinozilie kommt es zu einer Depolarisation, bei Auslenkung in die entgegengesetzte Richtung zu einer Hyperpolarisation (siehe Abbildung 3). Dadurch erfolgt eine Veränderung des Membranpotenzials, was zur Freisetzung von Glutamat in den synaptischen Spalt führt. Dies hat zur Folge, dass sich die Spontanaktivität der afferenten Nerven ändert und die Frequenz der Aktionspotenziale erhöht oder reduziert wird. Die Änderung dieser Frequenz ist direkt proportional zur Intensität der Drehbeschleunigung. Anhand der Potenzialänderung wird im Gehirn die wahrgenommene Beschleunigung errechnet. Auf diese Weise wird jede Bewegung im Raum in eine Vor- oder Zurückbewegung in den drei Raumachsen zerlegt und in Form eines elektrischen Signals weitergeleitet.

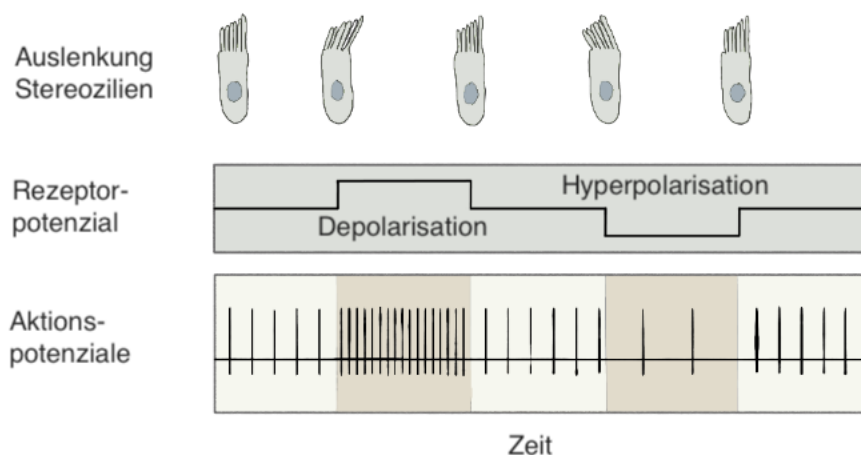


Abbildung 3: Die Auslenkung der Stereozilien in Richtung der Kinozilie führt zu einer Depolarisation, die durch eine erhöhte Glutamat Freisetzung die Aktionspotenzialfrequenz erhöht. Entgegengesetzt löst eine Hyperpolarisation eine Abnahme der Aktionspotenzialfrequenz in Vergleich zur Ruhefrequenz aus. In Anlehnung an Abb. 14.22 aus [Feigenspan, 2017].

Die Makulaorgane Sakkulus und Utrikulus – auch Otolithen genannt – stehen in einem 90°-Winkel zueinander, um Bewegungen in der Vertikalen und Horizontalen zu erkennen. Der Sakkulus ist zur Wahrnehmung der senkrechten Linearbeschleunigung vertikal angeordnet und der Utrikulus entsprechend horizontal. Obwohl die Schwerkraft auch eine Form der

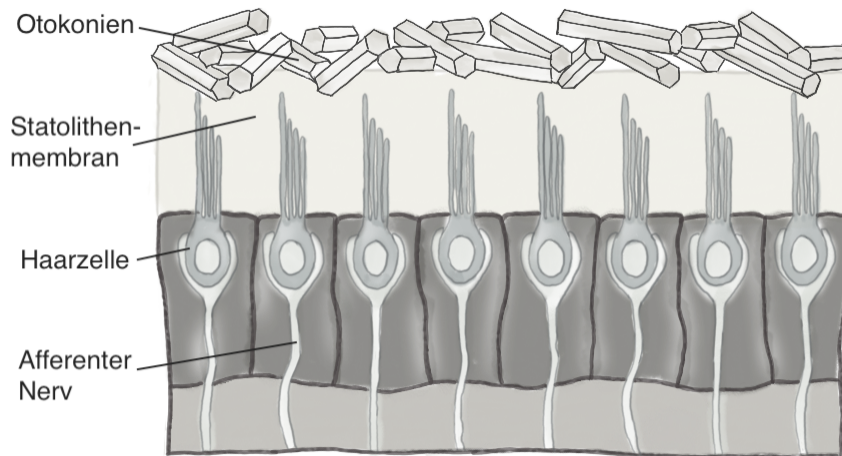


Abbildung 4: Darstellung der Makulaorgane mit den Stereozilien der Haarzellen die in die gallertartige Statolithenmembran reichen. In Anlehnung an Abb. 14.24 aus [Feigenspan, 2017].

Translationsbeschleunigung darstellt, wird sie vielmehr als die Stellung des Kopfes und des Körpers interpretiert. Die Maculae sacculi und utriculi, die aus Haarzellen und Stützzellen bestehen, liegen im Vestibulum des Labyrinths. Die Stereozilien dieser Haarzellen ragen in eine gallertige Schicht, die Statolithenmembran, hinein. Diese Gallertschicht ist mit Kalziumkarbonatkristallen, den sogenannten Otokonien, bedeckt (siehe Abbildung 4). Die Otokonien haben ein höheres spezifisches Gewicht als die Endolymphe, wodurch es bei einer Translationsbewegung zur Parallelverschiebung und zu einer entsprechenden Auslenkung der Zilien kommt. Die Auslenkung der Zilien führt zu einer Erhöhung bzw. einer Verringerung des Rezeptorpotenzials und moduliert hierüber die Freisetzung des Botenstoffs Glutamat. Die Glutamat Freisetzung in den synaptischen Spalt führt zu einer Depolarisation der dendritischen Fortsätze der nachfolgenden bipolaren Neuronen.

Die Nervenfortsätze bilden den Nervus vestibularis. Die Informationen des horizontalen und des anterioren Bogengangs sowie der Utrikulus laufen über den superioren Anteil des Nervus vestibularis zusammen, während die Informationen des hinteren Bogengangs und des Sakkulus

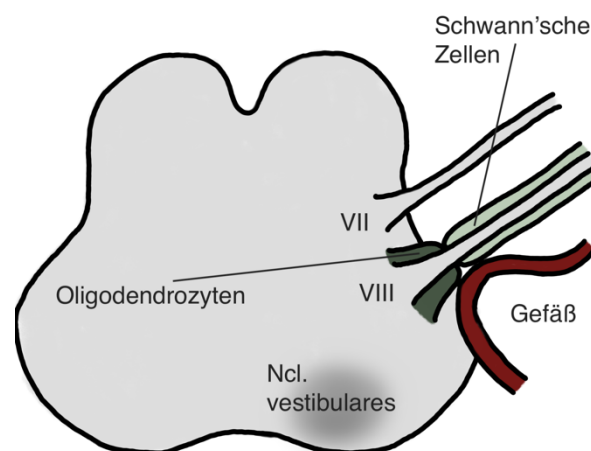


Abbildung 5: Darstellung der *Root-Entry-Zone* des Nervus vestibulocochlearis mit Wechsel der Myelinscheide von Schwann'schen Zellen auf Oligodendrozyten. Eigene Darstellung.

über den Nervus vestibularis inferior übermittelt werden. Der Nervus vestibularis vereint sich mit dem Nervus cochlearis, der die Signale der Cochlea führt, zu dem Nervus vestibulocochlearis, der durch den Meatus acusticus internus in die hintere Schädelgrube zieht. Am Unterrand der Pons tritt der Nervus vestibulocochlearis in den Hirnstamm ein und trennt sich wieder in die vestibulären und cochleären Fasern. Der Nerv ist mit einer Myelinscheide isoliert, die im peripheren Nervensystem von Schwann'schen Zellen gebildet wird und im zentralen Nervensystem von Oligodendrozyten (siehe Abbildung 5). Der Wechsel dieser Myelinscheide liegt im Bereich des Nerveintritts in den Hirnstamm, der als *Root-Entry-Zone* bezeichnet wird. Diese *Root-Entry-Zone* scheint eine erhöhte Empfindlichkeit zu haben und wird als Einflussfaktor in der Pathophysiologie der Vestibularisparoxysmie erachtet (siehe Kapitel 1.2).

1.1.2 Das zentrale vestibuläre System

1.1.2.1 Hirnstamm und Thalamus

In der Medulla oblongata liegen die Vestibulariskerne. Hier findet die erste Verarbeitung der vestibulären Informationen statt und die Reflexbögen zur sensomotorischen Kontrolle des Blicks und des Gleichgewichts werden verschaltet (siehe Abbildung 6). Außer den vestibulären Informationen laufen hier auch visuelle und propriozeptive Informationen von Muskelspindeln, Sehnenorganen sowie Gelenken zusammen (Bucher *et al.*, 1998; Emri *et al.*, 2003; Baumgärtner *et al.*, 2010; Kathleen E. Cullen, 2014). Des Weiteren gibt es zentrale Afferenzen von Rückenmark, Colliculus superior, Kleinhirn und Kortex (Carpenter, 1963; Büttner-Ennever, 1992).

Die Vestibulariskerne werden in Nucleus vestibularis superior (Bechterew-Kern), Nucleus vestibularis inferior (Roller-Kern), Nucleus vestibularis medialis (Schwalbe-Kern) und Nucleus vestibularis lateralis (Deiters-Kern) unterschieden. Die Afferenzen der Bogengänge enden hauptsächlich im Nucleus vestibularis superior und medialis, die der Makulaorgane im Nucleus vestibularis lateralis. Folglich reagieren die Neurone in diesen Kernen sensitiver auf Rotations- oder Translationsbewegungen.

Von allen vier Kerngebieten ziehen Efferenzen im Fasciculus longitudinalis medialis zu den drei motorischen Augenmuskelkernen Nucleus nervi oculomotorius, Nucleus nervi trochlearis und Nucleus nervi abducentis. Diese bilden den vestibulookulären Reflexbogen, der es ermöglicht, Objekte trotz Bewegungen des Körpers oder des Kopfes fixieren zu können (Schwarz, 1976) (siehe Abbildung 6).

Daneben ziehen der Tractus vestibulospinalis medialis und lateralis im Vorderstrang des Rückenmarks zu den Motoneuronen im cervikalen, thorakalen und lumbalen Rückenmark (Büttner-Ennever, 1992, 1999) (siehe Abbildung 6). Hierüber ist das vestibuläre System mit der Skelettmuskulatur vernetzt und steuert die Skelettmuskulatur auf spinaler Ebene. Über den Tractus vestibulospinalis lateralis läuft der vestibulospinale Reflex, der durch Stellreflexe das Gleichgewicht aufrechterhält (Pozzo, Berthoz and Lefort, 1990).

Der Tractus vestibulocerebellaris läuft von den Nuclei vestibularis superior, inferior und medialis zum Kleinhirn in den Lobus flocculonodularis und ist für die Regulation des Muskeltonus sowie der Augenmotorik verantwortlich.

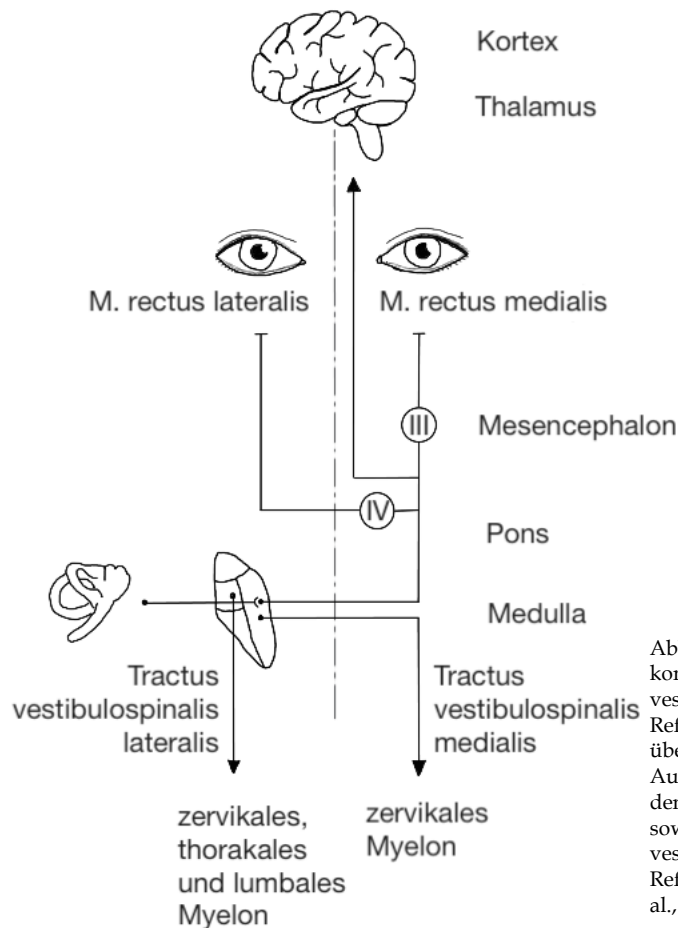


Abbildung 6: Schematische Darstellung der komplexen Verbindungen der Nuclei vestibularis anhand des vestibulookulären Reflexes. Zu erkennen sind die Verbindungen über den Drei-Neuronen-Reflexbogen zu den Augenmuskeln, die Verbindungen über den Thalamus zum parieto-insulären Kortex sowie die Verbindungen entlang des Tractus vestibulospinalis für die vestibulospinalen Reflexe. In Anlehnung an Abb. 1.2 aus [Brandt et al., 2013].

Es wurden bisher fünf unterschiedliche vestibuläre Bahnen beschrieben, die die vestibulären Kernen mit dem ipsilateralen und dem kontralateralen vestibulären Kortex verbinden, wovon einige über den Thalamus verlaufen (Dieterich *et al.*, 2005; Conrad, Baier and Dieterich, 2014). Drei dieser Bahnen verlaufen ipsilateral, während die beiden anderen entweder in der Pons oder im Mittelhirn kreuzen (Kirsch *et al.*, 2015).

Der Thalamus fungiert als Schaltstation, in der vestibuläre, visuelle und propriozeptive Informationen zusammenlaufen (Blum *et al.*, 1979; Büttner and Lang, 1979; Dieterich *et al.*, 2005). An der Verarbeitung sind mehrere Kerngebiete beteiligt, in denen multisensorische Neurone beschrieben sind, die die Signale prozessieren, integrieren und anschließend an den vestibulären Kortex weiterleiten (Conrad, Baier and Dieterich, 2014; Baier *et al.*, 2016).

1.1.2.2 Kortex

Der vestibuläre Kortex unterscheidet sich von anderen sensorischen Kortexen durch das Fehlen eines primären Kortex im engeren Sinne. Ein primärer Kortex zeichnet sich durch isolierte Afferenzen aus einem peripheren Sinnesorgan aus und wird durch eine entsprechende modalitätsspezifische Verarbeitung definiert. Im Gegensatz dazu nutzt das vestibuläre System ein Netzwerk aus mehreren multisensorischen kortikalen Bereichen in beiden Hemisphären. Die Kernregion dieses Netzwerks ist die posteriore Insel und die retroinsuläre Region, die in Makaken den Namen parieto-insulärer vestibulärer Kortex (PIVC) trägt (Guldin and Grüsser, 1998). Beim Menschen scheint das vestibuläre System ähnlich aufgebaut zu sein, mit der

posterioren Insel, der retroinsulären Region und dem Operculum 2 als Hauptbestandteile dieser Kernregion (Guldin and Grüsser, 1998; Brandt and Dieterich, 1999). Zusätzlich sind der obere temporale Gyrus, der angulare und der supramarginale Gyrus im Parietallappen, der somatosensorische Kortex, der Präkuneus, der Gyrus cinguli im frontalen Kortex und der Hippocampus an der vestibulären Verarbeitung beteiligt (Fasold *et al.*, 2002; Emri *et al.*, 2003; Lopez, Blanke and Mast, 2012; Zu Eulenburg *et al.*, 2012).

Der vestibuläre Kortex entspricht daher vielmehr einem bilateralen Netzwerk aus multiplen, multisensorischen Kortextbereichen (Dieterich and Brandt, 1993; Zwergal *et al.*, 2009; Baier *et al.*, 2012). Auf der kortikalen Ebene sind die vestibulären Kortexte beider Hemisphären durch das Splenium corpus callosi transcallosal miteinander verbunden. Die Informationen werden bilateral (Dieterich and Brandt, 2015) und in mehreren Hirnarealen (Lopez and Blanke, 2011) verarbeitet. Beim Affen wurden innerhalb dieser Areale multimodale Neuronen und verschiedene unimodale Neuronen gefunden (Guldin, Akbarian and Grüsser, 1992; Yang *et al.*, 2011).

Ein wesentliches Merkmal dieses bihemiphärischen vestibulären kortikalen Netzwerks ist eine funktionelle Asymmetrie zu Ungunsten der dominanten Hemisphäre in Hinblick auf die Händigkeit. Das heißt, bei Rechtshändern besteht eine Hemisphärendominanz vestibulärer Hirnareale in der rechten Hemisphäre und bei Linkshändern in der linken Hemisphäre (Dieterich *et al.*, 2003). Eine Metaanalyse der funktionellen Bildgebung bestätigte die Dominanz der rechten Hemisphäre bei Rechtshändern (Zu Eulenburg *et al.*, 2012). Eine weitere Besonderheit ist ein wechselseitig inhibitorisches visuell-vestibuläres Zusammenspiel (Wenzel *et al.*, 1996; Brandt, 1998; Brandt *et al.*, 2002).

Der vestibuläre Kortex ist zudem an verschiedenen kognitiven Funktionen beteiligt. Hierzu zählen die räumliche Orientierung (Berthoz *et al.*, 1995; Mittelstaedt, 1999) und das räumliche Gedächtnis (Smith, Darlington and Zheng, 2010), als auch die Unterscheidung zwischen Eigen- und Objektbewegung (Straube and Brandt, 1987), die für die Wahrnehmung der Vertikalität notwendig ist (Brandt, Dieterich and Danek, 1994; Mittelstaedt, 1999; Lopez, Halje and Blanke, 2008). Weiterhin ist es an der Entwicklung eines internen Modells von Schwerkraft und Körperbewegung (Brandt, 1998; Merfeld, Zupan and Peterka, 1999; Angelaki *et al.*, 2004) sowie der Körperwahrnehmung und dem Körperbewusstsein beteiligt (Vallar *et al.*, 1993; Bottini *et al.*, 1995).

Aufgrund dieses multisensorischen, auf mehrere Hirnareale verteilten Netzwerkes, ist die Bildgebung des vestibulären Kortex erschwert. In der ersten Publikation wurden mittels funktioneller MRT Ruhenetzwerke (siehe Kapitel 2.1.2) dieses vestibuläre, kortikale Netzwerk dargestellt und in Abhängigkeit der Händigkeit untersucht.

1.2 Vestibularisparoxysmie

Die zweite Publikation beschäftigt sich mit strukturellen Veränderungen am peripheren vestibulären System bei der Vestibularisparoxysmie. Die Symptomatik einer Vestibularisparoxysmie wurde erstmals von Jannetta als Kompressionssyndrom des VIII. Hirnnervens beschrieben (Jannetta, 1975) und später klinisch charakterisiert und so benannt (Brandt and Dieterich, 1994a).

Bei der Vestibularisparoxysmie handelt es sich um eine periphere vestibuläre Störung, die zu sehr kurzen, wiederkehrenden Schwindelattacken führt (Brandt and Dieterich, 1994b; Hüfner *et al.*, 2008). Die Diagnose wird anhand klinischer Kriterien nach der Definition der Internationalen Bárány Society gestellt (Strupp *et al.*, 2017). Die Schwindelattacken sind durch eine kurze Dauer von wenigen Sekunden bis unter fünf Minuten charakterisiert und treten in gleicher Art und Weise in hoher Frequenz, teils täglich auf. Sie können spontan auftreten oder seltener durch Kopfdrehungen oder Hyperventilation provoziert werden. Zum Teil sind auch begleitende Ohrsymptome (Tinnitus) beschrieben. Während einer Schwindelattacke kann in einigen Fällen ein horizontal-torsioneller Nystagmus zum betroffenen Ohr beobachtet werden. Ein wichtiges Diagnosekriterium zur Stellung einer sicheren Diagnose ist das positive Ansprechen auf die Therapie mit einem Natriumkanal-Blocker (Brandt and Dieterich, 1994a; Strupp *et al.*, 2017).

Die genaue Pathophysiologie ist bisher nicht endgültig verstanden (Karamitros *et al.*, 2022). Ein Faktor scheint eine Druckläsion des VIII. Hirnnerven durch ein Gefäß, meist einer pulsierenden Arterie, typischerweise der Arteria inferior anterior cerebelli. Hierbei wird angenommen, dass der wiederholte pulsierende Druck, der auf den Nerv wirkt, zu einer Demyelinisierung führt. Dies wiederum verursacht eine Übererregbarkeit des Nervus vestibulocochlearis, die eine ephaptische Depolarisation wahrscheinlicher macht (Jannetta, 1975, 1979; Jannetta, Møller and Møller, 1984; Brandt and Dieterich, 1994a). Diese These wird durch den in vereinzelt Fällen berichteten Therapieerfolg unterstützt, der mit einer operativen Dekompression des Nervus vestibulocochlearis einherging (Jannetta *et al.*, 1986; Møller, 1991; Strupp *et al.*, 2013). Aufgrund des hohen perioperativen Risikos von Vasospasmen und Hirnstamminfarkten stellt dies jedoch keine empfohlene Therapie dar (Strupp *et al.*, 2017, p. 201). Allerdings ist ein Gefäß-Nerven-Kontakt nicht bei allen Patienten mit Vestibularisparoxysmie nachzuweisen (Hüfner *et al.*, 2008). Auch scheint dieser nicht immer mit der Seite der audiovestibulären Störungen zu korrelieren (Markowski *et al.*, 2011). Umgekehrt kann ein Gefäß-Nerven-Kontakt bei 30% der gesunden Probanden nachgewiesen werden (Parnes *et al.*, 1990; Hüfner *et al.*, 2008; Best *et al.*, 2013). Folglich führt ein Gefäß-Nerven-Kontakt nicht zwangsläufig zu klinischen Symptomen oder messbaren vestibulären Funktionsstörungen (Markowski *et al.*, 2011).

Ein weiterer möglicher Faktor für die Entwicklung einer Vestibularisparoxysmie scheint die erhöhte Empfindlichkeit des Nervus vestibulocochlearis beim Wechsel vom peripheren in das zentrale Nervensystem zu sein (Hüfner *et al.*, 2008) (siehe Kapitel 1.1.1). In der Ein- bzw. Austrittszone in den Hirnstamm, der sogenannten *Root-Entry-Zone*, wechselt die Art der Myelinscheide von den peripheren Schwann'schen Zellen auf zentrale Oligodendrozyten (De Ridder *et al.*, 2002). Der Nervus vestibulocochlearis hat von allen Hirnnerven den längsten zentralen Myelinanteil (Sivarasan *et al.*, 2019). Entscheidend für eine pathologische mikrovaskuläre Kompression könnte daher zudem deren Lokalisation in der *Root-Entry-Zone* sein. Hinzu kommt vermutlich eine zentrale Pathophysiologie mit erhöhter Erregbarkeit innerhalb der Hirnnervenkerne z.B. durch eine reduzierter Hemmung der Hirnnervenkerne durch thalamisch-kortikalen Projektion (Esteban and Molina-Negro, 1986; Ishikawa *et al.*, 1997; Best *et al.*, 2013).

Die Therapie der Vestibularisparoxysmie besteht aus einem Natriumkanal-Blocker wie Carbamazepin, Oxcarbazepin oder Lacosamid, der das Membranpotenzial stabilisiert und dadurch die Erregbarkeit des Nervus vestibulocochlearis reduziert. Hierunter kommt es zu einer

Abnahme der Attackenfrequenz, -intensität und -dauer bis hin zum Sistieren der Attacken (Hüfner *et al.*, 2008).

In der zweiten Publikation dieser Dissertation wurden der Gefäß-Nerven-Kontakt sowie mögliche strukturelle Veränderungen des Nervus vestibulocochlearis und des endolymphatischen Raums bei der Vestibularisparoxysmie mit unterschiedlichen MRT Sequenzen untersucht (siehe Kapitel 2.2.1 und 2.2.2).

2. Magnetresonanztomographie

Die Magnetresonanztomographie (MRT) ist ein nicht invasives bildgebendes Verfahren, das mit einem starken Magnetfeld und hochfrequenten Radiowellen Schnittbilder erzeugt. Sie beruht auf dem physikalischen Prinzip des Eigendrehimpulses, sogenannten Spin, von Atomkernen, insbesondere Wasserstoffatomen. Durch ein starkes Magnetfeld werden die ansonsten ungeordneten Atomkerne in Abhängigkeit von der Magnetfeldrichtung ausgerichtet. Anschließend werden die Atomkerne durch Radiowellen in Schwingung versetzt und erzeugen nach dem Ende des Radiosignals elektrische Impulse, die je nach Gewebeart variieren (Radue *et al.*, 2016).

Beide Publikationen nutzen die Magnetresonanztomographie zur Darstellung und Untersuchung verschiedener Komponenten des vestibulären Systems. In der ersten Publikation wurde der vestibuläre Kortex anhand von Ruhenetzwerken in funktionelle Untereinheiten geteilt und diese in Abhängigkeit der Händigkeit weiter analysiert (siehe Kapitel 2.1.2). Die zweite Publikation nutzt die Magnetresonanztomographie zur Quantifizierung struktureller Veränderungen des peripheren vestibulären Systems bei der Vestibularisparoxysmie. Zum einen wurde anhand von DTI Sequenzen Veränderungen an der Nervenstruktur analysiert (siehe Kapitel 2.2.1), zum anderen mit Hilfe von Kontrastmittel das Volumen des endolymphatischen Raums bestimmt (siehe Kapitel 2.2.2).

2.1 Funktionelle Magnetresonanztomographie

2.1.1 BOLD Kontrast

Funktionelles MRT (fMRT) nutzt unterschiedliche Magnetfeldgradienten, um die Aktivität von Hirnarealen sichtbar zu machen. Die Grundlage dafür ist, dass die Aktivierung von Hirnarealen zu einem erhöhten zerebralen Blutfluss und Sauerstoffverbrauch führt, der durch die unterschiedlichen magnetischen Eigenschaften von desoxygeniertem und oxygeniertem Hämoglobin sichtbar gemacht wird und als *Blood Oxygenation Level Dependent* Kontrast bezeichnet wird (S. Ogawa *et al.*, 1990; Bandettini *et al.*, 1992; Kwong *et al.*, 1992; Ogawa *et al.*, 1993).

Die Aktivierung eines Hirnareals führt zu einem erhöhten Energie- und Sauerstoffbedarf (Buxton and Frank, 1997). Dementsprechend kommt es zu einem erhöhten zerebralen Blutfluss, der nach initialer Zunahme von desoxygeniertem Hämoglobin und Abnahme von oxygeniertem Hämoglobin zu einer Umkehr mit Anstieg des oxygenierten Hämoglobin und eine Abnahme des desoxygenierten Hämoglobin im Vergleich zum Ruhezustand führt (siehe Abbildung 7) (Buxton, Wong and Frank, 1998; Davis *et al.*, 1998). Diese Änderungen stellen vermutlich die hämodynamische Reaktion auf neuronale Ereignisse dar. Im MRT kann eine erhöhte neuronale Aktivität zum einen durch einen gesteigerten lokalen zerebralen Blutfluss und zum anderen durch eine Veränderung der Sauerstoffkonzentration abhängig vom Sauerstoffgehalt des Blutes nachgewiesen werden.

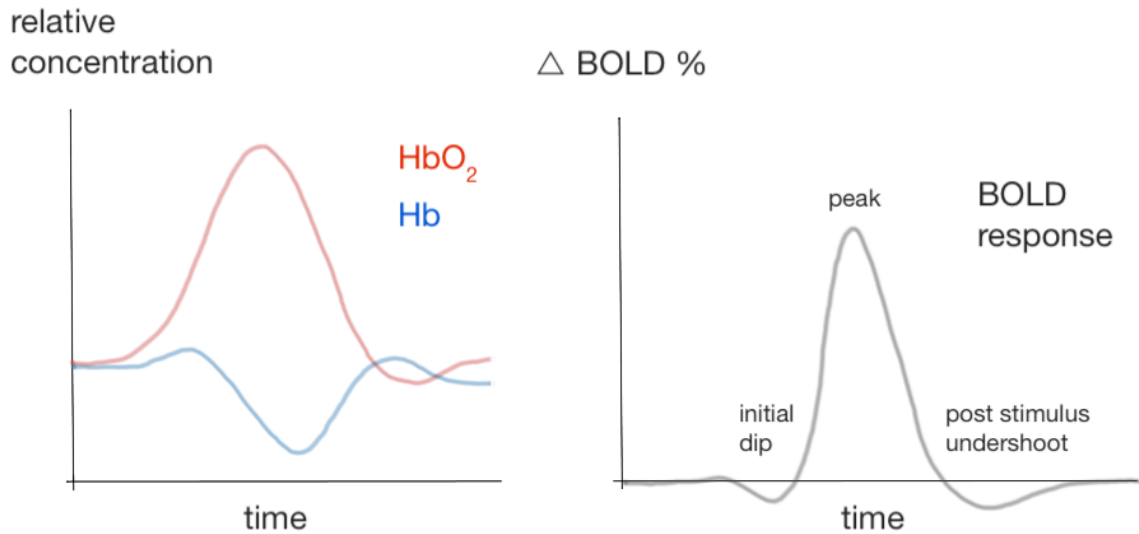


Abbildung 7: Darstellung der Hämoglobin Konzentrationen sowie des korrespondierenden BOLD Signals. Die Erhöhung des zerebralen Blutflusses bewirkt einen Anstieg des oxygenierten Hämoglobins. Auf der rechten Seite ist das BOLD Signal dargestellt, welches auf der Abnahme des paramagnetischen desoxygeniertem Hämoglobin basiert. In Anlehnung an Abb. 1 [Cinciute, 2019].

Diese Veränderung der Sauerstoffkonzentration wird als *Blood Oxygenation Level Dependent* Kontrast (BOLD Kontrast) bezeichnet und wurde zuerst an Ratten (Ogawa and Lee, 1990; Seiji Ogawa *et al.*, 1990) und später am Menschen (S. Ogawa *et al.*, 1990; Bandettini *et al.*, 1992; Kwong *et al.*, 1992; Ogawa *et al.*, 1993) nachgewiesen. Der BOLD Kontrast resultiert aus der Veränderung des Magnetfeldes, das die roten Blutkörperchen in Abhängigkeit vom Sauerstoffzustand des Hämoglobins umgibt. Der Paramagnetismus des sauerstofffreien Hämoglobins (Pauling and Coryell, 1936; Thulborn *et al.*, 1982) führt zu lokalen Gradienten im Magnetfeld, dessen Stärke von der Hämoglobin Konzentration abhängt. Diese endogenen Gradienten modulieren die Signalintensität von Magnetresonanzbildern (Thulborn *et al.*, 1982; Ogawa and Lee, 1990; Seiji Ogawa *et al.*, 1990; S. Ogawa *et al.*, 1990). Das resultierende BOLD Signal verhält sich annähernd proportional zur neuronalen Aktivität (Logothetis, 2003).

2.1.2 Funktionelle Parzellierung mittels Ruhenetzwerken

Die funktionelle Magnetresonanztomographie bietet die Möglichkeit das Gehirn *in vivo* zu parzellieren (Van Essen and Glasser, 2014) um somit die Organisationsprinzipien und kognitiven Prozesse besser zu verstehen (Greicius *et al.*, 2009; Smith *et al.*, 2009). In Studien zur Aufgabenaktivierung können die Veränderungen der Hirnaktivität während visueller, akustischer oder anderer Stimuli untersucht werden. Durch den Vergleich der aufgezeichneten Signale während der verschiedenen Zustände werden Aktivierungskarten erstellt. Neben den Aktivierungsstudien gibt es auch die Bildgebung von Ruhenetzwerken (*resting state network*, RSN). Hier wird der Ruhezustand des Gehirns, der sogenannte *Resting State*, mittels fMRT in Abwesenheit von externen Reizen oder expliziten Aufgaben untersucht. Dabei werden regionale Interaktionen einzelner Hirnregionen mittels niederfrequenter BOLD Schwankungen aufgezeichnet (Biswal *et al.*, 1995). Aufgrund zeitlicher Fluktuationen können verschiedene, sogenannte *Default Mode* Ruhenetzwerke erfasst werden (Eickhoff *et al.*, 2015). Diese spontanen Modulationen in Abwesenheit eines expliziten Inputs oder Outputs werden als Zusammenarbeit

zwischen entfernten Hirnarealen gewertet und sind eine Form der funktionellen Parzellierung des Gehirns.

In der ersten Publikation der vorliegenden Dissertation wurde die unabhängige Komponentenanalyse zur Analyse vestibulärer Ruhenetzwerke angewandt (Beckmann and Smith, 2004; Smith *et al.*, 2009).

Die unabhängige Komponentenanalyse (*Independent Component Analysis, ICA*) ist eine Methode der multivariaten Statistik aus dem Bereich der Signalverarbeitung, mit der sich Ursprungssignale aus einem linearen Signalgemisch herausfiltern lassen. Dabei wird davon ausgegangen, dass höchstens eine Variable gaußförmig verteilt ist und, dass die Variablen statistisch unabhängig voneinander sind (Hyvärinen, 2013). Die Daten werden in eine zweidimensionale Matrix zerlegt (siehe Abbildung 8). Die Matrix stellt den zeitlichen Verlauf und die räumliche Ausdehnung der zugrunde liegenden Ursprungssignale dar. Im Falle der fMRT ist dies das BOLD Signal, das in seine Frequenzen zerlegt wird. Anschließend werden alle Voxel eines Datensatzes aufgrund dieser zerlegten BOLD Frequenzen verschiedenen Ruhenetzwerken zugeordnet. Die entstehende Bildgebung dieser Ruhenetzwerke werden auch funktionelle Konnektivitätskarten genannt. Die gefundenen Netzwerke korrelieren in ihrer zeitlichen spontanen BOLD Fluktuation, sind aber räumlich getrennt und unabhängig voneinander (Kiviniemi *et al.*, 2003; Beckmann *et al.*, 2005). Der Vorteil der statistischen Unabhängigkeit der räumlichen Komponenten ist, dass jede errechnete Karte einzeln interpretiert werden kann (Beckmann, 2012).

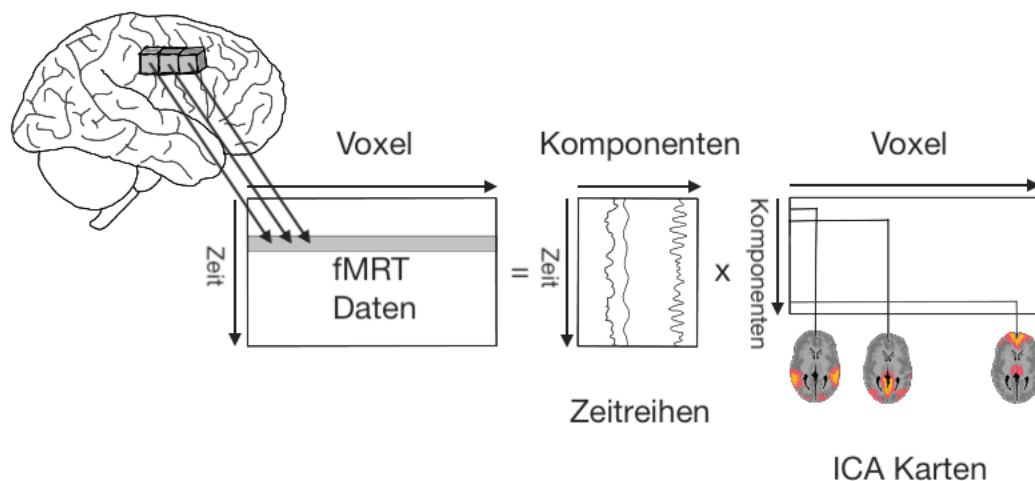


Abbildung 8: Schematische Darstellung der unabhängigen Komponentenanalyse. Die fMRT-Daten werden in einer zweidimensionalen Matrix dargestellt. Die Voxel werden als Spalten angeordnet, die Zeit als Zeilen. Mithilfe der ICA wird diese Matrix in das Produkt zweier Matrizen umgewandelt. Die eine Matrix stellt dabei die zeitlichen Verläufe der Signale dar. Die andere Matrix zeigt die Regionen, die zeitlich kohärent sind. In Anlehnung an Abb. 15.20 aus [Schneider and Fink, 2013].

2.2 Strukturelle Magnetresonanztomographie

Die Magnetresonanztomographie kann auch für strukturelle Fragestellungen angewendet werden. In der zweiten Publikation der vorliegenden Dissertation werden Veränderungen des Nervus vestibulocochlearis mittels *Diffusion Tensor Imaging* analysiert und das Volumen des endolymphatischen Raum anhand einer verzögerten Kontrastmittelanreicherung bestimmt.

2.2.1 Beurteilung der Nervenintegrität mittels Diffusion Tensor Imaging

Diffusion Tensor Imaging (DTI) ist ein MRT Verfahren, mit dem in-vivo Nervenfasern dargestellt werden können. Die Diffusionsbildgebung basiert auf der molekularen Bewegung von Wassermolekülen, auch Brownsche Bewegung genannt, die im Hirngewebe als Teils der physikalischen Diffusion vorkommt (Merboldt, Hanicke and Frahm, 1985; Taylor and Bushell, 1985; Le Bihan, 2003). Bei der Diffusionsbildgebung werden Magnetfeldgradienten erzeugt, die dazu dienen, die Wassermoleküle auszurichten. Während die starken Magnetfelder eingeschaltet sind, werden die Wassermoleküle in Richtung der Gradienten beeinflusst und ihre Bewegung ist entlang dieser Richtung eingeschränkt. Durch die Generierung mehrerer Magnetfeldgradienten in verschiedene Richtungen wird die Bewegung der Wassermoleküle in verschiedenen Raumrichtungen erfasst. Anhand der Messungen der Molekülbewegungen wird ein Diffusionstensor berechnet, der die Stärke der Diffusion in die verschiedenen Richtungen beschreibt (Le Bihan *et al.*, 2001). Basierend auf dem Diffusionstensor werden Bilder erzeugt, die die stärkste Diffusion von Wassermolekülen darstellen. Die Anisotropie, also die Richtungseigenschaft des jeweiligen Gewebes, beeinflusst die Diffusionsbewegungen. Nervenfasern haben eine hohe Anisotropie, sodass die Bewegung der Wassermoleküle entlang der Fasern eingeschränkt ist. Entsprechend verläuft die stärkste Diffusion parallel zur vorherrschenden Faserrichtung des Gewebes (siehe Abbildung 9). Dadurch wird die dominante Faserorientierung in jedem Voxel bestimmt und somit die mittlere Längsrichtung der Axone dargestellt (Le Bihan and van Zijl, 2002). Anhand der Diffusionsbildgebung kann daher die Struktur und der geometrische Aufbau von Hirngewebe untersucht werden.

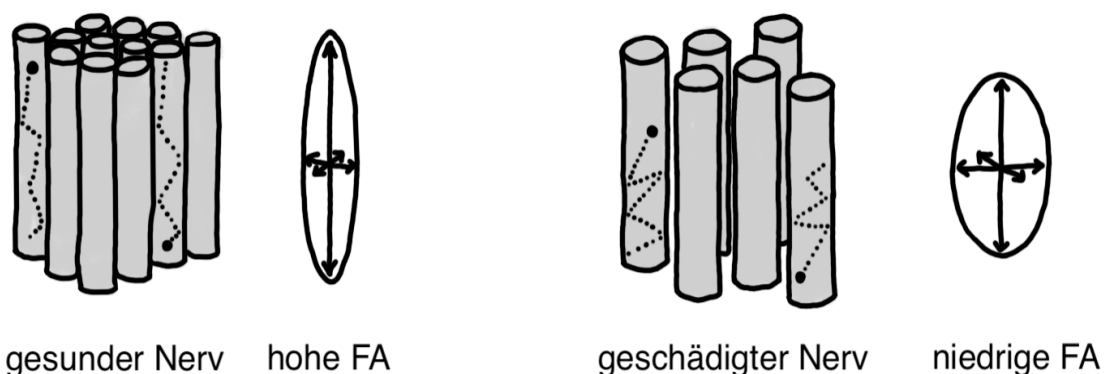


Abbildung 9: Darstellung eines gesunden Nervens mit Myelinscheide und dichter Anordnung, wodurch die Diffusion in der Längsachse des Nervens eingeschränkt ist. Auf der rechten Seite Darstellung eines geschädigten Nervens mit veränderter Mikrostruktur und vermehrter Diffusion senkrecht zur Längsachse des Nervens. In Anlehnung an Abb. 1 [Rojoa, 2021].

Die Integrität des Nervens wird mittels der Anisotropie, der Richtungseigenschaft des Gewebes, und des *Apparent Diffusion* Koeffizienten (ADC) untersucht (Le Bihan, 1995; Leal *et al.*, 2019). Strukturelle Schäden im Hirngewebe beeinflussen die molekulare Diffusion und dadurch die Gewebeanisotropie. Veränderungen der Anisotropie können anhand der fraktionellen Anisotropie (*Fractional anisotropy*, FA) erfasst werden (Pierpaoli and Basser, 1996; Pierpaoli *et al.*, 1996). Eine Nervenschädigung führt zu einer weniger gerichteten Diffusion und niedrigeren FA Werten (siehe Abbildung 9). Es wird daher angenommen, dass die FA ansatzweise die Faserdichte, den axonalen Durchmesser und die Myelinisierung in der weißen Substanz widerspiegelt (Yuan *et al.*, 2022).

Ein weiterer Parameter ist der *Apparent Diffusion* Koeffizient, er beschreibt quantitativ die Geschwindigkeit der Wassermoleküle, welche von der Mikrostruktur abhängt. Bei Nervenschädigung ändert sich der *Apparent Diffusion* Koeffizient aufgrund der veränderten Mikrostruktur.

2.2.2 Darstellung des Endolymphatischen Raums mittels kontrastmittelverstärktem MRT

Die Darstellung des endo- und perilymphatischen Raumes (siehe Kapitel 1.1.1) mittels MRT ist aufgrund der ähnlichen Zusammensetzung der Flüssigkeiten und dünnen Membran nur mit der Hilfe von Kontrastmittel möglich. Hierzu erfolgt eine intravenöse Gabe von Gadolinium Kontrastmittel. Nach 4 Stunden hat sich das Kontrastmittel im Körper verteilt und die optimale Anreicherung in der Perilymphe erreicht. Das Kontrastmittel kann die Reissner Membran nicht durchdringen, entsprechend kann mit Hilfe einer Subtraktionsanalyse Perilymphe von Endolympe und Knochen unterschieden werden. Hierfür wird eine *3D real Inversion Recovery* (*3D-real IR*) Sequenz von einer T2-gewichteten *3D-Fluid-Attenuated Inversion Recovery* (FLAIR) Sequenz subtrahiert um den endolymphatischen Raum nicht invasiv darzustellen (Nakashima *et al.*, 2007; Naganawa *et al.*, 2008, 2013; Sano *et al.*, 2012).

Zur Diskriminierung zwischen physiologischer Weite des endolymphatischen Raums und einem pathologischen endolymphatischen Hydrops (siehe Kapitel 1.1.1) ist eine Quantifizierung der Ausprägung des endolymphatischen Raums nötig. Nicht nur die Ausprägung des Hydrops, sondern auch die lokale Beteiligung z.B. von Cochlea und oder Vestibulum ist wichtig, auch um die Effektivität von Therapien zu objektivieren. Zur Einteilung des endolymphatischen Hydrops gibt es verschiedene semi-qualitative und quantitative Methoden. Bei der semi-qualitativen Graduierung wird der endolymphatische Raum anhand der Größe im Vergleich zum totalen Flüssigkeitsraum in verschiedene Grade eingeteilt (Nakashima *et al.*, 2009; Liu *et al.*, 2011). Die quantitative Klassifikation kann entweder zweidimensional anhand der Fläche oder dreidimensional anhand des berechneten Volumen erfolgen (Homann *et al.*, 2015; Boegle *et al.*, 2021). Die unterschiedlichen Graduierungen können entweder manuell, semi-automatisiert oder voll-automatisiert durchgeführt werden, wobei bei der automatisierten Graduierung unterschiedliche *Deep-Learning-Algorithmen* verwendet werden. In der zweiten Publikation wird eine automatische volumetrische Segmentierung mittels eines auf *Volumetric Local Thresholding* (VOLT) basierendem Algorithmus (Gerb *et al.*, 2020; Ahmadi *et al.*, 2022) verwendet.

3. Zusammenfassung

Die vorliegende kumulative Dissertation untersucht das zentrale und periphere vestibuläre System mittels struktureller und funktioneller Magnetresonanztomographie in Kombination mit elektrophysiologischen und behavioralen Parametern (Publikation 1) oder im Unterschied zu einer vestibulär erkrankten Kohorte (Publikation 2). Das vestibuläre System ist vergleichsweise wenig untersucht. Eine Besonderheit ist, dass es ungleich der anderen Sinnessysteme, keinen primären vestibulären Kortex im engeren Sinne hat, sondern multisensorische Informationen in einem bihemisphärischen, multihierarchischen, kortikalen Netzwerk verarbeitet, deren Kernregion beim Menschen in der hinteren Inselregion liegt.

Die erste Publikation untersucht, welche funktionellen Untereinheiten innerhalb des bekannten vestibulären kortikalen Netzwerks eine händigkeitsabhängige Hemisphärendominanz zeigen. Hierfür wurden funktionelle MRT Ruhenetzwerke innerhalb bekannter vestibulärer Kortexareale von 60 gesunden Probanden (30 Rechtshändern, 30 Linkshändern) durch eine unabhängige Komponentenanalyse in ihre funktionellen Untereinheiten geteilt und in Abhängigkeit der Händigkeit untersucht. Diese funktionellen Untereinheiten unterschieden sich bezüglich ihrer Hemisphärensymmetrie und ihrer funktionellen Vernetzung sowohl zu den übrigen Hirnarealen als auch untereinander. Symmetrische Subareale waren multifunktional, ubiquitär und gut mit den übrigen, insbesondere dem visuellen und auditorischen, Kortexarealen vernetzt. Asymmetrische Subareale dagegen lateralisierten auf die nicht-dominante Hemisphäre (bei Rechtshändern auf die rechte Hemisphäre und bei Linkshändern auf die Linke), waren funktional spezialisierter und befanden sich in der mittleren, posterioren und inferioren Insel. Damit ließ sich ein bihemisphärisches, multisensorisches, multifunktionelles vestibuläres kortikales Netzwerk darstellen, welches um eine funktional spezialisierte Kernregion organisiert ist. Ein genaues Verständnis der funktionellen Organisation des vestibulären Systems ist entscheidend, um zentrale vestibuläre Läsionen, wie zum Beispiel im Rahmen eines Schlaganfalls, besser zu verstehen und behandeln zu können.

In der zweiten Publikation wurden strukturelle periphere vestibuläre Veränderungen bei Patienten mit Vestibularisparoxysmie untersucht. Bei der Vestibularisparoxysmie kommt es zu einer ephaptischen Erregung des VIII. Hirnnerven, wahrscheinlich bedingt durch einen pathologischen Gefäß-Nerven-Kontakt im Bereich des Nerveneintritts in den Hirnstamm. In dieser Arbeit wurden die funktionellen und strukturellen Auswirkungen dieses Kontakts auf den VIII. Hirnnerven und das Innenohr untersucht. Im Vergleich zu den gesunden Kontrollen konnte bei Patienten mit Vestibularisparoxysmie strukturelle Unterschiede des betroffenen Nervs sowie eine Asymmetrie des endolymphatischen Raums nachgewiesen werden. Die Krankheitsdauer und die Gesamtzahl der Schwindelattacken korrelierten positiv mit der verminderten strukturellen Integrität des Nervus vestibulocochlearis. Darüber hinaus wurden Korrelationen zwischen der Entfernung der neurovaskulären Kompression zur Wurzeintrittszone im Hirnstamm und der audiovestibulären Funktion, dem Verlust der Nervenintegrität und dem Volumen des endolymphatischen Raums festgestellt. Dies lässt auf eine erhöhte Empfindlichkeit des Nervus vestibulocochlearis bei neurovaskulärer Kompression in der Nähe der Wurzeintrittszone schließen. Daneben könnte der Winkel des Nervs zum Gefäß die Spezifität des Gefäß-Nerven-Kontakts bei der Diagnosestellung erhöhen.

4. Abstract

This doctoral thesis uses structural and functional magnetic resonance imaging (MRI) in combination with electrophysiological and behavioral parameters or in contrast to a diseased cohort to examine the central (publication 1) and peripheral (publication 2) vestibular system. The vestibular system is comparatively less understood. Unlike other sensory systems, the vestibular system lacks a primary cortex. Instead, multisensory information in humans is processed in a bihemispheric multihierarchical cortical network organized around a core region in the posterior insular region.

The first publication investigates which functional subunits within the known vestibular cortical network show a handedness-dependent hemisphere dominance. For this purpose, functional MRI resting networks within known vestibular network areas of 60 healthy participants (30 right-handed, 30 left-handed) were divided into further subunits using independent component analysis. These functional subunits differed regarding their hemispheric symmetry and functional connectivity both to the other brain areas and to each other. Symmetrical subareas were multifunctional, ubiquitous, and well-connected to the other (primarily visual and auditory) cortex areas. Asymmetric subareas, on the other hand, lateralized to the non-dominant hemisphere (right hemisphere in right-handers and left hemisphere in left-handers), were more functionally specialized and located in the middle, posterior, and inferior insula. This allowed the depiction of a bihemispheric, multisensory, multifunctional vestibular cortical network organized around a functionally specialized core region. A detailed understanding of the functional organization of the vestibular system is critical to better understand and treat central vestibular lesions, such as those seen in the context of stroke.

The second publication studies structural peripheral changes in patients with vestibular paroxysmia. Vestibular paroxysmia is caused by an ephaptic excitation of the VIIIth cranial nerve, most likely due to a pathological vessel-nerve contact in the area of nerve entry into the brainstem. This work investigated the functional and structural effects of this contact on the VIIIth cranial nerve and the inner ear. Compared with healthy controls, structural differences of the affected nerve and asymmetry of the endolymphatic space were demonstrated in patients with vestibular paroxysmia. Disease duration and total number of vertigo attacks correlated positively with reduced structural integrity of the vestibulocochlear nerve. In addition, correlations were found between the distance of neurovascular compression to the root entry zone in the brainstem and audiovestibular function, loss of nerve integrity, and volume of the endolymphatic space, suggesting increased susceptibility of the vestibulocochlear nerve to pathologic neurovascular compression near the root entry zone. Besides, the angle of the nerve to the vessel might increase the specificity of vascular-nerve contact in diagnosis. To better understand peripheral vestibular disorders, it is essential to gain a clear differentiation and a comprehensive understanding between pathologic and aetiologic changes.

5. Publikation I - Handedness-dependent functional organizational patterns within the bilateral vestibular cortical network revealed by fMRI connectivity based parcellation

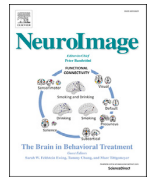
Kirsch V, Boegle R, Keeser D, Kierig E, Ertl-Wagner B, Brandt T, Dieterich M. Handedness-dependent functional organizational patterns within the bilateral vestibular cortical network revealed by fMRI connectivity based parcellation. *Neuroimage*. 2018 Sep;178:224-237. doi: 10.1016/j.neuroimage.2018.05.018. Epub 2018 May 19. PMID: 29787866.



Contents lists available at ScienceDirect

NeuroImage

journal homepage: www.elsevier.com/locate/neuroimage



Handedness-dependent functional organizational patterns within the bilateral vestibular cortical network revealed by fMRI connectivity based parcellation



V. Kirsch^{a,b,c,*}, R. Boegle^{b,c,1}, D. Keeser^{d,e}, E. Kierig^{a,c}, B. Ertl-Wagner^{c,d,g}, T. Brandt^{c,f}, M. Dieterich^{a,b,c,g}

^a Department of Neurology, Ludwig-Maximilians Universität, Munich, Germany

^b Graduate School of Systemic Neuroscience, Ludwig-Maximilians Universität, Munich, Germany

^c German Center for Vertigo and Balance Disorders-IFB^{LMU}, Ludwig-Maximilians Universität, Munich, Germany

^d Department of Radiology, Ludwig-Maximilians Universität, Munich, Germany

^e Department of Psychiatry, Ludwig-Maximilians Universität, Munich, Germany

^f Clinical Neuroscience, Ludwig-Maximilians Universität, Munich, Germany

^g Munich Cluster for Systems Neurology (SyNergy), Munich, Germany

ARTICLE INFO

Keywords:

Vestibular cortical network
Asymmetry
Multisensory
Hemisphere dominance
Functional parcellation
Lateralization

ABSTRACT

Current evidence points towards a vestibular cortex that involves a multisensory bilateral temporo-parietal-insular network with a handedness-dependent hemispheric lateralization. This study aimed to identify handedness-dependent organizational patterns of (lateralized and non-lateralized) functional subunits within the human vestibular cortex areas. 60 healthy volunteers (30 left-handed and 30 right-handed) were examined on a 3T MR scanner using resting state functional MRI (fMRI). The data was analyzed in four major steps using a functional connectivity based parcellation (fCBP) approach: (1) independent component analysis (ICA) on a whole brain level to identify different resting state networks (RSN); (2) creation of a vestibular informed mask from four whole brain ICs that included reference coordinates of the vestibular network extracted from meta-analyses of vestibular neuroimaging experiments; (3) Re-ICA confined to the vestibular informed mask; (4) cross-correlation of the activated voxels within the vestibular subunits (parcels) to each other (P-to-P) and to the whole-brain RSN (P-to-RSN).

This approach disclosed handedness-dependency, inter-hemispheric symmetry, the scale of connectedness to major whole brain RSN and the grade of spatial overlap of voxels within parcels (common/unique) as meaningful discriminatory organizational categories within the vestibular cortex areas. This network consists of multiple inter-hemisphere symmetric (not lateralized), well-connected (many RSN-assignments) multisensory areas (or hubs; e.g., superior temporal gyrus, temporo-parietal intersection) organized around an asymmetric (lateralized, “dominant”) and functionally more specialized (few RSN-assignments) core region in the parieto-insular cortex. The latter is in the middle, posterior and inferior insula. In conclusion, the bilateral cortical vestibular network contains not only a handedness-dependent lateralized central region concentrated in the right hemisphere in right-handers and left hemisphere in left-handers, but also surrounding inter-hemisphere symmetric multisensory vestibular areas that seem to be functionally influenced by their neighboring sensory systems (e.g., temporo-parietal intersection by the visual system). One may speculate that the development of an asymmetrical organized vestibular subsystem reflects a more recent phylogenetic evolution of various multisensory vestibular functions. The right hemispheric dominance of spatial orientation and its disorders, spatial neglect and pusher syndrome, may serve as examples.

* Corresponding author. Department of Neurology, University Hospital, Ludwig Maximilian University Munich, Marchioninistraße 15, 81377, Munich, Germany.
E-mail address: valerie.kirsch@med.lmu.de (V. Kirsch).

¹ These authors contributed equally.

<https://doi.org/10.1016/j.neuroimage.2018.05.018>

Received 13 March 2018; Received in revised form 2 May 2018; Accepted 5 May 2018

Available online 19 May 2018

1053-8119/© 2018 Published by Elsevier Inc.

Introduction

The vestibular cortex differs from other sensory cortices. Lacking a primary cortex in the narrower sense, the vestibular system relies on a network involving multiple multisensory vestibular cortical areas in both hemispheres organized around a core region in the posterior insula and retroinsular region, called the parieto-insular vestibular cortex (PIVC) in monkeys (Guldin and Grüsser, 1998). This network seems to be very similar in humans with the posterior insula, retro-insular region, and operculum 2 (OP2) representing the main components of said core region (Guldin and Grüsser, 1998; Brandt and Dieterich, 1999; Zu Eulenburg et al., 2012; Lopez et al., 2012). Another important feature of the vestibular system is a hemispheric asymmetry, namely the dominance of the ipsilateral hemisphere in relation to handedness (Dieterich et al., 2003). Further, there is a preference of the ipsilateral ascending projections from the stimulated ear (Bense et al., 2003; Dieterich et al., 2017), and a reciprocal inhibitory visual-vestibular interaction disclosed by functional imaging (Brandt et al., 1998; Brandt et al., 2002, 2003; Wenzel et al., 1996).

The vestibular cortical network relies on vestibular, visual, and somatosensory inputs in monkeys (Guldin et al., 1992; Chen et al., 2011a) and humans (Baumgärtner et al., 2010; Bucher et al., 1998; Dieterich et al., 1998; Emri et al., 2003; Fasold et al., 2002; Konen and Kastner, 2008). These multisensory inputs converge at multiple levels from the brain stem to the cortex: reflexive sensorimotor control of eyes, head, and body at the brain stem/cerebellar level; perception of self-motion and control of voluntary movement and balance at the cortical/subcortical level; and higher vestibular cognitive functions (e.g., spatial memory and navigation) at the cortical level (Dieterich and Brandt, 2015). This varying multisensory information is centrally computed, both bilaterally (Dieterich and Brandt, 2015) and hierarchically (Chen et al., 2010). It converges (Chen et al., 2011a; Carriot et al., 2013) in multiple spatially distributed (Brandt and Dieterich, 1999; Lopez and Blanke, 2011) and spatially tuned (Chen et al., 2011b) cortical areas. Within these areas both multimodal neurons as well as a mixture of multiple unimodal neuronal populations have been found in monkeys (Guldin et al., 1992; Yang et al., 2011; Dokka et al., 2015). Consequently, a binary understanding that allocates one specific label to one specific cortical area will most likely not do justice to the vestibular cortical network, especially at the scale being assessed by functional MRI (fMRI) (Logothetis, 2012, 2002; Tolia et al., 2005).

Resting state fMRI provides proxies of dynamic neuronal interactions that are thought to reflect mixtures of various cognitive processes and physiological factors (Buckner et al., 2008; Fox and Raichle, 2007; Smith et al., 2009). Functional connectivity based parcellation (fCBP) approaches oftentimes use independent component analysis (ICA) on resting state fMRI to divide a region of interest (ROI) into distinct sub-regions (Eickhoff et al., 2015; Kim et al., 2010). An fCBP approach that is restricted to a specific mask is then able to identify even more discrete functional subunits within this region (Kim et al., 2013; Mars et al., 2012; Smith et al., 2015). Most fCBP approaches then use a binary allocation of one label/parcel per voxel (Craddock et al., 2012; Neubert et al., 2014; Thirion et al., 2014). However, ICA naturally allows a multivariate (non-binary) separation of linear mixtures of signal sources that temporally correlate and spatially overlap (Beckmann and Smith, 2004). This non-binary methodical approach might be able to reflect multiple signals at the same spatial location, e.g., in multiple populations of neurons or a single multisensory population and might therefore be insightful when dealing with the vestibular system.

This study aimed to identify handedness-dependent organizational patterns of functional subunits within the human vestibular cortex areas whilst addressing its multisensory (non-binary) nature. To that end, 60 healthy volunteers (30 left-handed and 30 right-handed) were analyzed using masked ICA approaches resulting in binary and non-binary results. This mask was data-driven (composed of whole brain independent components) and specific to the vestibular cortical system as the

independent components (ICs) used had to include vestibular reference coordinates derived from two meta-analyses of vestibular neuroimaging experiments pinpointing the vestibular cortex (Lopez et al., 2012; Zu Eulenburg et al., 2012).

Materials and methods

Subjects

Institutional Review Board (IRB) approval was obtained prior to the initiation of the study. Each participant provided informed oral and written consent in accordance with the Declaration of Helsinki. 30 healthy right-handed (RH) volunteers (17 females; aged 20–67 years, mean age $26,7 \pm 8,3$ years) and 30 healthy left-handed (LH) volunteers (14 females; aged 20–65 years, mean age $26,1 \pm 8,6$ years) were included in the study. LH and RH were age- and gender-matched. The laterality handedness quotient was assessed with the 10-item inventory of the Edinburgh test (Oldfield, 1971; Salmasso and Longoni, 1985). The inclusion criterion was age between 18 and 70 years. Exclusion criteria were a history of any neurological, vestibular, and/or psychiatric disorder, pregnancy, and MR-related contraindications such as cardiac pacemakers, ferromagnetic implants, or claustrophobia.

Measurement of the semicircular canal and otolith functions

The integrity of vestibular function was ascertained by assessing the semicircular canal function with the head-impulse test for the vestibulo-ocular reflex (VOR) and otolith function with the determination of the subjective visual vertical (SVV). The head-impulse test (Halmagyi and Curthoys, 1988) was measured using high-frame-rate video-oculography (VOG) with the EyeSeeCam (Schneider et al., 2009; EyeSeeTech, Munich, Germany). A median gain during head impulses < 0.8 (eye velocity in $^{\circ}/s$ divided by head velocity in $^{\circ}/s$) was considered the criterion for a pathological VOR and exclusion of the subject. A tilt of the SVV is a sensitive sign of a graviceptive vestibular tone imbalance, assessed when sitting in an upright position in front of a half-spherical dome with the head fixed on a chin rest (for details see Dieterich and Brandt, 1993). A mean deviation of $> 2.5^{\circ}$ from the true vertical was considered a pathological tilt of SVV. None of the participants showed deficits of the VOR or pathological tilts of the SVV.

MR imaging protocol

MR imaging data were acquired in a whole-body 3.0 Tesla MR scanner (Magnetom Verio, Siemens Healthcare, Erlangen, Germany) with a 32-channel head coil. Intrinsic brain activity was assessed with BOLD fMRI based on a T2*-weighted echo-planar imaging (EPI) sequence with a $3.0 \times 3.0 \times 3.0$ mm³ isotropic resolution (TE = 30 ms, TR = 3000 ms, 200 frames per subject). No other task was required except keeping the eyes closed, remaining still without focusing the thoughts on anything specific and not falling asleep. Anatomical images included a T1-weighted magnetization-prepared rapid gradient echo (MP-RAGE) sequence with a field-of-view of 256 mm and an isotropic spatial resolution of $1.0 \times 1.0 \times 1.0$ mm³ (TE 4.37 ms, TR = 2100 ms, number of slices 160). Images in DICOM format were converted to the Nifti-file format (using MRICron dcm2nii).

Preprocessing of fMRI data

All acquired images were preprocessed using the SPM12 software package, DARTEL (Diffeomorphic Anatomical Registration Through Exponentiated Lie algebra; Ashburner, 2007; Ashburner and Friston, 2011), CONN functional connectivity toolbox v15 (Whitfield-Gabrieli and Nieto-Castanon, 2012), whole brain ICA as well as dual regression as implemented in the FSL toolbox MELODIC (Beckmann and Smith, 2004; Beckmann et al., 2005; Filippini et al., 2009), and in-house scripts written

in MATLAB (MathWorks Inc., Natick, MA, USA) as previously described in (Cyran et al., 2016). Anatomical analyses in DARTEL included: *i*) segmentation of the images into white matter (WM), gray matter (GM), and cerebrospinal fluid (CSF) using the New Segmentation algorithm implemented in SPM12 and including an intensity non-uniformity correction to account for smooth intensity variations caused by gradient distortions; *ii*) application of the DARTEL approach for registration, normalization, and modulation; *iii*) further normalization of the GM and WM images to MNI space; and smoothing of the GM and WM images with an 4 mm full width at half maximum Gaussian kernel to increase signal to noise ratio. In the resulting images, each voxel represented an absolute amount of brain volume, equivalent to the brain volume per unit prior to normalization. Functional analyses in CONN included: *j*) import of the preprocessed anatomical volumes; *jj*) spatial preprocessing of functional volumes [slice-timing correction, realignment, normalization and smoothing (4-mm FWHM Gaussian filter) using SPM12 default parameter choices]; and *jjj*) temporal preprocessing of the resulting residual BOLD time series using a band-pass filter ($0.008 \text{ Hz} < f < 0.09 \text{ Hz}$). ICA-based denoising included: *k*) group ICA to distinguish noise and signal sources in the fMRI data; *kk*) dual-regression to generate individual contributions per subject for all independent components allowing for the separation of noise and signal on the

individual subject level even if noise and signal sources are correlated and *kkk*) subtraction of the components that were judged by visual inspection to be noise of each respective subject as previously described (Cyran et al., 2015).

For a flowchart of the functional connectivity based parcellation (fCBP) methods used please view Fig. 1. Please note that supplementary data was converted into a Data in Brief article (Kirsch et al., 2018), which is referred to frequently in the following.

Whole brain ICA

An 80 dimensional group ICA (Craddock et al., 2012) was performed on denoised fMRI data (LH and RH combined) using a whole brain mask (Calhoun et al., 2001; Beckmann and Smith, 2004; Beckmann et al., 2005). The dimensionality of the ICA was estimated by the FSL MELODIC default method using the Laplace approximation to the Bayesian evidence of the model order (Beckmann and Smith, 2004).

Each independent component (IC) was semi-automatically labeled to the 20 resting state network (RSN) atlas proposed by Laird et al. (2011) using the highest product between the highest voxel-overlap (Dice-Coefficient) and the highest absolute correlation (spatial overlap and distribution of statistical values). The Laird atlas contains a full functional

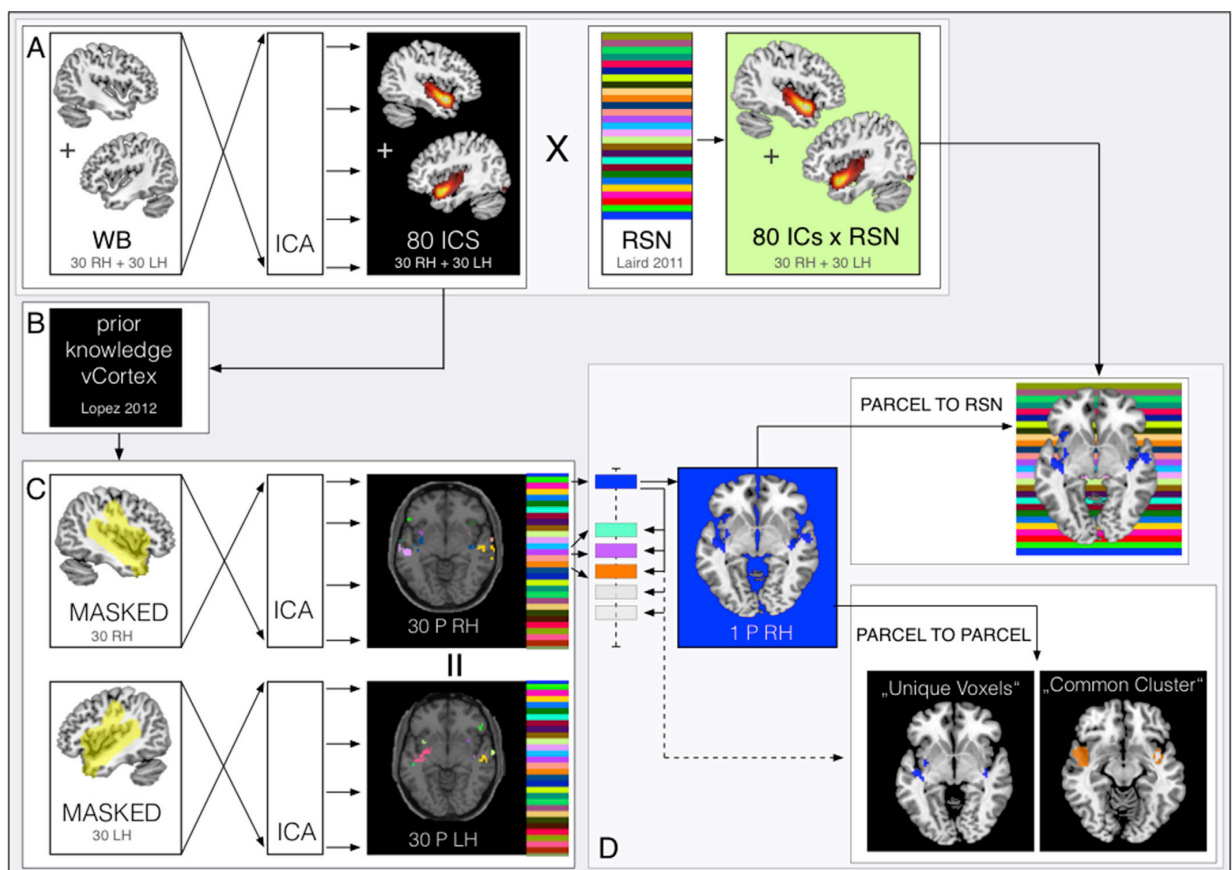


Fig. 1. Flowchart of the used fCBP (functional connectivity based parcellation) methods used. The data was analyzed in four major steps: [A] whole brain (WB) binary fCBP using independent component analysis (ICA) to identify different resting state networks (RSN) and their behavioral interpretations according to (Laird et al., 2011); [B] creation of a vestibular informed mask from four whole brain ICs that included reference coordinates of the vestibular network extracted from meta-analyses of vestibular neuroimaging experiments; [C] masked binary fCBP using Re-ICA confined to the vestibular informed mask; [D] masked non-binary fCBP using cross-correlation of the activated voxels within the vestibular subunits (parcels = P) to each other to differentiate between “common” or “unique” voxels (Parcel-to-Parcel) and to the whole-brain RSN (Parcel-to-RSN). Note, that the colored RSN background in (A) corresponds to one specific RSN (of 27) to which the depicted IC was labeled to. In (C) and (D) every parcel has its own discriminative color that is independent of the RSN colors. This changes in “Parcel to RSN”, where each parcel is correlated with the whole brain RSN. Black and white background means no allocation to RSN. This system was followed throughout this work.

explication of RSN intrinsic connectivity at a standard low order decomposition using a neuroinformatics approach based on the Brain-Map behavioral taxonomy as well as a stratified, data-driven ordering of cognitive processes. This enabled us to group the networks (ICs) we found to specific brain functions (i.e., 73 of 80 or 91.25% of ICs were assigned to 20 maps- and task-correlations taken from Laird and coauthors).

ICs that did not fit the Laird components (overall 7 of 80 or 8.75% of ICs) were checked visually and assigned to an anatomical label of the

“Harvard-Oxford cortical structural atlas”. Here, sound behavioral interpretations to each IC (network) were determined by inserting their maximum xyz-MNI-coordinates into the large-scale, automated synthesis of the human functional neuroimaging data platform Neurosynth (neurosynth.org), using a radius of 4 mm (Yarkoni et al., 2011). For an overview of all RSN composed of 80 whole brain ICs see Fig. 2. For more detail on the RSN please view Fig. 1 in the respective Data in Brief article (Kirsch et al., 2018).



Fig. 2. Overview of the whole brain (WB) functional connectivity based parcellation (fCBP) and the vestibular informed mask. 80 whole brain (WB) independent components (ICs) were labeled to 27 resting state networks (RSNs). Every RSN was color-coded and can be viewed in the color-scale on the left of the figure. The background-color of each IC conforms to the color of the RSN it was labeled to. This enables a quick overview of both resulting ICs and their respective RSN. For an overview of the RSNs view Fig. 1 in the respective Data in Brief article (Kirsch et al., 2018). Within the figure four whole brain ICs (IC1, IC3, IC13, IC58) are highlighted. These ICs included vestibular reference coordinates and were combined to create the vestibular informed mask at the bottom right of the figure.

Vestibular informed mask

To refine the identification of vestibular subunits the functional connectivity based parcellation (fCBP) was confined to a vestibular informed mask (Mars et al., 2012; Kim et al., 2013; Smith et al., 2015). To ensure a data-driven logic, four whole brain independent components (IC1, IC3, IC13, IC58) that included vestibular reference coordinates of two meta-analyses of vestibular neuroimaging experiments attempting to pinpoint the vestibular cortex (Lopez et al., 2012; Zu Eulenburg et al., 2012) were thresholded and combined to create a vestibular informed mask surrounding the sylvian fissure (cf. Fig. 2). The mask included cortical areas, such as the anterior, middle and posterior insula, retro-insular cortex, parietal operculum (OP1-4), superior temporal gyrus (STG) and inferior parietal lobule (IPL). Note that cerebellar or subcortical areas that are known to be involved in vestibular processing, as well as cortical areas located around the longitudinal cerebral fissure (such as the precuneus and the anterior cingulum) were not included in the mask, since we wanted to keep our analyses both data-driven and spatially confined.

Masked ICA

Resting-state functional connectivity based parcellation (fCBP) oftentimes uses independent component analysis (ICA) and divides any given region of interest (ROI) into distinct functional sub-units according to common spatio-temporal patterns of BOLD signal fluctuations that are maximally independent from each other. For this study two variations of ICA were used. One variation, the more traditional (binary) ICA approach, where each functional sub-unit must be spatially distinct (and voxels are forced to choose a sub-unit; cf. method section ‘masked binary ICA’); and the second variation, a multivariate (non-binary) ICA approach where functional-subunits can overlap (and voxels can be part

of multiple sub-units with their various behavioral interpretations; method section ‘masked non-binary ICA’). Note, fCBP was restricted to a vestibular informed mask (cf. method section ‘vestibular informed mask’).

Masked binary ICA

ICA with 30 dimensions was run separately for LH and RH denoised fMRI data within the vestibular informed mask (see Fig. 2). The dimensionality was chosen to avoid overfitting whilst extracting a reasonable number of parcels within the mask (Gursoy and Niebur, 2005; Särelä and Vigário, 2001). The mask restricted ICA had roughly 9000 voxels for the estimation of independence between sources, while the whole brain ICA had roughly 90000 voxels. We chose to be conservative with the number of dimensions and used the estimate provided by Särelä and coauthors (Särelä and Vigário, 2001) whilst adding another factor of 1/2. A binary fCBP approach as described by Kim et al. (2013) was chosen. Here, each voxel is allocated exactly one label (or parcel) in terms of its maximally significant weight (“modulations of spatial component map (significance values)” multiplied by “extent of time course modulations”). This approach binarizes the parcel identity of every voxel and ignores all other significant overlaps in favor of the most significant one and results in spatially distinct functional sub-units or parcels (cf. Fig. 3). Parcels were anatomically characterized using the Harvard- Oxford structural cortical atlas (Desikan et al., 2006; Makris et al., 2006) and the Juelich histological cyto- and myeloarchitectonic atlas (Eickhoff et al., 2005, 2007).

In order to be able to compare LH and RH parcels we had to find analogous binary parcels between LH and RH. Analogous binary parcels were determined by multiplication of the highest Dice-coefficient (voxel-overlap measure) and the absolute spatial correlation coefficient (correlation of spatial independent component maps). This approach was successful for interhemispheric symmetric parcels, but not for interhemispheric asymmetric parcels. Here, the parcels needed to be spatially flipped (mirrored) to correspond between LH and RH. This was done

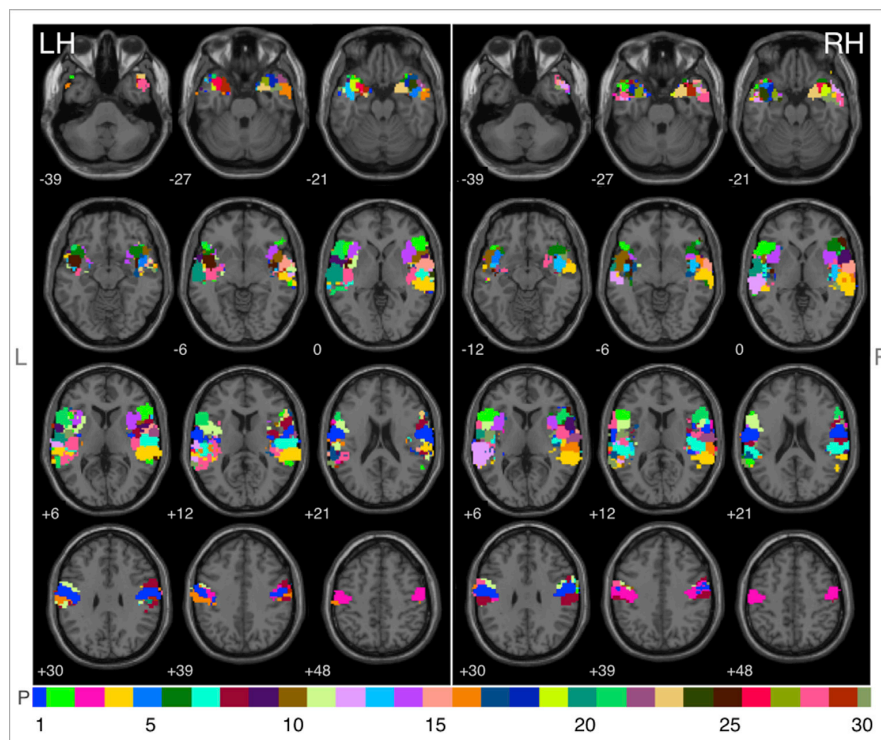


Fig. 3. Masked binary ICA summary maps of 30 left-handed (LH) and 30 right-handed (RH) healthy volunteers (FDR<0.01). Each of the 30 parcels (P) was assigned to a separate color (cf. color scale), which was the same for LH and RH subgroups. Anatomical assignments can be viewed in the respective Data in Brief article (Kirsch et al., 2018).

with respect to the x-axis, i.e., hemisphere-flip in x-direction in MNI-space (cf. Fig. 4 for a comparison of “raw” and “flipped” ICs for LH and RH). A complete overview of each “raw” symmetric and asymmetric parcel can be viewed in Fig. 2 of the respective Data in Brief article (Kirsch et al., 2018).

Handedness-dependency of a parcel was calculated using a laterality-index based on the number of voxels within a parcel $[(R-L)/(R+L)] \times 100$. If the laterality-index per parcel and between LH and RH changed in a concordant fashion it was termed handedness-independent (-). An inverse laterality-index was termed handedness-dependent (+).

Masked non-binary ICA

ICA allows a non-binary (multivariate) separation of linear mixtures of signal sources that temporally correlate and spatially overlap (Beckmann and Smith, 2004). The non-binary (multivariate) fCBP approach uses this non-orthogonal ICA feature to investigate meaningful commonalities and differences (cross-correlation) between functional subunits in space (Parcel-to-Parcel) and time (Parcel-to-RSN).

For the “Parcel-to-RSN correlations” time courses of the 30 binary parcels were correlated to the 27 whole brain RSN (cf. method section ‘whole brain ICA’) to enable their functional mapping following Laird’s atlas (Laird et al., 2011) and/or Yarkonis “Neurosynth.org” platform (Yarkoni et al., 2011). Time courses of each parcel and each RSN were extracted separately from the functional data of each subject using dual regression (Beckmann et al., 2009; Filippini et al., 2009) and correlated to each other on a subject-by-subject basis. The correlation coefficients were transformed to z-scores using Fisher’s r-to-z transformation, and then tested on group-level.

For the “Parcel-to-Parcel correlations” spatial overlap between the voxels of the 30 parcels was investigated. “Common clusters” or “unique voxels” could be distinguished. “Common clusters” (C) were defined as voxels that spatially overlapped between parcels. “Unique voxels” (U) were defined as voxels that were part of one parcel only and surpassed 15 voxels of cluster size. To visualize the “common” voxels, 9 groups of 2–6

parcels (“common clusters”) were defined via spatial overlap. Finally, the time course of each “common cluster” and each RSN was extracted via dual regression on subject-basis, correlated and analyzed on group-level based on the regression coefficients. For more detail on the RSN please view Fig. 1 in the respective Data in Brief article (Kirsch et al., 2018).

Statistics and map display

All IC maps were thresholded to $p > 0.5$ for the alternative hypothesis test using the Gaussian/gamma mixture model approach implemented in MELODIC (Beckmann and Smith, 2004, 2005; Cole et al., 2010). Time courses for all components (80 whole brain ICs, 30 parcels, 9 “common clusters”) were created using dual regression on the fMRI data (Beckmann et al., 2009; Filippini et al., 2009). All correlations were calculated on a subject-by-subject basis from these dual regression stage 1 time courses. The correlation coefficients were then transformed to z-scores using Fisher’s r-to-z transformation, and then tested on the group-level. The resulting connectivity matrices were thresholded using false discovery rate (FDR) $q < 0.01$ to correct for multiple comparisons. See also method section ‘masked non-binary ICA’ above.

Statistics of behavioral data and number of RSN-assignments were performed using the IBM SPSS Statistics software package (Version 20).

Results

Handedness and integrity of vestibular function

LH and RH healthy volunteers did not differ significantly in terms of age or gender (*t*-test, two-tailed, $p > 0.5$). The laterality quotient for right-handedness as per the 10-item inventory of the Edinburgh test was +100% in 27 of the RH volunteers, +90% in two and +80% in one. The laterality quotient for left-handedness was -100% in 15, -90% to -80% in 12 and -70% to 65% in 3 of the 30 LH volunteers. None of the participants showed pathological tilts of the SVV or deficits of the VOR in

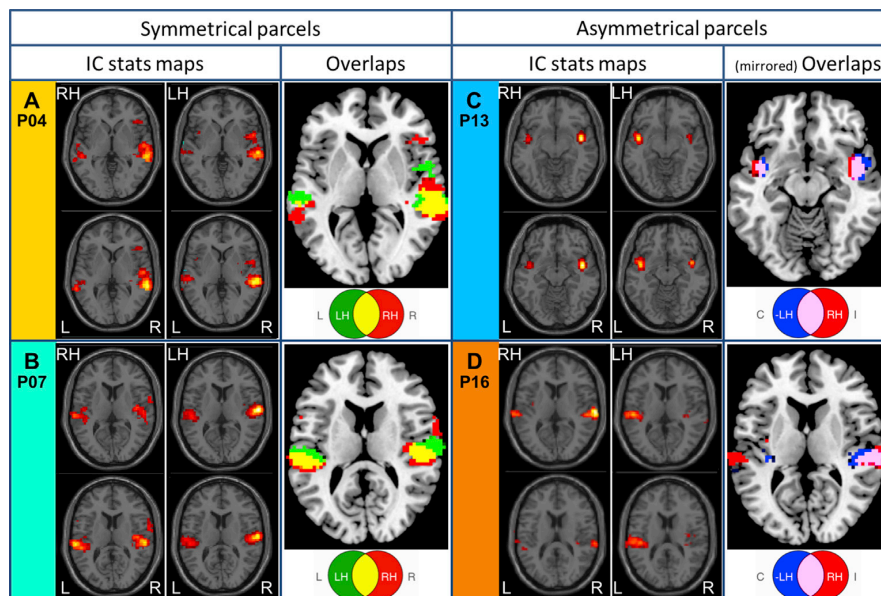


Fig. 4. Exemplary display of parcel symmetry relationships for left-handed (LH) and right-handed (RH) subjects. Hemisphere symmetrical (shown in A & B) and hemisphere asymmetrical (shown in C & D) parcels between LH and RH are shown in their “raw” statistical independent component map form and the final combined overlay indicating overlaps of LH and RH via color mixing to illustrate what an overlap entails. Hemisphere asymmetrical parcels (P13 and P16 shown in C & D) required mirroring of one of the patterns of the LH or RH to generate a meaningful overlap of LH and RH, therefore all voxels of the LH were mirrored with respect to the midline, i.e. left and right side of the LH were flipped for these parcels. In all overlays the left side of cortex is displayed on the left, indicated by “L” and the right side or cortex is displayed on the right indicated by “R”. In the final overlay showing the overlap via color mixing for the case of the asymmetrical parcels (P13 and P16 shown in C & D) this labeling is changed to ipsilateral “I” and contralateral “C”, due to overlay of RH with the midline-flipped LH. Note that ipsilateral (I) therefore indicates the right side for the RH and left side for the LH (now flipped to the right for maximum overlap, i.e. a hemisphere asymmetrical parcel). A complete overview of each “raw” symmetric and asymmetric parcel can be viewed in Fig. 2 in the respective Data in Brief article (Kirsch et al., 2018).

head impulse testing. Therefore, 60 participants were included in the analyses as the study cohort. Head motion measured by the mean relative displacement (in mm) was low for both RH (0.09 ± 0.16) and LH (0.09 ± 0.09) and did not differ significantly between groups.

Whole brain ICA

The whole brain 80-dimensional ICA decomposition (cf. Fig. 2) was semi-automatically labeled to the 20 resting state network (RSN) atlas (and its behavioral interpretations) proposed by Laird et al. (2011). These were 73 of the 80 ICs (or 91.25% of ICs), which were assigned to 20 maps and task-correlations taken from Laird and coauthors. Seven further networks (i.e., 7 of 80 or 8.75% of ICs) were anatomically labeled using the “Harvard-Oxford cortical structural atlas” and functionally characterized using the large-scale, automated synthesis of human functional neuroimaging data platform Neurosynth (neurosynth.org). For more detail please see Fig. 1 in the respective Data in Brief article (Kirsch et al., 2018).

Masked binary ICA

Masked binary fCBP revealed 30 parcels for each group of LH and RH (Fig. 3), which were matched spatially. This enabled a differentiation between 17 “symmetrical” and 13 “asymmetrical” parcels (Fig. 5) regarding hemispherical distribution of voxels. **Symmetrical parcels** (P1, P3-4, P6-9, P11-12, P14-15, P20, P22-23, P25, P28, P30) showed high spatial overlap between LH and RH volunteers (Fig. 5A). **Asymmetrical parcels** (P2, P5, P10, P13, P16-19, P21, P24, P26-27, P29) needed to be flipped (cf. method section ‘masked binary ICA’) to view analogous “hemispherical distributional” results of LH and RH (cf. Fig. 5B). The laterality-index of most parcels was handedness-dependent. Eleven parcels were handedness-independent (P3, P4, P7-8, P11-12, P15, P20, P22-23, P30). Anatomical characterization of the 30 parcels can be viewed in of the respective Data in Brief article (Kirsch et al., 2018).

Masked non-binary ICA

Masked non-binary (multivariate) fCBP enabled the investigation of interdependencies in between the 30 parcels (*P-to-P correlations*) and in relation to the whole brain RSNs (*P-to-RSN correlations*).

P-to-RSN correlations

The number of RSN assignments to each parcel (“P-to-RSN correlations” Fig. 3 of in the respective Data in Brief article (Kirsch et al., 2018). did not differ between LH ($1-20$; 10 ± 7 SD) and RH ($2-19$; 11 ± 5 SD). However, spatially symmetrical parcels had significantly more RSN assignments (LH 13 ± 6 SD; RH 13 ± 5 SD) than asymmetrical parcels (LH 6 ± 6 SD; RH 8 ± 4 SD) using two-sampled t-tests ($p < 0.001$). There was a total of 18 parcels with ≤ 12 RSN assignments (P2, P4, P5, P8, P13, P16-19, P21, P23-30), and 12 parcels with ≥ 12 RSN assignments (P1, P3, P6, P7, P9-12, P14, P15, P20, P22).

The parcels were subsequently categorized by means of “spatial symmetry” and “number of Parcel-to-RSN correlations”. This resulted in two different types of parcels: “asymmetrical and less connected” and “symmetrical and connected”. Furthermore “P-to-RSN correlations” enabled a functional mapping per Laird’s “Behavioral Interpretations of Intrinsic Connectivity Networks” (2011; cf. method section ‘whole brain ICA’) or per Yarkonis “Neurosynth.org” platform (Yarkoni et al., 2011). For overview-purposes the parcels were further grouped using the pre-dominant anatomical landmark:

Type 1: “Asymmetrical and less connected” (Fig. 5). This parcel (P) type was spatially asymmetrical and correlated with fewer than 12 RSN:

- **Group “IFG” (inferior frontal gyrus; P2, P21)** included primarily BA 44 and BA45 and showed an asymmetry toward the dominant hemisphere (left in RH and right LH). The correlations with the whole brain RSN systems suggest a connection with language, speech and working memory functions, as inferred from the function assignments of the Laird’s atlas and the extracted functions from the neurosynth.org database (Laird et al., 2011; Smith et al., 2009; Yarkoni et al., 2011).
- **Group “S/MTG” (superior and middle temporal gyrus; P4)** included primarily the superior and middle temporal gyri. The correlations with the whole brain RSN systems suggest a connection with hearing, specifically spatial hearing, motion and spatial localization functions, as inferred from the function assignments of the Laird’s atlas and the extracted functions from the neurosynth.org database (Laird et al., 2011; Smith et al., 2009; Yarkoni et al., 2011).
- **Group “middle and posterior insula” (P5, P13, P17, P25, P28, P30)** included asymmetrical and symmetrical parcels around the posterior insula (Id1, Ig2). Asymmetrical parcels (P5, P13, P17) tended toward the non-dominant hemisphere (right in RH and left LH). Symmetrical parcels (P25, P28, P30) correlated with more RSNs and/or included the inferior parietal lobule (IPL; P28, P30), secondary somatosensory cortex (P28, P30) or the primary auditory cortex and BA45 (P25). The correlations with the whole brain RSN systems suggest a connection with multimodal processing of the vestibular system supporting a multitude of behaviors by providing vestibular coordinates and self-monitoring functions. The behaviors include balance, spatial orientation, spatial coordinate transformation for perception (e.g. spatial hearing) and behavior (Brandt and Dieterich, 1999; Lopez et al., 2012; Zu Eulenburg et al., 2012) and as inferred from the function assignments of the Laird’s atlas and the extracted functions from the neurosynth.org database (Laird et al., 2011; Smith et al., 2009; Yarkoni et al., 2011).
- **Group “inferior insula” (P18, P19, P23-24, P26-27, P29) included contralateral asymmetrical (P18, P24, P27), ipsilateral asymmetrical (P19, P26, P29) and one symmetrical (P23) parcel** including the hippocampus. The correlations with the whole brain RSN systems suggest a connection with spatial orientation, spatial reasoning, coordinate transformation and further vestibular coordinate input processing functions (Brandt and Dieterich, 1999; Lopez et al., 2012; Zu Eulenburg et al., 2012) and as inferred from the function assignments of the Laird’s atlas and the extracted functions from the neurosynth.org database (Laird et al., 2011; Smith et al., 2009; Yarkoni et al., 2011).

Most of the parcels listed under type 1 “asymmetrical and less connected” were part of known hemisphere-lateralized (asymmetrical, dominant) and mostly handedness-dependent brain functions such as speech and language (group “IFG” including Broca’s area), and vestibular sensory processing and/or vestibular coordinate transformation (group “middle, posterior and inferior insula”). To put it more simply, these parcels seemed to show preponderance for converging sense-specific information and functions for other systems, i.e. they specialize in abstractions of sensory information. For more detail please see in the respective Data in Brief article (Kirsch et al., 2018).

Type 2: “Symmetrical and connected” (cf. Fig. 5). The parcels of this group were spatially symmetrical and correlated with more than 12 RSN.

- **Group “anterior insula” (P6, P14)** included symmetrical parcels around the anterior insula with some involvement of BA44, the frontal orbital cortex and temporal pole. The correlations with the whole brain RSN systems suggest a connection with attentional salience and adaptive cognitive control of cognition and behavior, as inferred from the function assignments of the Laird’s atlas and the

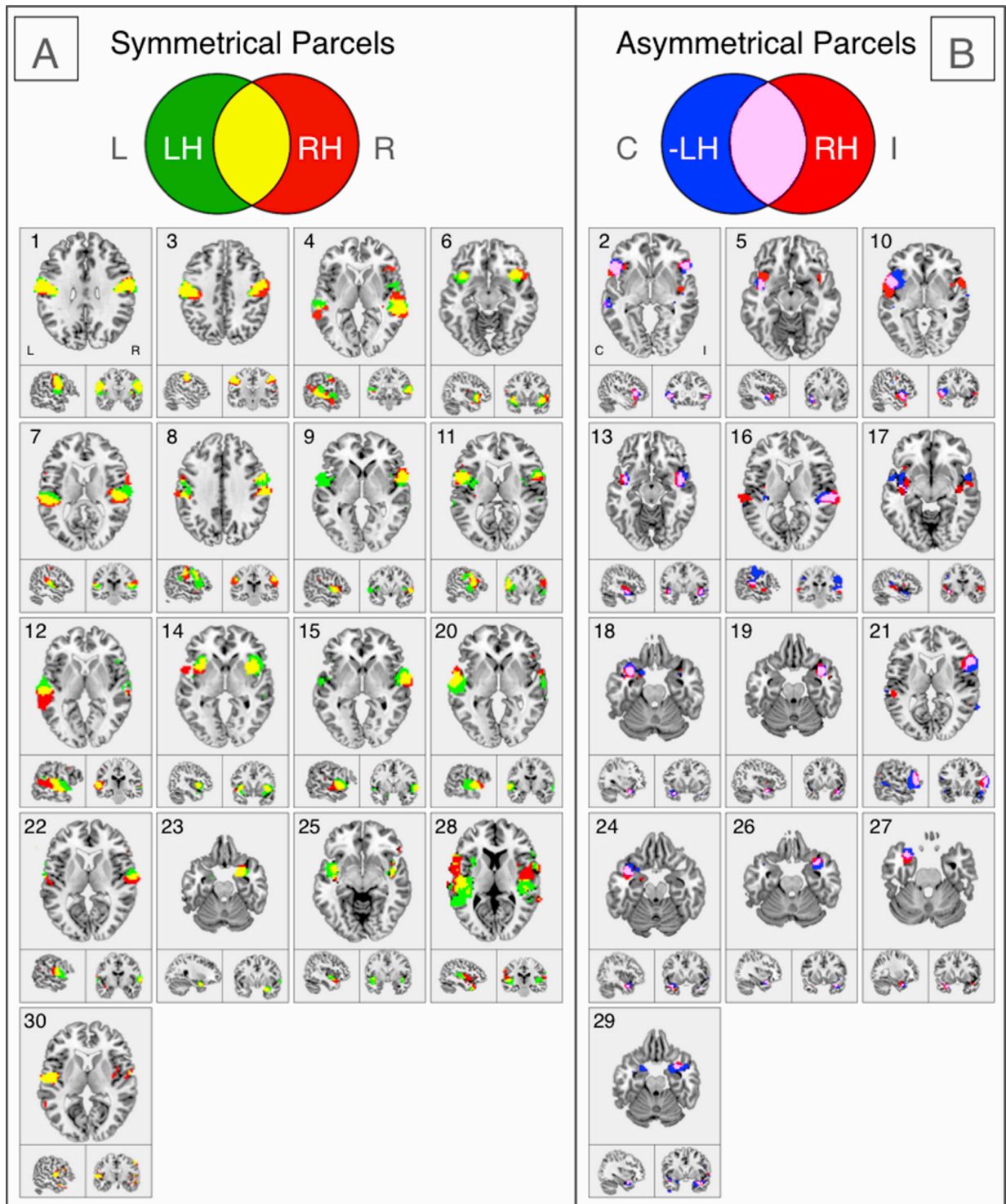


Fig. 5. Masked binary ICA single maps of 30 left-handed (LH) and 30 right-handed (RH) healthy volunteers enabled a differentiation between “symmetrical” and “asymmetrical” parcels ($FDR < 0.01$). In **symmetrical parcels** (5A) LH (green) and RH (red) parcels seemed to mostly overlap spatially (yellow; L = left; R = right). In **asymmetrical parcels** (5B) LH (blue) and RH (red) parcels seemed to inversely overlap spatially (pink). Here LH maps were flipped to depict the overlap (C = contralateral; I = ipsilateral). Anatomical assignments can be viewed in the respective Data in Brief article (Kirsch et al., 2018).

extracted functions from the neurosynth.org database (Laird et al., 2011; Smith et al., 2009; Yarkoni et al., 2011).

- **Group “sensorimotor” (P1, P3)** included symmetrical parcels with both somatosensory (BA1, BA3a + b) and motor (BA4a + p, BA6) cortical areas. The correlations with the whole brain RSN systems suggest a connection with adaptive transformation of sensory percept into motor responses for head, eye, torso and limb coordination and prediction of sensory percept, as inferred from the function assignments of the Laird’s atlas and the extracted functions from the neurosynth.org database (Laird et al., 2011; Smith et al., 2009; Yarkoni et al., 2011).
- **Group “STG” (superior temporal gyrus; P10, P12, P15, P16, P20, P22)** included foremost and bilaterally the superior temporal gyrus (STG) in combination with the primary auditory cortex (P7), inferior parietal lobule (P7, P8, P11), BA44 (P11, P9) and/or secondary somatosensory cortex (P7, P8, P9) and motor cortex (P8, P11). The correlations with the whole brain RSN systems suggest a connection with hearing (tone and pitch discrimination), speaker identification, attended speech identification/separation, touch, pain, visceral sensation and tactile attention, as inferred from the function assignments of the Laird’s atlas and the extracted functions from the neurosynth.org database (Laird et al., 2011; Smith et al., 2009; Yarkoni et al., 2011).
- **Group “temporo-parietal” (P7, P8, P9, P11)** included areas in the intersection between the temporal and parietal lobe. The correlations with the whole brain RSN systems suggest a connection with the combination of limbic, visual, auditory and somatosensory percept in self-reference and localization of self-other relationships, as well as reflective thinking, interoception and theory of mind, as inferred from the function assignments of the Laird’s atlas and the extracted functions from the neurosynth.org database (Laird et al., 2011; Smith et al., 2009; Yarkoni et al., 2011).

Parcels listed under type 2 “Symmetrical and connected” were inter-hemispheric symmetrical (balanced) parcels that were highly connected (with widespread RSN correlations). In contrast to type 1 parcels, which were more specialized and lateralized between hemispheres and seemed to converge information streams. These type 2 symmetric highly

connected nodes modulate, combine, and redistribute more abstract functions and integrative processing. Note that these regions are also thought to be part of the network hubs in the human brain (Eguíluz et al., 2005; Achard et al., 2006; Breakspear et al., 2007) that are suggested to be functionally valuable for integrative information processing (Buckner et al., 2009; van den Heuvel et al., 2012; Crossley et al., 2013). In addition, these parcels seem to be functionally influenced by the neighboring sensory systems (e.g., temporo-parietal intersection by the visual system, superior temporal gyrus by the auditory system). For more detail please see in the respective Data in Brief article (Kirsch et al., 2018).

P-to-P correlations

The multivariate masked fCBP enabled the distinction of spatial uniqueness and commonality of independent components that form parcels. “Unique voxels” and “common clusters” voxels within the parcels were subsequently differentiated.

“Unique voxels” (cf. Fig. 6A). Unique voxels (U) within a parcel area are characterized by unique spatial assignment with no overlaps. A detailed overview of the “unique” voxels is provided in the respective Data in Brief article (Kirsch et al., 2018).

The categorization of the parcels by means of “hemispheric symmetry” and “number of parcels to systems correlations” remained stable when only considering the unique voxels within the parcels. Most parcels in RH (besides 6: U13, U18-19, U24, U26, U29) showed unique voxels, whereas in LH only 50% of the parcels (U5-6, U9-10, U12, U15, U18-19, U20, U22, U24-26, U29-30) showed unique voxels. When present, unique voxels within parcels overall contained less than half or 1/3 of the voxel count of the entire parcels, indicating that many spatial overlaps occurred between parcels. In general, the anatomical labeling remained stable for unique voxel parcels with only slight shifts in the percentage of represented topographies. Handedness-dependency remained stable (with only U16 changing its handedness-dependency). Note, that within key structures of the vestibular system the ipsilateral handedness-dependency was concentrated in the inferior insula (U28) and less in the posterior insula (U28, U17).

“Common clusters” (cf. Fig. 6B). Common clusters were defined as voxels

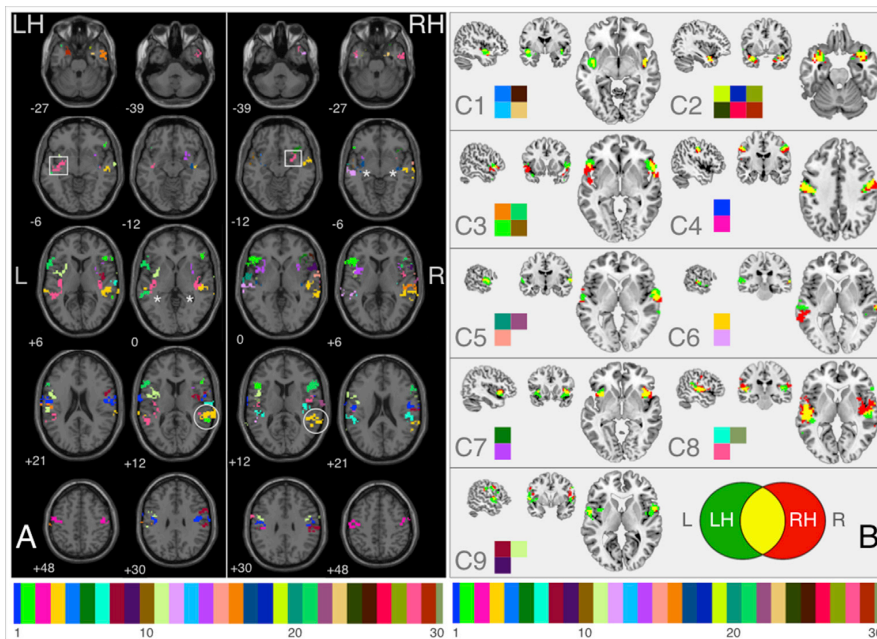


Fig. 6. Masked non-binary ICA maps revealed “unique” voxels (6A; FDR<0.01; >15 voxels) and “common” clusters (6B; FDR<0.01). The x-axis shows the color scale of the 30 binary parcels (cf. Fig. 3), each of which was assigned to a separate color (cf. color scale), and the colors matched between LH and RH subgroups. Handedness-dependency remained stable (with only U16 changing its handedness-dependency). Within key structures of the vestibular system the ipsilateral handedness-dependency was concentrated in the inferior insula (square around U28) and less in the posterior insula (bilateral stars in U28, U17). Note that the right-sided handedness-independent area within the temporo-parietal region (circle, U4) was the same area, which was activated in a patient suffering from repetitive room-tilt-illusions (Kirsch et al., 2017). “Common clusters” consisted of 2–6 parcels. For a quick overview, each cluster was characterized by an assembly of its color-coded parcels. Here LH (green) and RH (red) parcels seemed to mostly overlap spatially (yellow). For more detailed characterization please see in the respective Data in Brief article (Kirsch et al., 2018).

that overlapped in between parcels. To enable visualization of the “common” voxels, 9 groups of 2–6 spatially similar parcels (“common clusters”; C) were defined and correlated to whole brain RSNs. Fig. 4 in the respective Data in Brief article (Kirsch et al., 2018) provides a detailed overview of the common clusters.

Common clusters were spatially symmetrical, which indicate regions of multiple coexisting patterns of functional connectivity, i.e. due to multiple neuronal populations. Common clusters were equally represented for LH and RH. Apart from C1 “posterior insula” and C2 “inferior insula”, common clusters correlated with more than 5 RSN “systems”, which indicate manifold functionality. The rough anatomical labeling (e.g., inferior insula”, “posterior insula”) remained stable.

Discussion

Identification of handedness-dependent organizational patterns of functional subunits within the human vestibular cortex areas was possible by addressing its multisensory (non-binary) nature. To this end a masked non-binary functional connectivity based parcellation (fCBP) approach was introduced. Meaningful discriminatory organizational categories were handedness-dependency, inter-hemispheric symmetry, the scale of connectedness to major whole brain RSN (P-to-RSN correlations) and the grade of spatial overlap of voxels within parcels (P-to-P correlations).

These categories revealed a familiar handedness-dependent bilateral vestibular network of multiple asymmetric and symmetric multisensory areas organized around a core region in the parieto-insular cortex, i.e., the middle, posterior and inferior insula. This core region was hemispherically lateralized (asymmetric, dominant), functionally more specialized (fewer RSN-assignments) and multisensory in nature (see ‘core regions’ in Fig. 7 A). Its surrounding areas (e.g., STG, TP intersection, cf. ‘hub regions’ in Fig. 7A) were hemispherically symmetric (balanced,

equal), well-connected (more RSN-assignments) and functionally influenced by the neighboring sensory systems (e.g., TP by the visual system, STG by the auditory system). Within these fundamentally different types of functional units, overlapping (“common” voxels) or specific (“unique” voxels) subunits could be distinguished.

In the following we speculate if this might reflect different neuronal populations within a functional subunit and possible advantages of a non-binary methodical approach. Then characteristics of the cortical core and surrounding vestibular areas are related to previous animal and human studies. Finally, we discuss phylogenetic evolution as a possible key to understanding the systematic “otherness” of the vestibular system, as well as the method and its limitations within this study.

A non-binary parcellation approach for a non-binary sensory system

The vestibular system can be considered non-binary in many respects, most notably when considering the multisensory nature of motion stimuli of the individual (Angelaki and Cullen, 2008; Goldberg et al., 2012; Carriot et al., 2015) and their bilateral (Dieterich and Brandt, 2015) and hierarchical (Chen et al., 2010) computation that converge (Chen et al., 2011a; Carriot et al., 2013) in multiple spatially distributed (Brandt and Dieterich, 1999; Lopez and Blanke, 2011) and spatially tuned (Chen et al., 2011b) cortical areas. In addition, within these areas both multimodal neurons and a mixture of multiple unimodal neuronal populations have been found in monkeys (Guldin et al., 1992; Yang et al., 2011; Dokka et al., 2015).

The non-binary parcellation approach identified multiple overlapping as well as unique voxels within all subunits in both right-handed (RH) and left-handed (LH) healthy volunteers. These heterogeneous differences within one parcellated functional unit that processes vestibular information might reflect different types of neurons (uni- or multimodal), different intersections or constellations of neuronal populations (one or

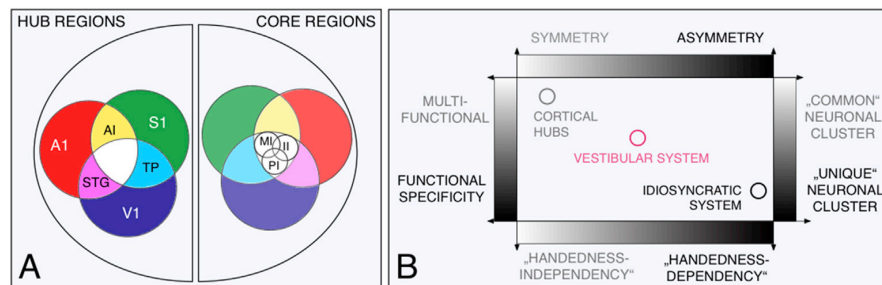


Fig. 7. Quality of hub and core regions within vestibular cortex areas. (A) Masked binary and non-binary functional connectivity based parcellation (fCBP) revealed handedness-dependent organizational patterns within the vestibular cortical network. This network bi-hemispherically consists of multiple symmetric and asymmetric multisensory areas (=hubs), such as STG (superior temporal gyrus), TP (temporo-parietal intersection) and AI (anterior insula). These hubs are organized around a core region in the parieto-insular cortex, i.e. middle (MI), posterior (PI) and inferior insula (II). Note, that similar to a chromatic circle, the involved vestibular cortex area (resulting color) depends on the modality and mixture of used stimuli (colors) and are influenced by the neighboring sensory system (color). Similarities to a Venn diagram are unintentional. (B) This approach disclosed Functional specificity (“P-to-RSN correlations”), hemispherical symmetry, grade of spatial overlap of neuronal populations (common/unique; “P-to-P correlations”) and handedness-dependency as meaningful discriminatory organizational categories. At its extremities lie multifunctional, symmetrical, commonness of neuronal populations and handedness-independent cortical hubs (such as TP) or functional specific, asymmetric, uniqueness of neural populations and handedness-dependent idiosyncratic systems (such as language or higher visual functions). Within this diagram the vestibular system occupies an intermediate position.

multiple) or different hierarchies of signal processing within a functional unit (Smith et al., 2009; Van Essen and Glasser, 2014; Amunts and Zilles, 2015; Glasser et al., 2016). Consequently, this non-binary approach provides new insight into the organization of functional specialization in lateralized multisensory cortical areas like the vestibular cortical network. Such organization might be underestimated or even not detected in a solely binary approach.

The vestibular cortical surrounding areas: interhemispheric balanced and integrative hubs

Unlike other sensory systems, brain activation studies with PET and fMRI in humans (Suzuki et al., 2001; Fasold et al., 2002; Emri et al., 2003; Lopez and Blanke, 2011) and tracer and electrophysiological studies in animals (Angelaki and Cullen, 2008; Büttner and Büttner, 1978; Grüsser et al., 1990a; Odkvist et al., 1974; Phillips et al., 1971; Rancz et al., 2015) suggest that the vestibular system has no primary cortex area in the narrower sense. Instead, it consists of a bilateral cortical network of neuronal populations in various cortical areas, primarily in the parietal and temporal cortex. Robust parts of this network are the “*symmetrical and connected*” superior temporal gyrus (STG), inferior parietal lobule (IPL) and anterior insula, which process vestibular information (Phillips et al., 1971; Odkvist et al., 1974; Büttner and Büttner, 1978; Bense et al., 2001) depending on the modality and mixture of stimuli (Chen et al., 2010, 2011b; Klingner et al., 2013). One might speculate that these interhemispheric balanced (symmetric) regions serve as integrative hubs to a core region in the parieto-insular cortex (Frank et al., 2014). Fittingly, these integrative hubs seem to be functionally influenced by the neighboring sensory systems (e.g. temporo-parietal intersection by the visual system, superior temporal gyrus by the auditory system).

Note that most of these regions are also thought to be part of the network hubs in the human brain (van den Heuvel and Sporns, 2011; 2013); a minority might be high-degree (highly connected) hub nodes (Eguíluz et al., 2005; Achard et al., 2006; Breakspear et al., 2007) that mediate many of the long-distance connections between brain modules (Zamora-López et al., 2010) and are suggested to be functionally valuable for integrative information processing (Buckner et al., 2009; van den Heuvel et al., 2012; Crossley et al., 2013).

The vestibular cortical core region: a hemispherically asymmetric and specialized network

The most robust vestibular cortical structures in human brain lesion and activation studies, as well as tracer and electrophysiological studies in animals include the “*asymmetrical and less connected*” middle, posterior, inferior insula and retroinsular cortex (Figs. 5B and 7A, Table 2A in the respective Data in Brief article). This region is referred to as the parieto-insular vestibular cortex (PIVC) in monkeys (Akbarian et al., 1993; Brandt and Dieterich, 1999; Guldin and Grüsser, 1998). The cortical processing of vestibular information in monkeys and humans (Dieterich et al., 2003, 2005; Chen et al., 2010) is multisensory (Grüsser et al., 1990a, 1990b; Guldin and Grüsser, 1998) and asymmetric. This might explain its intermediate position with regard to RSN connectiveness between the primary sensory cortex and the integrative hubs (cf. ‘*hub regions*’ in Fig. 7A). Notably, robust optic flow and vestibular tuning were found in an area strongly interconnected with the PIVC, at the posterior end of the sylvian fissure in the visual posterior sylvian area (VPS) of macaque monkeys, which receives projections from a visual area, the dorsal medial superior temporal area (MSTd) (Chen et al., 2011a). These data, as well as a comparison of vestibular spatiotemporal tuning in macaque cortical areas PIVC, VIP, and MSTd, suggest there is a hierarchy in the cortical processing of vestibular information, i.e., the PIVC is most proximal to the vestibular periphery and the MSTd most distal (Chen et al., 2011b). The importance of this area in the posterior operculo-insular complex for vestibular processing is also evident in humans (Baier et al., 2013, 2012; Brandt et al., 1994; Ionta et al., 2011;

Kaski et al., 2016; Lopez et al., 2012; Zu Eulenburg et al., 2012).

The asymmetry (network lateralization) and handedness-dependency displayed in our functional subunits might reflect the presumed hemispheric dominance (network lateralization) towards the non-dominant (concerning handedness) hemisphere (Dieterich et al., 2003; Janzen et al., 2008; Karnath and Dieterich, 2006; Nigmatullina et al., 2015; Zu Eulenburg et al., 2012), i.e. dominance of the right hemisphere in right-handers. Fittingly, the other asymmetric functional subunit in our analysis was the inferior frontal lobule (IFL) including Broca’s area BA44 and BA45 with its known hemispheric dominance (network lateralization) towards the dominant hemisphere (concerning handedness) (Jakobsen et al., 2016; Oliveira et al., 2016; Rasmussen and Milner, 1977), i.e. dominance of left hemisphere in right-handers.

Another remarkable finding was the inclusion of the inferior insula in our asymmetric network of vestibular core regions; however, it had fewer RSN-assignments than the middle and posterior insula. This might support earlier findings in humans that inferred that the inferior insula was an important and probably thalamus-independent (Dieterich et al., 2005; Kirsch et al., 2016) central target station for incoming vestibular information. DTI tractography of vestibular brainstem pathways revealed (Dieterich et al., 2017) that cortical vestibular dominance is not a distinct cortical phenomenon but is closely linked to a vestibular input dominance, which builds up in the upper brainstem and is functionally mirrored in an ipsilateral handedness-dependency in the inferior insula.

A phylogenetic view of the organizational patterns found in the vestibular cortical network

The need for fast, efficient information processing despite (functional) brain expansion during evolution (Preuss, 2011; Sherwood et al., 2012) is thought to have led to both lateralization and specialization (Levy, 1969; Ringo et al., 1994). One may speculate that the separation of a symmetrically from an asymmetrically organized vestibular system reflects a phylogenetic evolution of various multisensory vestibular functions. Here the vestibular system takes an intermediary position. This view supports the concept that “symmetry”, “handedness-independency”, “multifunctionality” and “commonness of neuronal populations” point to one system with an infrastructure based on brain hubs (cf. ‘*hub regions*’ in Fig. 7A). In contrast, “asymmetry” (or lateralization or dominance), “handedness-dependency”, functional specificity” and “uniqueness of neuronal population” rather point toward a phylogenetically “idiosyncratic” system (cf. ‘*core regions*’ in Fig. 7A), such as the establishment of language or higher visual functions (cf. Fig. 7B).

A symmetrically organized phylogenetically “older” system seems to have been further developed by an additional asymmetric lateralized “younger” system chiefly localized in the parieto-insular region. Asymmetry developed together with sensorimotor specialization of handedness and orientation (Brandt and Dieterich, 2015), both of which are based on different spatial reference frames: handedness (e.g., manipulation of objects) mainly on an ego-centric and orientation of the individual in space mainly on an allo-centric reference frame. Note, that within key structures of the vestibular system the ipsilateral handedness-dependency was concentrated in the inferior insula and less in the posterior insula (cp. Fig. 6A). One possible explanation for the patterns of handedness-dependency from bottom to top might be that the vestibular system lateralizes before the motor system and pre-determines the lateralization of phylogenetically later developing cognitive functions including its own higher functions (Brandt and Dieterich, 2017).

Methodological limitations

There are several methodical limitations in our study that need to be considered in the interpretation of the data: First, we used ICA because it allows the separation of overlapping sources. However, it is currently unclear how multiple populations of neurons or a multisensory population should be separated in fMRI data. For example, there may be many

V. Kirsch et al.

NeuroImage 178 (2018) 224–237

non-linearities in neuronal interaction and transformation into a hemodynamic signal mixture that cannot be captured by linear ICA unmixing algorithms. Second, a general problem with ICA is the initialization of the algorithm using a random seed and the possibility of arriving at different solutions in each run. A deterministic algorithm might be preferable if it can also distinguish overlapping sources. Third, assignments of parcels into “common” clusters were mainly driven by anatomical location. A self-organizing collection of ICs into groups of spatially overlapping and interacting regions would allow an operator-independent summary. Fourth, it is unclear how changes in the number of components would change the assignments of the parcels and therefore the grouping of unique and common clusters. Currently, we chose the number of components in such a way as to avoid overfitting and instability of the ICA results. This needs to be investigated further, and would also benefit from a deterministic algorithm that would also generate the number of parcels independent of the user choice. At this point we can only point to the results of Abou-Elseoud and coworkers (Abou-Elseoud et al., 2009; Abou-Elseoud et al., 2011) who showed for whole brain ICA that increases in model-order leads to splits in some components but not in others and that if splits occur then they seem to follow underlying functions and are not arbitrary. Fifth, it is possible that the non-binary ICA-based approach might be specific to the problem of separating highly multisensory regions. Generally, parcellation should be considered as a strongly context-dependent endeavor where methods used for different questions will not show converging results, but different functional aspects of the whole system (Hauois, 2012). This is not due to methodical limitations, but relates to the fact that the brain is fundamentally fuzzy due to the dense causal nature of structure-function relationships. Sixth, our method, as well as, “classical” functional connectivity clustering methods and border detection methods are dependent on thresholding which introduces degree-vagueness as differences between parcels depend also on the chosen threshold and thresholding method. Seventh, other cortex areas involved in vestibular processing such as the precuneus and the anterior cingulum were not represented within our mask, since we wanted to keep our analyses both data-driven and spatially confined.

Conclusion

In conclusion, the bilateral vestibular cortical network should be understood as an agglomeration of (for the most part) handedness-dependent multiple interhemispheric symmetric (balanced) integrative hub areas that surround an asymmetric (lateralized, dominant) multisensory core region in the parieto-insular cortex, and with the inferior insula as a target station for incoming lateralized vestibular information. One may speculate that lateralized hemispheric function such as speech, handedness, and higher cortical (cognitive) vestibular functions (e.g., large-scale spatial orientation) reflect the most recent evolutionary developments. Lateralization of multisensory vestibular function has implications for neurological disorders: The frequency and severity of hemispatial neglect and pusher syndrome which occur with right hemispheric strokes of the middle cerebral artery which supplies the territory of the vestibular insula and parietal operculum.

Conflicts of interest

The authors declare they have no competing financial interests.

Acknowledgments

Partially funded by the Society for the Advancement of Science and Research at the Medical Faculty of the Ludwig Maximilians University Munich (Verein zur Förderung von Wissenschaft und Forschung an der Medizinischen Fakultät der Ludwig-Maximilians Universität München), the Graduate School of Systemic Neurosciences (GSN), the German Foundation for Neurology (Deutsche Stiftung für Neurologie, DSN), the Hertie Foundation and the German Federal Ministry of Education and

Research (German Center for Vertigo and Balance Disorders -IFB^{LMU}, Grant code 01EO140). This is a part of the dissertation of E. Kierig. We thank Judy Benson, Marie Cheetham and Katie Göttinger for copy-editing the manuscript.

References

- Abou-Elseoud, A., Starck, T., Remes, J., Nikkinen, J., Tervonen, O., Kiviniemi, V., 2009. The effect of model order selection in group PICA. *Hum. Brain Mapp.* 1216. NA-NA. <https://doi.org/10.1002/hbm.20929>.
- Abou Elseoud, A., Littow, H., Remes, J., Starck, T., Nikkinen, J., Nissilä, J., Timonen, M., Tervonen, O., Kiviniemi, V., 2011. Group-ica model order highlights patterns of functional brain connectivity. *Front. Syst. Neurosci.* 5 (37). <https://doi.org/10.3389/fnsys.2011.00037>.
- Achard, S., Salvador, R., Whitcher, B., Suckling, J., Bullmore, E., 2006. A resilient, low-frequency, small-world human brain functional network with highly connected association cortical hubs. *J. Neurosci.* 26, 63–72. <https://doi.org/10.1523/JNEUROSCI.3874-05.2006>.
- Akbarian, S., Grusser, O.J., Guldin, W.O., 1993. Corticofugal projections to the vestibular nuclei in squirrel monkeys: further evidence of multiple cortical vestibular fields. *J. Comp. Neurol.* 332, 89–104. <https://doi.org/10.1002/cne.903320107>.
- Amunts, K., Zilles, K., 2015. Architectonic mapping of the human brain beyond brodmann. *Neuron* 88, 1086–1107. <https://doi.org/10.1016/j.neuron.2015.12.001>.
- Angelaki, D.E., Cullen, K.E., 2008. Vestibular system: the many facets of a multimodal sense. *Annu. Rev. Neurosci.* 31, 125–150. <https://doi.org/10.1146/annurev.neuro.31.060407.125555>.
- Ashburner, J., 2007. A fast diffeomorphic image registration algorithm. *Neuroimage* 38, 95–113. <https://doi.org/10.1016/j.neuroimage.2007.07.007>.
- Ashburner, J., Friston, K.J., 2011. Diffeomorphic registration using geodesic shooting and Gauss-Newton optimisation. *Neuroimage* 55, 954–967. <https://doi.org/10.1016/j.neuroimage.2010.12.049>.
- Baier, B., Eulenburger, P.Z., Best, C., Geber, C., Müller-Forell, W., Birklein, F., Dieterich, M., 2013. Posterior insular cortex - a site of vestibular-somatosensory interaction? *Brain Behav.* 3, 519–524. <https://doi.org/10.1002/brb3.155>.
- Baier, B., Suchan, J., Karnath, H.O., Dieterich, M., 2012. Neural correlates of disturbed perception of verticality. *Neurology* 78, 728–735. <https://doi.org/10.1212/WNL.0b013e318248e544>.
- Baumgärtner, U., Iannetti, G.D., Zambreanu, L., Stoeter, P., Treede, R.-D., Tracey, I., 2010. Multiple somatotopic representations of heat and mechanical pain in the operculo-insular cortex: a high-resolution fMRI study. *J. Neurophysiol.* 104, 2863–2872. <https://doi.org/10.1152/jn.00253.2010>.
- Beckmann, C.F., DeLuca, M., Devlin, J.T., Smith, S.M., 2005. Investigations into resting-state connectivity using independent component analysis. *Philos. Trans. R. Soc. Lond. B Biol. Sci.* 360, 1001–1013. <https://doi.org/10.1098/rstb.2005.1634>.
- Beckmann, C.F., Mackay, C.E., Filippini, N., Smith, S.M., 2009. Group comparison of resting-state fMRI data using multi-subject ICA and dual regression. *Hum. Brain Mapp. Conf* 181.
- Beckmann, C.F., Smith, S.M., 2005. Tensorial extensions of independent component analysis for multisubject fMRI analysis. *Neuroimage* 25, 294–311. <https://doi.org/10.1016/j.neuroimage.2004.10.043>.
- Beckmann, C.F., Smith, S.M., 2004. Probabilistic independent component analysis for functional magnetic resonance imaging. *IEEE Trans. Med. Imag.* 23, 137–152. <https://doi.org/10.1109/TMI.2003.822821>.
- Bense, S., Bartenstein, P., Lutz, S., Stephan, T., Schwaiger, M., Brandt, T., Dieterich, M., 2003. Three determinants of vestibular hemispheric dominance during caloric stimulation: a positron emission tomography study. *Ann. N. Y. Acad. Sci.* 1004, 440–445. <https://doi.org/10.1111/j.1749-6632.2003.tb00256.x>.
- Bense, S., Stephan, T., Yousry, T.A., Brandt, T., Dieterich, M., 2001. Multisensory cortical signal increases and decreases during vestibular galvanic stimulation (fMRI). *J. Neurophysiol.* 85, 886–899.
- Brandt, T., Dieterich, M., 2017. The dizzy patient: don't forget disorders of the central vestibular system. *Nat. Rev. Neurol.* 13, 352–362. <https://doi.org/10.1038/nrneurol.2017.58>.
- Brandt, T., Dieterich, M., 2015. Does the vestibular system determine the lateralization of brain functions? *J. Neurol.* 262, 214–215. <https://doi.org/10.1007/s00415-014-7548-8>.
- Brandt, T., Dieterich, M., 1999. The vestibular cortex: its locations, functions, and disorders. *Ann. N. Y. Acad. Sci.* 871, 293–312. <https://doi.org/10.1111/j.1749-6632.1999.tb09193.x>.
- Brandt, T., Dieterich, M., Danek, a, 1994. Vestibular cortex lesions affect the perception of verticality. *Ann. Neurol.* 35, 403–412. <https://doi.org/10.1002/ana.410350406>.
- Brandt, T., Bartenstein, P., Janek, A., Dieterich, M., 1998. Reciprocal inhibitory visual-vestibular interaction. Visual motion stimulation deactivates the parieto-insular vestibular cortex. *Brain* 121 (Pt 9), 1749–1758.
- Brandt, T., Glasauer, S., Stephan, T., Bense, S., Yousry, T.A., Deutschlander, A., Dieterich, M., 2002. Visual-vestibular and visuovestibular cortical interaction: new insights from fMRI and pet. *Ann. N. Y. Acad. Sci.* 956, 230–241.
- Brandt, T., Marx, E., Stephan, T., Bense, S., Dieterich, M., 2003. Inhibitory interhemispheric visuovestibular interaction in motion perception. *Ann. N. Y. Acad. Sci.* 1004, 283–288.
- Breakspear, M., Sporns, O., Honey, C.J., Ko, R., 2007. Network structure of cerebral cortex shapes functional connectivity on multiple time scales. *Pnas* 104, 10240–10245. <https://doi.org/10.1073/pnas.0701519104>.

- Bucher, S.F., Dieterich, M., Wiesmann, M., Weiss, A., Zink, R., Yousry, T. a, Brandt, T., 1998. Cerebral functional magnetic resonance imaging of vestibular, auditory, and nociceptive areas during galvanic stimulation. *Ann. Neurol.* 44, 120–125. <https://doi.org/10.1002/ana.410440118>.
- Buckner, R.L., Andrews-Hanna, J.R., Schacter, D.L., 2008. The Brain's default network: anatomy, function, and relevance to disease. *Ann. N. Y. Acad. Sci.* 1124, 1–38. <https://doi.org/10.1196/annals.1440.011>.
- Buckner, R.L., Sepulcre, J., Talukdar, T., Krienen, F.M., Liu, H., Hedden, T., Andrews-Hanna, J.R., Sperling, R. a, Johnson, K. a, 2009. Cortical hubs revealed by intrinsic functional connectivity: mapping, assessment of stability, and relation to Alzheimer's disease. *J. Neurosci.* 29, 1860–1873. <https://doi.org/10.1523/JNEUROSCI.5062-08.2009>.
- Büttner, U., Buettner, U.W., 1978. Parietal cortex (2v) neuronal activity in the alert monkey during natural vestibular and optokinetic stimulation. *Brain Res.* 153, 392–397.
- Calhoun, V.D., Adali, T., Pearlson, G.D., Pekar, J.J., 2001. A method for making group inferences from functional MRI data using independent component analysis. *Hum. Brain Mapp.* 14, 140–151.
- Carriot, J., Brooks, J.X., Cullen, K.E., 2013. Multimodal integration of self-motion cues in the vestibular system: active versus passive translations. *J. Neurosci.* 33, 19555–19566. <https://doi.org/10.1523/JNEUROSCI.3051-13.2013>.
- Carriot, J., Jamali, M., Cullen, K.E., 2015. Rapid adaptation of multisensory integration in vestibular pathways. *Front. Syst. Neurosci.* 9 (59). <https://doi.org/10.3389/fnsys.2015.00059>.
- Chen, A., DeAngelis, G.C., Angelaki, D.E., 2011a. Convergence of vestibular and visual self-motion signals in an area of the posterior sylvian fissure. *J. Neurosci.* 31, 11617–11627. <https://doi.org/10.1523/JNEUROSCI.1266-11.2011>.
- Chen, A., DeAngelis, G.C., Angelaki, D.E., 2011b. A comparison of vestibular spatiotemporal tuning in macaque parietoinsular vestibular cortex, ventral intraparietal area, and medial superior temporal area. *J. Neurosci.* 31, 3082–3094. <https://doi.org/10.1523/JNEUROSCI.4476-10.2011>.
- Chen, A., DeAngelis, G.C., Angelaki, D.E., 2010. Macaque parieto-insular vestibular cortex: responses to self-motion and optic flow. *J. Neurosci.* 30, 3022–3042. <https://doi.org/10.1523/JNEUROSCI.4029-09.2010>.
- Cole, D.M., Smith, S.M., Beckmann, C.F., 2010. Advances and pitfalls in the analysis and interpretation of resting-state fMRI data. *Front. Syst. Neurosci.* 4 (8). <https://doi.org/10.3389/fnsys.2010.00008>.
- Craddock, R.C., James, G.A., Holtzheimer, P.E., Hu, X.P., Mayberg, H.S., 2012. A whole brain fMRI atlas generated via spatially constrained spectral clustering. *Hum. Brain Mapp.* 33, 1914–1928. <https://doi.org/10.1002/hbm.21333>.
- Crosley, N.A., Mechelli, A., Vértes, P.E., Winton-Brown, T.T., Patel, A.X., Ginestet, C.E., McGuire, P., Bullmore, E.T., 2013. Cognitive relevance of the community structure of the human brain functional coactivation network. *Proc. Natl. Acad. Sci. U. S. A* 110, 11583–11588. <https://doi.org/10.1073/pnas.1220826110>.
- Cyran, C.A.M., Boegle, R., Stephan, T., Dieterich, M., Glasauer, S., 2016. Age-related decline in functional connectivity of the vestibular cortical network. *Brain Struct. Funct.* 221, 1443–1463. <https://doi.org/10.1007/s00429-014-0983-6>.
- Cyran, C.A.M., Boegle, R., Stephan, T., Dieterich, M., Glasauer, S., 2015. Age-related decline in functional connectivity of the vestibular cortical network. *Brain Struct. Funct.* <https://doi.org/10.1007/s00429-014-0983-6>.
- Desikan, R.S., Ségonne, F., Fischl, B., Quinn, B.T., Dickerson, B.C., Blacker, D., Buckner, R.L., Dale, A.M., Maguire, R.P., Hyman, B.T., Albert, M.S., Killiany, R.J., 2006. An automated labeling system for subdividing the human cerebral cortex on MRI scans into gyral based regions of interest. *Neuroimage* 31, 968–980. <https://doi.org/10.1016/j.neuroimage.2006.01.021>.
- Dieterich, M., Bartenstein, P., Spiegel, S., Bense, S., Schwaiger, M., Brandt, T., 2005. Thalamic infarctions cause side-specific suppression of vestibular cortex activations. *Brain* 128, 2052–2067. <https://doi.org/10.1093/brain/awh551>.
- Dieterich, M., Bense, S., Lutz, S., Drzezga, a, Stephan, T., Bartenstein, P., Brandt, T., 2003. Dominance for vestibular cortical function in the non dominant hemisphere. *Cerebr. Cortex* 994–1007.
- Dieterich, M., Brandt, T., 1993. Ocular torsion and tilt of subjective visual vertical are sensitive brainstem signs. *Ann. Neurol.* 33, 292–299. <https://doi.org/10.1002/ana.410330311>.
- Dieterich, M., Brandt, T., 2015. The bilateral central vestibular system: its pathways, functions, and disorders. *Ann. N. Y. Acad. Sci.* 1–17. <https://doi.org/10.1111/nyas.12585>.
- Dieterich, M., Bucher, S.F., Seelos, K.C., Brandt, T., 1998. Horizontal or vertical optokinetic stimulation activates visual motion-sensitive, ocular motor and vestibular cortex areas with right hemispheric dominance. An fMRI study. *Brain* 121 (Pt 8), 1479–1495. <https://doi.org/10.1093/brain/121.8.1479>.
- Dieterich, M., Kirsch, V., Brandt, T., 2017. Right-sided dominance of the bilateral vestibular system in the upper brainstem and thalamus. *J. Neurol.* 1–8. <https://doi.org/10.1007/s00415-017-8453-8>.
- Dokka, K., DeAngelis, G.C., Angelaki, D.E., 2015. Multisensory integration of visual and vestibular signals improves heading discrimination in the presence of a moving object. *J. Neurosci.* 35, 13599–13607. <https://doi.org/10.1523/JNEUROSCI.2267-15.2015>.
- Eguíluz, V.M., Chialvo, D.R., Cecchi, G.A., Baliki, M., Apkarian, A.V., 2005. Scale-free brain functional networks. *Phys. Rev. Lett.* 94 (18102). <https://doi.org/10.1103/PhysRevLett.94.018102>.
- Eickhoff, S.B., Paus, T., Caspers, S., Grosbras, M.H., Evans, A.C., Zilles, K., Amunts, K., 2007. Assignment of functional activations to probabilistic cytoarchitectonic areas revisited. *Neuroimage* 36, 511–521. <https://doi.org/10.1016/j.neuroimage.2007.03.060>.
- Eickhoff, S.B., Stephan, K.E., Mohlberg, H., Grefkes, C., Fink, G.R., Amunts, K., Zilles, K., 2005. A new SPM toolbox for combining probabilistic cytoarchitectonic maps and functional imaging data. *Neuroimage* 25, 1325–1335. <https://doi.org/10.1016/j.neuroimage.2004.12.034>.
- Eickhoff, S.B., Thirion, B., Varoquaux, G., Bzdok, D., 2015. Connectivity-based parcellation: critique and implications. *Hum. Brain Mapp.* 36, 4771–4792. <https://doi.org/10.1002/hbm.22933>.
- Emri, M., Kisely, M., Lengyel, Z., Balkay, L., Márián, T., Mikó, L., Berényi, E., Sziklai, I., Trón, L., Tóth, A., 2003. Cortical projection of peripheral vestibular signaling. *J. Neurophysiol.* 89, 2639–2646. <https://doi.org/10.1152/jn.00599.2002>.
- Fasold, O., von Brevern, M., Kuhberg, M., Ploner, C.J., Villringer, A., Lempert, T., Wenzel, R., 2002. Human vestibular cortex as identified with caloric stimulation in functional magnetic resonance imaging. *Neuroimage* 17, 1384–1393 (pii). <https://doi.org/S1053811902912413>.
- Filippini, N., MacIntosh, B.J., Hough, M.G., Goodwin, G.M., Frisoni, G.B., Smith, S.M., Matthews, P.M., Beckmann, C.F., Mackay, C.E., 2009. Distinct patterns of brain activity in young carriers of the APOE-epsilon4 allele. *Proc. Natl. Acad. Sci. U. S. A* 106, 7209–7214. <https://doi.org/10.1073/pnas.0811879106>.
- Fox, M.D., Raichle, M.E., 2007. Spontaneous fluctuations in brain activity observed with functional magnetic resonance imaging. *Nat. Rev. Neurosci.* 8, 700–711 (pii). <https://doi.org/10.1038/nrn2201>.
- Frank, S.M., Baumann, O., Mattingley, J.B., Greenlee, M.W., 2014. Vestibular and visual responses in human posterior insular cortex. *J. Neurophysiol.* 112, 2481–2491. <https://doi.org/10.1152/jn.00078.2014>.
- Glasser, M.F., Coalson, T.S., Robinson, E.C., Hacker, C.D., Harwell, J., Yacoub, E., Uğurbil, K., Andersson, J., Beckmann, C.F., Jenkinson, M., Smith, S.M., Van Essen, D.C., 2016. A multi-modal parcellation of human cerebral cortex. *Nature*. <https://doi.org/10.1038/nature18933>.
- Goldberg, J., Wilson, V., Cullen, K., Angelaki, D., Broussard, D., Büttner-Ennever, J., Fukushima, K., Minor, L., 2012. The Vestibular System. A Sixth Sense. Oxford University Press, New York.
- Grüsser, O.J., Pause, M., Schreiter, U., 1990a. Vestibular neurones in the parieto-insular cortex of monkeys (*Macaca fascicularis*): visual and neck receptor responses. *J. Physiol.* 430, 559–583.
- Grüsser, O.J., Pause, M., Schreiter, U., 1990b. Localization and responses of neurones in the parieto-insular vestibular cortex of awake monkeys (*Macaca fascicularis*). *J. Physiol.* 430, 537–557.
- Guldin, W.O., Akbarian, S., Grüsser, O.J., 1992. Cortico-cortical connections and cytoarchitectonics of the primate vestibular cortex: a study in squirrel monkeys (*Saimiri sciureus*). *J. Comp. Neurol.* 326, 375–401. <https://doi.org/10.1002/cne.903260306>.
- Guldin, W.O., Grüsser, O.J., 1998. Is there a vestibular cortex? *Trends Neurosci.* 21, 254–259. [https://doi.org/10.1016/S0166-2236\(97\)01211-3](https://doi.org/10.1016/S0166-2236(97)01211-3).
- Gursoy, E., Niebur, D., 2005. Impact of sample size on ICA-based harmonic source estimation. In: *Proc. 13th Int. Conf. Intell. Syst. Appl. to Power Syst. ISAP'05 2005*, pp. 123–127. <https://doi.org/10.1109/ISAP.2005.1599251>.
- Halmagyi, G.M., Curthoys, I.S., 1988. A clinical sign of canal paresis. *Arch. Neurol.* 45, 737–739.
- Hauens, P., 2012. The fuzzy brain. Vagueness and mapping connectivity of the human cerebral cortex. *Front. Neuroanat.* 6, 1–11. <https://doi.org/10.3389/fnana.2012.00037>.
- Ionta, S., Heydrich, L., Lenggenhager, B., Mouthon, M., Fornari, E., Chapuis, D., Gassert, R., Blanke, O., 2011. Multisensory mechanisms in temporo-parietal cortex support self-location and first-person perspective. *Neuron* 70, 363–374. <https://doi.org/10.1016/j.neuron.2011.03.009>.
- Jakobsen, E., Böttger, J., Bellec, P., Geyer, S., Rübbsamen, R., Petrides, M., Margulies, D.S., 2016. Subdivision of Broca's region based on individual-level functional connectivity. *Eur. J. Neurosci.* 43, 561–571. <https://doi.org/10.1111/ejn.13140>.
- Janzen, J., Schlindwein, P., Bense, S., Bauermann, T., Vucurevic, G., Stoeter, P., Dieterich, M., 2008. Neural correlates of hemispheric dominance and ipsilaterality within the vestibular system. *Neuroimage* 42, 1508–1518. <https://doi.org/10.1016/j.neuroimage.2008.06.026>.
- Karnath, H.O., Dieterich, M., 2006. Spatial neglect—a vestibular disorder? *Brain* 129, 293–305 (pii). <https://doi.org/10.1093/brain/awh698>.
- Kaski, D., Quadir, S., Nigmatullina, Y., Malhotra, P.A., Bronstein, A.M., Seemungal, B.M., 2016. Temporoparietal encoding of space and time during vestibular-guided orientation. *Brain* 139, 392–403. <https://doi.org/10.1093/brain/awv370>.
- Kim, D.J., Park, B., Park, H.J., 2013. Functional connectivity-based identification of subdivisions of the basal ganglia and thalamus using multilevel independent component analysis of resting state fMRI. *Hum. Brain Mapp.* 34, 1371–1385. <https://doi.org/10.1002/hbm.21517>.
- Kim, J.-H., Lee, J.-M., Jo, H.J., Kim, S.H., Lee, J.H., Kim, S.T., Seo, S.W., Cox, R.W., Na, D.L., Kim, S.I., Saad, Z.S., 2010. Defining functional SMA and pre-SMA subregions in human MFC using resting state fMRI: functional connectivity-based parcellation method. *Neuroimage* 49, 2375–2386. <https://doi.org/10.1016/j.neuroimage.2009.10.016>.
- Kirsch, V., Boegle, R., Keeser, D., Kierig, E., Ertl-Wagner, B., Brandt, T., Dieterich, M., 2018. Beyond Binary Parcellation of the Vestibular Cortex. *Data in Brief*. Submitted.
- Kirsch, V., Keeser, D., Hergenroeder, T., Ertl, O., Ertl-Wagner, B., Brandt, T., Dieterich, M., 2016. Structural and functional connectivity mapping of the vestibular circuitry from human brainstem to cortex. *Brain Struct. Funct.* 221, 1291–1308. <https://doi.org/10.1007/s00429-014-0971-x>.
- Kirsch, V., Keeser, D., Becker-Bense, S., Karali, T., Ertl-Wagner, B., Brandt, T., Dieterich, M., 2017. Vestibular and visual cortex activity during room tilt illusion. *J. Neurol.* <https://doi.org/10.1007/s00415-017-8457-4>.

V. Kirsch et al.

NeuroImage 178 (2018) 224–237

- Klingner, C.M., Volk, G.F., Flatz, C., Brodoehl, S., Dieterich, M., Witte, O.W., Guntinas-Lichius, O., 2013. Components of vestibular cortical function. *Behav. Brain Res.* 236, 194–199. <https://doi.org/10.1016/j.bbr.2012.08.049>.
- Konen, C.S., Kastner, S., 2008. Representation of eye movements and stimulus motion in topographically organized areas of human posterior parietal cortex. *J. Neurosci.* 28, 8361–8375. <https://doi.org/10.1523/JNEUROSCI.1930-08.2008>.
- Laird, A.R., Fox, P.M., Eickhoff, S.B., Turner, J.A., Ray, K.L., McKay, D.R., Glahn, D.C., Beckmann, C.F., Smith, S.M., Fox, P.T., 2011. Behavioral interpretations of intrinsic connectivity networks. *J. Cognit. Neurosci.* 23, 4022–4037. https://doi.org/10.1162/jocn_a.00077.
- Levy, J., 1969. Possible basis for the evolution of lateral specialization of the human brain. *Nature* 224, 614–615.
- Logothetis, N.K., 2012. Intracortical recordings and fMRI: an attempt to study operational modules and networks simultaneously. *Neuroimage* 62, 962–969. <https://doi.org/10.1016/j.neuroimage.2012.01.033>.
- Logothetis, N.K., 2002. The neural basis of the blood-oxygen-level-dependent functional magnetic resonance imaging signal. *Philos. Trans. R. Soc. Lond. B Biol. Sci.* 357, 1003–1037. <https://doi.org/10.1098/rstb.2002.1114>.
- Lopez, C., Blanke, O., 2011. The thalamocortical vestibular system in animals and humans. *Brain Res. Rev.* 67, 119–146. <https://doi.org/10.1016/j.brainresrev.2010.12.002>.
- Lopez, C., Blanke, O., Mast, F.W., 2012. The human vestibular cortex revealed by coordinate-based activation likelihood estimation meta-analysis. *Neuroscience* 212, 159–179. <https://doi.org/10.1016/j.neuroscience.2012.03.028>.
- Makris, N., Goldstein, J.M., Kennedy, D., Hodge, S.M., Caviness, V.S., Faraone, S.V., Tsuang, M.T., Seidman, L.J., 2006. Decreased volume of left and total anterior insular lobule in schizophrenia. *Schizophr. Res.* 83, 155–171. <https://doi.org/10.1016/j.schres.2005.11.020>.
- Mars, R.B., Sallet, J., Schüffelgen, U., Jbabdi, S., Toni, I., Rushworth, M.F.S., 2012. Connectivity-based subdivisions of the human right “temporoparietal junction area”: evidence for different areas participating in different cortical networks. *Cerebr. Cortex* 22, 1894–1903. <https://doi.org/10.1093/cercor/bhr268>.
- Neubert, F.-X., Mars, R.B., Thomas, A.G., Sallet, J., Rushworth, M.F.S., 2014. Comparison of human ventral frontal cortex areas for cognitive control and language with areas in monkey frontal cortex. *Neuron* 81, 700–713. <https://doi.org/10.1016/j.neuron.2013.11.012>.
- Nigmatullina, Y., Hellyer, P.J., Nachev, P., Sharp, D.J., Seemungal, B.M., 2015. The neuroanatomical correlates of training-related perceptuo-reflex uncoupling in dancers. *Cerebr. Cortex* 25, 554–562. <https://doi.org/10.1093/cercor/bht266>.
- Oldkvist, L.M., Schwarz, D.W., Fredrickson, J.M., Hassler, R., 1974. Projection of the vestibular nerve to the area 3a arm field in the squirrel monkey (*saimiri sciureus*). *Exp. Brain Res.* 21, 97–105.
- Oldfield, R.C., 1971. The assessment and analysis of handedness: the Edinburgh inventory. *Neuropsychologia* 9, 97–113. [https://doi.org/10.1016/0028-3932\(71\)90067-4](https://doi.org/10.1016/0028-3932(71)90067-4).
- Oliveira, F.F., de, Marin, S., de M.C., Bertolucci, P.H.F., 2016. Neurological impressions on the organization of language networks in the human brain. *Brain Inj.* 1–11. <https://doi.org/10.1080/02699052.2016.1199914>.
- Phillips, C.G., Powell, T.P., Wiesendanger, M., 1971. Projection from low-threshold muscle afferents of hand and forearm to area 3a of baboon's cortex. *J. Physiol.* 217, 419–446.
- Preuss, T.M., 2011. The human brain: rewired and running hot. *Ann. N. Y. Acad. Sci.* E182–E191. <https://doi.org/10.1111/j.1749-6632.2011.06001.x>.
- Rancez, E.A., Moya, J., Drawitsch, F., Brichta, A.M., Canals, S., Margrie, T.W., 2015. Widespread vestibular activation of the rodent cortex. *J. Neurosci.* 35, 5926–5934. <https://doi.org/10.1523/JNEUROSCI.1869-14.2015>.
- Rasmussen, T., Milner, B., 1977. The role of early left-brain injury in determining lateralization of cerebral speech functions. *Ann. N. Y. Acad. Sci.* 299, 355–369.
- Ringo, J.L., Doty, R.W., Demeter, S., Simard, P.Y., 1994. Time is of the essence: a conjecture that hemispheric specialization arises from interhemispheric conduction delay. *Cerebr. Cortex* 4, 331–343.
- Salmaso, D., Longoni, A.M., 1985. Problems in the assessment of hand preference. *Cortex* 21, 533–549.
- Särelä, J., Vígario, R., 2001. The problem of overlearning in high-order ICA approaches: analysis and solutions BT - bio-inspired applications of connectionism. In: Mira, J., Prieto, A. (Eds.), *Bio-inspired Applications of Connectionism. IWANN 2001. Lecture Notes in Computer Science*, vol 2085. Springer, Berlin, Heidelberg. Springer Berlin Heidelberg, Berlin, Heidelberg, pp. 818–825. Mira J., Prieto A. https://doi.org/10.1007/3-540-45723-2_99.
- Schneider, E., Villgratner, T., Vockeroth, J., Bartl, K., Kohlbecher, S., Bardins, S., Ulbrich, H., Brandt, T., 2009. EyeSeeCam: an eye movement-driven head camera for the examination of natural visual exploration. *Ann. N. Y. Acad. Sci.* 1164, 461–467. <https://doi.org/10.1111/j.1749-6632.2009.03858.x>.
- Sherwood, C.C., Bauernfeind, A.L., Bianchi, S., Raghanti, M.A., Hof, P.R., 2012. Human Brain Evolution Writ Large and Small, pp. 237–254. <https://doi.org/10.1016/B978-0-444-53860-4.00011-8>.
- Smith, S.M., Fox, P.T., Miller, K.L., Glahn, D.C., Fox, P.M., Mackay, C.E., Filippini, N., Watkins, K.E., Toro, R., Laird, A.R., Beckmann, C.F., 2009. Correspondence of the brain's functional architecture during activation and rest. *Proc. Natl. Acad. Sci. U. S. A.* 106, 13040–13045. <https://doi.org/10.1073/pnas.0905267106>.
- Smith, S.M., Nichols, T.E., Vidaurre, D., Winkler, A.M., Behrens, T.E., Glasser, M.F., Ugurbil, K., Barch, D.M., Van Essen, D.C., Miller, K.L., 2015. A positive-negative mode of population covariation links brain connectivity, demographics and behavior. *Nat. Neurosci.* 18, 1–7. <https://doi.org/10.1038/nn.4125>.
- Suzuki, M., Kitano, H., Ito, R., Kitanishi, T., Yazawa, Y., Ogawa, T., Shiino, A., Kitajima, K., 2001. Cortical and subcortical vestibular response to caloric stimulation detected by functional magnetic resonance imaging. *Cognit. Brain Res.* 12, 441–449.
- Thirion, B., Varoquaux, G., Dohmatob, E., Poline, J.-B., 2014. Which fMRI clustering gives good brain parcellations? *Front. Neurosci.* 8 (167). <https://doi.org/10.3389/fnins.2014.00167>.
- Tolias, A.S., Sultan, F., Augath, M., Oeltermann, A., Tehovnik, E.J., Schiller, P.H., Logothetis, N.K., 2005. Mapping cortical activity elicited with electrical microstimulation using fMRI in the macaque. *Neuron* 48, 901–911. <https://doi.org/10.1016/j.neuron.2005.11.034>.
- van den Heuvel, M.P., Kahn, R.S., Goni, J., Sporns, O., 2012. High-cost, high-capacity backbone for global brain communication. *Proc. Natl. Acad. Sci. Unit. States Am.* 109, 11372–11377. <https://doi.org/10.1073/pnas.1203593109>.
- van den Heuvel, M.P., Sporns, O., 2013. Network hubs in the human brain. *Trends Cognit. Sci.* 17, 683–696. <https://doi.org/10.1016/j.tics.2013.09.012>.
- van den Heuvel, M.P., Sporns, O., 2011. Rich-club organization of the human connectome. *J. Neurosci.* 31, 15775–15786. <https://doi.org/10.1523/JNEUROSCI.3539-11.2011>.
- Van Essen, D.C., Glasser, M.F., 2014. In vivo architectonics: a cortico-centric perspective. *Neuroimage* 93, 157–164. <https://doi.org/10.1016/j.neuroimage.2013.04.095>.
- Wenzel, R., Bartenstein, P., Dieterich, M., Danek, A., Weindl, A., Mimosima, S., Ziegler, S., Schwaiger, M., Brandt, T., 1996. Deactivation of human visual cortex during involuntary ocular oscillations. A PET activation study. *Brain* 119 (Pt 1), 101–110.
- Whitfield-Gabrieli, S., Nieto-Castanon, A., 2012. A functional connectivity toolbox for correlated and anticorrelated brain networks. *Brain Connect.* 2, 125–141. <https://doi.org/10.1089/brain.2012.0073>.
- Yang, Y., Liu, S., Chowdhury, S. a, DeAngelis, G.C., Angelaki, D.E., 2011. Binocular disparity tuning and visual-vestibular congruency of multisensory neurons in macaque parietal cortex. *J. Neurosci.* 31, 17905–17916. <https://doi.org/10.1523/JNEUROSCI.4032-11.2011>.
- Yarkoni, T., Poldrack, R.A., Nichols, T.E., Van Essen, D.C., Wager, T.D., 2011. Large-scale automated synthesis of human functional neuroimaging data. *Br. J. Pharmacol.* 8, 665–670. <https://doi.org/10.1038/nmeth.1635>.
- Zamora-López, G., Zhou, C., Kurths, J., 2010. Cortical hubs form a module for multisensory integration on top of the hierarchy of cortical networks. *Front. Neuroinf.* 4 (1). <https://doi.org/10.3389/fnro.2010.11.001>.
- Zu Eulenburg, P., Caspers, S., Roski, C., Eickhoff, S.B., 2012. Meta-analytical definition and functional connectivity of the human vestibular cortex. *Neuroimage* 60, 162–169. <https://doi.org/10.1016/j.neuroimage.2011.12.032>.

Glossary

- BA: Broadman areal
 C: Common cluster
 CSF: Cerebrospinal fluid
 fCBP: Functional connectivity based parcellation
 IC: Independent component
 ICA: Independent component analysis
 IPL: Inferior parietal lobule
 L: Left
 LH: Left-handed
 L-I: Laterality-index
 MR: Magnetic resonance
 MRI: Magnetic resonance imaging
 MST: Medial superior temporal area
 MSTd: Dorsal medial superior temporal area
 M/STG: Middle and superior temporal gyrus
 MT: Middle temporal area
 OP: Operculum
 OP2: Operculum 2
 P: Parcel
 P-P: Parcel to parcel correlation
 P-RSN: Parcel to resting state network correlation
 PET: Positron emission tomography
 PIVC: Parieto-insular vestibular cortex
 R: Right
 RH: Right-handed
 ROI: Region of interest
 RSN: Resting-state network
 SD: Standard deviation
 STG: Superior temporal gyrus
 SVV: Subjective visual vertical
 TP: Temporo-parietal
 U: Unique voxel
 VOG: Videoculography
 VOR: Vestibular-ocular reflex
 VPS: Visual posterior sylvian area

6. Publikation II - Vestibular paroxysmia entails vestibular nerve function, microstructure and endolymphatic space changes linked to root-entry zone neurovascular compression

Kierig E, Gerb J, Boegle R, Ertl-Wagner B, Dieterich M, Kirsch V. Vestibular paroxysmia entails vestibular nerve function, microstructure and endolymphatic space changes linked to root-entry zone neurovascular compression. *J Neurol*. 2022 Oct 18. doi: 10.1007/s00415-022-11399-y. Epub ahead of print. PMID: 36255522.



Vestibular paroxysmia entails vestibular nerve function, microstructure and endolymphatic space changes linked to root-entry zone neurovascular compression

Emilie Kierig^{1,2} · Johannes Gerb^{1,2} · Rainer Boegle^{1,2,3} · Birgit Ertl-Wagner^{4,5} · Marianne Dieterich^{1,2,3,6} · Valerie Kirsch^{1,2,3}

Received: 24 November 2021 / Revised: 22 September 2022 / Accepted: 23 September 2022
© The Author(s) 2022

Abstract

Combining magnetic resonance imaging (MRI) sequences that permit the determination of vestibular nerve angulation (NA = change of nerve caliber or direction), structural nerve integrity via diffusion tensor imaging (DTI), and exclusion of endolymphatic hydrops (ELH) via delayed gadolinium-enhanced MRI of the inner ear (iMRI) could increase the diagnostic accuracy in patients with vestibular paroxysmia (VP). Thirty-six participants were examined, 18 with VP (52.6 ± 18.1 years) and 18 age-matched with normal vestibulocochlear testing (NP 50.3 ± 16.5 years). This study investigated whether (i) NA, (ii) DTI changes, or (iii) ELH occur in VP, and (iv) to what extent said parameters relate. Methods included vestibulocochlear testing and MRI data analyses for neurovascular compression (NVC) and NA verification, DTI and ELS quantification. As a result, (i) NA increased NVC specificity. (ii) DTI structural integrity was reduced on the side affected by VP ($p < 0.05$). (iii) 61.1% VP showed mild ELH and higher asymmetry indices than NP ($p > 0.05$). (iv) “Disease duration” and “total number of attacks” correlated with the decreased structural integrity of the affected nerve in DTI ($p < 0.001$). NVC distance within the nerve’s root-entry zone correlated with nerve function (Roh = 0.72, $p < 0.001$), nerve integrity loss (Roh = -0.638, $p < 0.001$), and ELS volume (Roh = -0.604, $p < 0.001$) in VP. In conclusion, this study is the first to link eighth cranial nerve function, microstructure, and ELS changes in VP to clinical features and increased vulnerability of NVC in the root-entry zone. Combined MRI with NVC or NA verification, DTI and ELS quantification increased the diagnostic accuracy at group-level but did not suffice to diagnose VP on a single-subject level due to individual variability and lack of diagnostic specificity.

Keywords Vestibular paroxysmia · Endolymphatic hydrops · Endolymphatic space · MRI · Inner ear · Gadolinium-based contrast agent · Intravenous · Vestibular nerve · Root-entry zone · DTI · Diffusion imaging

Abbreviations

3D	Three-dimensional	ANOVA	Analysis of variance
AD	Axial diffusivity	Δ	Side difference
AEP	Auditory evoked potential	DTI	Diffusion tensor imaging
AI	Asymmetry index	dVP	Definite vestibular paroxysmia
AICA	Anterior inferior cerebellar artery	DWI	Diffusion-weighted imaging
		ELH	Endolymphatic hydrops
		ELS	Endolymphatic space
		FA	Fractional anisotropy

Emilie Kierig and Johannes Gerb contributed equally to the study.

✉ Valerie Kirsch
vkirsch@med.lmu.de

¹ Department of Neurology, University Hospital, Ludwig-Maximilians-Universität, Fraunhoferstr. 20, 82152 Munich, Germany

² German Center for Vertigo and Balance Disorders-IFB, University Hospital, Ludwig-Maximilians-Universität, Munich, Germany

³ Graduate School of Systemic Neuroscience (GSN), Ludwig-Maximilians-Universität, Munich, Germany

⁴ Department of Radiology, The Hospital for Sick Children, University of Toronto, Toronto, Canada

⁵ Department of Radiology, University Hospital, Ludwig-Maximilians-Universität, Munich, Germany

⁶ Munich Cluster for Systems Neurology (SyNergy), Munich, Germany

FLAIR	Fluid-attenuated inversion recovery
NP	Participants with normal vestibulocochlear testing
HIT	Head-impulse test
IAC	Internal auditory canal
IE-Vnet	Inner ear Vnet
iMRI	Delayed intravenous gadolinium-enhanced MRI of the inner ear
LH	Left-handed
MASD	Mean of the absolute differences of the first (1st) order
MA2SD	Mean of the absolute differences of the second (2nd) order
MD	Mean diffusivity
MRI	Magnetic resonance imaging
MSSD	Mean of the squared differences of the 1st order
MS2SD	Mean of the squared differences of the 2nd order
NA	Nerve angulation
NVC	Neurovascular compression
PCA	Principal component analysis
PE	Point of entry/exit for afferent/efferent fibers out of/into the brainstem
PICA	Posterior inferior cerebellar artery
PS	Perilymphatic space
PLS	Projection into latent space
PTA	Pure tone audiometry
pVP	Probable vestibular paroxysmia
RD	Radial diffusivity
RH	Right-handed
SCA	Superior cerebellar artery
SPN	Spontaneous nystagmus
SPACE	Sampling perfection with application-optimized contrasts by using different flip angle evolutions
SSP	Statistical summary parameter
SVV	Subjective visual vertical
TFS	Total fluid space
TN	Triggered nystagmus
TiN	Trigeminal neuralgia
VA	Vertebral artery
VM	Vestibular migraine
VN	Vestibular nerve
VOG	Video-oculography
VP	Vestibular paroxysmia

demyelination with succeeding hyperexcitability through neurovascular compression (NVC) in the root-entry and transition zone of the eighth cranial nerve [2–4]. Diagnostic criteria for VP, as defined by the Classification Committee of the Bárány Society, are mostly based on patient history [5]. However, due to symptom variability caused partly by an affection of different audiovestibular parts of the eighth cranial nerve, diagnosis is only considered definitive when responsive to carbamazepine or oxcarbazepine.

Clinical and neurophysiological parameters vary in VP. Patients can exhibit signs of mild to moderate unilateral nerve failure [6, 7], excitation [8, 9], both [10, 11], or no dysfunction [12] in audiovestibular testing during attack-free intervals. Therefore, a combination of neurophysiological and imaging techniques is recommended to determine the affected side and the degree of damage associated with VP [6]. However, magnetic resonance imaging (MRI) findings of vascular compression are not VP-specific or predictive for the affected side because they are also observed in about 30% of healthy asymptomatic subjects [6, 10]. Moreover, 7 Tesla T1 structural MRI detected no abnormalities within the VP vestibular nerve in six patients underlining that VP symptoms are not a sign of nerve hypofunction [13].

The question was whether an MR imaging approach tailored to VP could improve the overall predictive diagnostic value in VP. Therefore, the combination of three sequences permits the determination of vestibular nerve angulation, structural nerve integrity via diffusion tensor imaging (DTI), and non-invasive quantification of the endolymphatic space (ELS) by delayed gadolinium-enhanced MRI of the inner ear (iMRI) were used. Nerve angulation/distortion (NA) was proposed to be a more specific imaging feature than NVC [14]. In addition, DTI revealed significantly lower anisotropy and higher apparent diffusion coefficient in the affected trigeminal root in trigeminal neuralgia than healthy controls [15]. Furthermore, iMRI is developing into a standard clinical tool to investigate a possible endolymphatic hydrops (ELH) as a cause of episodic vertigo, such as in Ménière's disease [16, 17] and vestibular migraine [18, 19]. Against this background, the study investigated the following aspects:

- (i) Can nerve angulation/distortion improve the NVC informative value in VP?
- (ii) Are there measurable structural differences in the affected eighth cranial nerve in VP?
- (iii) Does ELH play a role in VP?
- (iv) To what extent are clinical, diagnostic, and MRI VP parameters related?

Introduction

Vestibular paroxysmia (VP) is a rare cause of short episodic vertigo with or without auditory and vegetative symptoms [1]. The assumed mechanism is ephaptic discharges induced by

Materials and methods

Setting and institutional review board approval

All data were acquired at the Interdisciplinary German Center for Vertigo and Balance Disorders (DSGZ) and the Neurology Department of the Munich University Hospital (LMU) between 2018 and 2020. Institutional Review Board approval was obtained before the initiation of the study (no. 641-15). Furthermore, all participants provided informed oral and written consent in accordance with the Declaration of Helsinki before inclusion in the study.

Study population

Thirty-six consecutive participants, 18 patients with vestibular paroxysmia (VP) and 18 age-matched participants with normal vestibulocochlear testing (NP), underwent MR imaging with sequences that permit determination of vestibular nerve angulation, structural nerve integrity via diffusion tensor imaging (DTI), and delayed intravenous gadolinium-enhanced magnetic resonance imaging (iMRI) for exclusion or verification of ELH. Diagnosis of VP was based on the Classification Committee of the Bárány Society 2016 [5]. Therefore, MRI results were excluded from the diagnostic classification. NP were inpatients of the Neurology Department without symptoms or underlying pathologies of the vestibulocochlear system that underwent MRI with a contrast agent as part of their diagnostic workup and agreed to undergo additional iMRI sequences after 4 h. Ethical considerations did not allow us to include healthy volunteers without a medical indication for an iMRI with a contrast agent (see limitations for more information). NP underwent audiovestibular testing to confirm the soundness of their peripheral inner ear end-organs. The reasons for their admission to the clinic included movement disorders ($n=4$), epilepsy ($n=3$), optic neuritis ($n=2$), polyneuropathy ($n=2$), headache ($n=2$), idiopathic facial nerve palsy ($n=1$), viral meningitis ($n=1$), subdural hematoma ($n=1$), spinal inflammatory lesion ($n=1$), and decompensated esophoria ($n=1$). The laterality quotient for right-handedness was assessed with the ten-item inventory of the Edinburgh test [20]. Inclusion criteria were age between 18 and 85 years (VP, NP) and normal audiovestibular testing to confirm the soundness of their peripheral end-organs and the central vestibular system (NP, see “Measurement of the auditory, semicircular canal and otolith functions”). Exclusion criteria for NP were current cochlear or vestibular disorders, a positive history of vertigo-, balance-, or hearing disorders, as well as any MR-related contraindications [21], poor image quality, or missing MR sequences for NP and VP.

Measurement of the auditory, semicircular canal and otolith functions

Diagnostic workup included a thorough neurological workup (e.g., history-taking, clinical examination), neuro-orthoptic assessment [e.g., Frenzel glasses, fundus photography and adjustments of the subjective visual vertical (SVV)], video-oculography (VOG) during caloric and head impulse testing (HIT), as well as ocular and cervical vestibular evoked myogenic potentials (o/cVEMPs), and pure tone audiometry (PTA).

A tilt of the SVV is a sensitive sign of an acute graviceptive vestibular tone imbalance. SVV was assessed with the subject sitting upright in front of a half-spherical dome with the head fixed on a chin rest [22]. A mean deviation of $>2.5^\circ$ from the true vertical was considered a pathological tilt of SVV [22].

The impairment of the vestibulo-ocular reflex (VOR) in higher frequencies was measured by HIT [23] using high-frame-rate VOG with EyeSeeCam ([24], EyeSeeTech, Munich, Germany). A median gain during head impulses <0.6 (eye velocity in $^\circ/s$ divided by head velocity in $^\circ/s$) was considered a pathological VOR [25]. Furthermore, semicircular canal responsiveness in lower frequencies was performed for both ears with 30° cold and 44° warm water. Vestibular paresis was defined as $>25\%$ asymmetry between the right- and left-sided responses [26] or the sum of the maximal peak velocities of the slow phase caloric-induced nystagmus for stimulation with warm and cold water on each side $<25^\circ/\text{sec}$ [27]. The caloric asymmetry index (AI_C) was calculated based on the slow-phase velocity of the caloric nystagmus: $AI_C[\%] = \frac{(R_{330} + R_{440}) - (L_{330} + L_{440})}{(R_{330} + R_{440}) + (L_{330} + L_{440})} \times 100$.

Vestibular evoked myogenic potentials (VEMPs) are short-latency, mainly otolith-driven vestibular reflexes elicited by air-conducted sound (ACS), bone-conducted vibration, or galvanic vestibular stimulation and recorded from the contralateral inferior oblique eye muscle (ocular or oVEMPs) or the ipsilateral sternocleidomastoid muscle (cervical or cVEMPs). VEMPs were recorded with the Eclipse platform (Interacoustics, Middelfart, Denmark) as described previously [28, 29]. VEMP responses that were discernible from background noise were included in the analysis. Furthermore, only the asymmetry index ($AI_{O/CV}$) of VEMP amplitudes and latencies were analyzed to avoid bias by examiners [30]. Amplitude side difference $\geq 50\%$ was considered pathological.

For cochlear function and acoustic processing, acoustically evoked potentials (AEP) and pure-tone audiometry (PTA) by air conduction at 250 Hz–8.0 kHz were performed. PTA was based on both ears' four-tone average (arithmetic mean) of the thresholds at 0.5, 1, 2, and 3 kHz. Hearing

loss was defined as PTA > 25 dB [31]. In all tests, the contralateral ear was masked by adequate noise. All audiometric equipment is regularly recalibrated (every 6 months) according to the local university equipment standard.

Nomenclature

In the following, “ipsilateral” refers to the clinically leading side (or affected side) and “contralateral” to the opposite side (or non-affected side). The definition of the “clinically leading side (or affected side)” was based on clinical and neurophysiological findings. Side-defining signs were clear patterns of unilateral loss of audiovestibular function [10]. In the case of patients presenting without a leading clinical side, a pseudorandom number generator [“Mersenne Twister” algorithm [31], uniform distribution] was used to generate a random number between 1 (= minimum value) and 9 (= maximum value). Even numbers meant “left side = ipsilateral side,” and uneven numbers indicated “right = ipsilateral side.” “Vertigo” pertains to attacks of spontaneous spinning or non-spinning vertigo with a duration of less than 1 min, stereotyped phenomenology in a particular patient that fits the criteria of VP [5], and is not better accounted for by another diagnosis.

MR imaging approach tailored to VP

MR imaging in this study used combined sequences to investigate the peripheral vestibular system in VP (see Fig. 1). Particular emphasis was put on the presence of neurovascular compression (NVC) and structural DTI tractography quantification along the intracisternal course of the eighth cranial nerve. Another focus included the volumetric quantification of the endolymphatic space (ELS) within the membranous and bony labyrinth of the audiovestibular end-organ.

Data acquisition

Four hours after intravenous injection of a standard dose (0.1 mmol/kg body weight) of gadobutrol (Gadovist®, Bayer, Leverkusen, Germany), MR imaging (MRI) data were acquired in a whole-body 3 Tesla MRI scanner (Magnetom Skyra, Siemens Healthcare, Erlangen, Germany) with a 20-channel head coil.

A high-resolution, strongly T2-weighted, spin-echo 3D-SPACE (three-dimensional sampling perfection with application-optimized contrasts using different flip angle evolutions) sequence delineated the total inner ear fluid space from the surrounding bone. A T2-weighted 3D-FLAIR (three-dimensional fluid-attenuated inversion recovery) sequence was used to differentiate endolymph from perilymph within the total fluid space (TFS). The 3D-FLAIR sequence had the following parameters: TR 6000 ms; TE

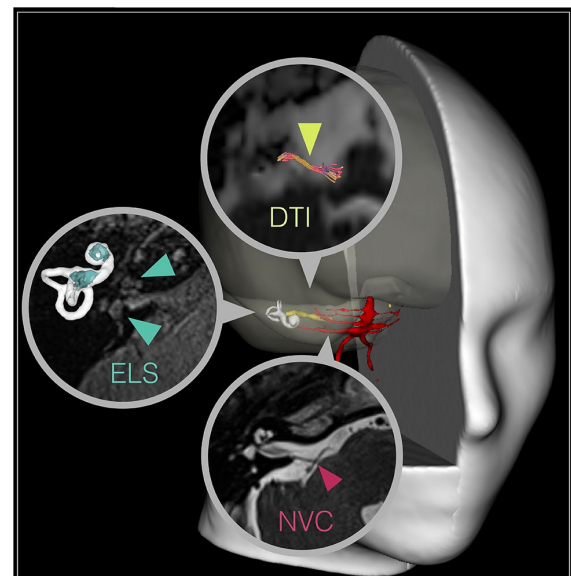


Fig. 1 MR imaging approach tailored to VP. This study investigated the vestibular nerve with a MR imaging approach tailored to vestibular paroxysmia (VP). A 3D rendered T1-image visualizes the spatial relationship between overlaid blood vessels (red), the eighth cranial nerve (8 CN, yellow), and the vestibulocochlear end organ (white shell). These key structures are further shown magnified in a circle within a transversal slice of the cerebellopontine angle in the respective raw data with color-coded arrowheads pointing towards them. Particular emphasis was put on the site of neurovascular compression (NVC, behind red arrowhead in the lower circle), and the DTI tractography quantification of the cisternal segment of the eighth cranial nerve (behind yellow arrowhead in the upper circle) between the point of entry (PE: point of entry for afferent fibers, point of exit for efferent fibers into/out of the brainstem) and the internal auditory canal (IAC). In addition, the study focused on the volumetric quantification of the endolymphatic space (ELS, behind the turquoise arrowheads in the middle circle) within the membranous and bony labyrinth of the inner ear. The upper arrowhead points toward the cochlea, and the lower arrowhead points towards the vestibulum. The corresponding volumetric visualization of these structures (ELS in turquoise) is depicted on the left, next to these structures. Visualization tools were a combination of 3D Slicer (<https://www.slicer.org/>, version 4.11 [36]) and DSI Studio (<http://dsi-studio.labsolver.org/>, version 2021-02-12).

134 ms; TI 2240 ms; FA 180°; FOV 160 × 160 mm²; 36 slices; base resolution 320; averages 1; slice thickness 0.5 mm. The 3D-SPACE sequence had the following parameters: TR 1000 ms; TE 133 ms; FA 100°; FOV 192 × 192 mm²; 56 slices; base resolution 384; averages 4; slice thickness of 0.5. According to a previously reported method [32], ELS was observed on the 3D-FLAIR images as enlarged negative-signal spaces inside the labyrinth.

T1 and DTI structural sequences were used to localize and quantify the vestibular nerve. T1-weighted magnetization-prepared rapid gradient echo (MP-RAGE) sequences had the following parameters: FOV 256 mm; isotropic

spatial resolution of $1.0 \times 1.0 \times 1.0 \text{ mm}^3$; TE 2.07 ms; TR = 1900 ms; number of slices 160. Diffusion tensor imaging (DTI) sequences were measured with the following parameters: 64 directions; $2.0 \times 2.0 \times 2.0 \text{ mm}^3$ isotropic voxels; TE = 95 ms; TR = 9600 ms, bipolar diffusion scheme; b values = 0 and 1000 s/mm^2 .

Data analyses

Neurovascular compression and nerve angulation of the eighth cranial nerve The vestibulocochlear (eighth cranial) nerve was examined using a double oblique reformat of the 3D-SPACE data, with the sagittal plane set in a modified glabellomeatal line and the coronal plane set in line with the vestibulocochlear nerve as suggested by [14]. An experienced head and neck radiologist (BEW) and two neurologists (EK, VK), blinded to the clinical diagnosis, assessed the data. If discrepancies arose, a consensus was reached by discussion. Neurovascular compression (NVC) was defined as a lack of a detectable layer of cerebrospinal fluid between the eighth cranial nerve and any surrounding blood vessel, as proposed by reference [10]. All identified vessels were followed to their origin and classified anatomically. It was classified as an artery (vein) if retracable to a major arterial (venous) vessel. NVC between the point of entry (PE: point of entry for afferent fibers, point of exit for efferent fibers into/out of the brainstem) and the beginning of the internal auditory canal (IAC) were called ‘cisternal,’ NVC within the IAC ‘meatal.’ Nerve angulation (NA) was defined as a change in direction or caliber of the vestibulocochlear nerve at the point of contact, as proposed previously [14]. VP patients had been diagnosed before MRI acquisition based on the clinical diagnostic criteria.

Quantitative structural DTI assessment of the eighth cranial nerve DTI preprocessing included noise correction using MRTRIX3 [33–35]. T1-MPRAGE volume was manually cropped using 3D-SLICER version 4.10.2 [36]. Automated brain extraction was performed with FSL BET [37]. An artificial b0 volume was created using SynB0 [38] and used for geometric and susceptibility artifact correction using FSL Topup [39] and Eddy [40]. After bias field correction using ANTS [41], a reference b0 was extracted from the geometrically corrected diffusion-weighted imaging (DWI). The preprocessed DWI was interpolated to a voxel size of 1 mm^3 using MRTRIX3. A two-step-registration with 12 degrees of freedom was performed using the BRAINSFIT module included in 3D-Slicer, with (j) coregistration of the T1-MPRAGE (moving image) and the reference b0 (fixed image) and (j) coregistration of the high-resolution 3D-SPACE (moving image) and the registered T1-MPRAGE* (fixed image). Finally, a fusion volume of b0 and registered 3D-SPACE was created using MRTRIX3.

DTI tractography and tract-specific analyses were performed using DSI-Studio ([42], <http://dsi-studio.labsolver.org/>). First, an automatic quality control routine checked the b-table to ensure its accuracy [38]. Next, the diffusion tensor was calculated. A deterministic fiber tracking algorithm [43] was used with augmented tracking strategies [44] to improve reproducibility. A spherical seed region was placed at the IAC on the b0-SPACE fusion volume; a spherical ending region was placed at the root-entry zone of the eighth cranial nerve at the pontocerebellar angle. The threshold settings were as follows: anisotropy threshold: 0.5–0.7 Otsu’s threshold, change threshold: 20%, angular threshold: 15–90 degrees, step size: 0.5–1.5 voxels. Tracks shorter than 15 mm or longer than 150 mm were discarded. After 500 tracts were calculated, fiber tracking was automatically terminated. Based on this first approximation, the vestibulocochlear nerve was selected based on the following criteria: (k) anatomically plausible direction, (kk) brainstem entry at the pontocerebellar angle, and (kkk) visual correlation with the course of the nerve in the b0-SPACE fusion volume. After identifying the nerve, the tracts were manually adjusted to remove unwanted fibers inside the brainstem, e.g., the vestibulospinal tract. The generated tracts for the eighth cranial nerves on both sides were stretched to an equal length, allowing analysis of DTI parameters along the course of the tract. A regression kernel size of 2.0 was used.

DTI indices over fractional anisotropy (FA), mean diffusivity (MD), axial diffusivity (AD), and radial diffusivity (RD) were investigated in the following three ways: (I) *Average tensor map approach*: The average DTI indices of the entire vestibular nerve (VN) were used as a surrogate marker for the overall VN integrity. (II) *Localized tensor map approach*: Fiber tracts were assessed in 100 1% subsegments. The entire length (between PE and IAC) of each subject’s VN fiber was 100%. In combination with the affected side, the calculation of the NVC subsegment [%] = $\frac{\text{PEtoNVC}[\text{mm}]}{\text{PEtoIAC}[\text{mm}]} \times 100$ enabled a localized NVC-specific assessment of VN. (III) *Successive differences tensor map approach*: The 100 generated 1% subsegments were transformed into statistical summary parameters (SSP) to reduce the statistical testing and extract relevant features. SSP assessing the “overall” effects of VP vs. NP included the “mean”, “median”, “standard deviation”, and “interquartile range” across all 100 generated 1% steps, i.e., treating each part of the nerve similarly to every other part, as though each segment were a random manifestation of one overall effect. Furthermore, the deviations along the nerve were assessed via statistics of successive differences of first (1st) and second (2nd) order. Successive differences of 1st order are the differences between every two adjacent values of the 100 generated 1% steps divided by

the first value to get a percentage. The 2nd order is the repetition of the process using the generated 99 differences of the 1st order step. The statistical parameters then calculated were *the mean of the squared differences* (MSSD) and *the mean of the absolute differences* (MASD). Note that the squared differences allow a more substantial weighting of large deviations even if few, while the absolute differences do not weigh the larger deviations more strongly than many small ones. Therefore, *the mean squared successive differences* (MSSD: 1st order; MS2SD: 2nd order), and *the mean absolute successive differences* (MASD: 1st order; MA2SD: 2nd order) were calculated as a measure of the relative influence of larger deviations. Due to the use of successive differences, SSPs treat local parts of effectively 2 (1st order) and 4 (2nd order) segments of the nerve as though they are realizations of a random process related to successive local deteriorations of the nerve. Differential entropy [45] was calculated using the 15, 27, and 50 nearest neighbors. SSP allows us to assess the “disorderedness” of the whole nerve and the successive differences. Each of these parameter classes was grouped into collections, such as “central tendencies” (mean and median), “dispersions” (standard deviation and interquartile range), “successive differences 1st order” (MSSD, MASD, and MSSD/MASD), “successive differences 2nd order” (MS2SD, MA2SD, and MS2SD/MA2SD fraction), “raw entropy” and “successive difference entropy”. SSP group differences were assessed using principal component analysis (PCA) using MATLAB’s built-in *pca.m* in the statistics and machine learning toolbox. SSP correlations to chosen clinical parameters (such as “disease duration”, “total number of attacks”, “the average length of the attack”, and “the number of attacks in the last three months”) were tested by projection into latent space (PLS, [46–48]).

Semi-quantitative visual grading and 3D-quantification of the endolymphatic space Semi-quantitative (SQ) visual grading of the endolymphatic space (ELS) was performed independently by an experienced head and neck radiologist (BEW) and two neurologists (JG, VK) who were blinded to the clinical patient data. The ELS’s characterization in the vestibulum and cochlea was based on previously described criteria [49].

3D-quantification of the ELS consisted of three steps: first, segmentation of the total fluid space (TFS) was based on IE-Vnet [50], a recently proposed and pre-trained volumetric deep learning algorithm with V-net architecture that was deployed via the TOMAAT module [51] in a 3D-Slicer toolbox (version 4.11 [36]). Second, ELS and perilymphatic space (PS) were differentiated within the TFS using Volumetric Local Thresholding (VOLT; [52]) with ImageJ Fiji [53], the “Fuzzy and artificial neural networks image

processing toolbox” [54], and the “MorphoLibJ Toolbox” [55]. The resulting 3D volume included classification into two different compartments (ELS and PS), examined at cut-off 6. Third, measurements were performed using the ‘Analyze Regions (3D)’ plugin of the “MorpholibJ Toolbox” [55]. The method is described in more detail in previous publications [52].

ELS symmetry between both inner ears was assessed using two parameters: Absolute ELS side difference, where $\Delta = |ELS_i - ELS_c|$, and ELS_i is the 3D-quantification of the ipsilateral ELS and ELS_c of the contralateral ELS in mm^3 . Normalized ELS side difference, with an asymmetry index, $AI[\%] = \frac{(ELS_v - ELS_c)}{(ELS_i + ELS_c)} \times 100$, where the value is independent of the individual TFS.

Statistics and validation parameters

Analyses were performed using the Statistical Package for Social Sciences software (SPSS, Inc, Chicago, IL, USA) or using self-written scripts in MATLAB, version 7.19.0 (R2019b), including the “Statistics and Machine Learning” toolbox provided with MATLAB (Natick, Massachusetts: The MathWorks Inc). Categorical values are reported as the number of cases that fit the category/number of patients in the examined group [%]; ordinal or scalar values are presented as (mean \pm standard deviation).

NVC and ELS parameter

One-way analysis of variance (ANOVA) for multiple comparisons, which was post-hoc Bonferroni-corrected for multiple testing, was used for scalar (ELS volumetric quantification result, clinical diagnostic raw data) and ordinal (ELH semi-quantitative visual scoring result) values. Group differences were assessed between all VP vs. NP and definite VP vs. NP. Linear agreement between parameter pairs was calculated for each method separately using the two-sided Spearman’s correlation coefficient. Results were reported at a significance level of $p < 0.05$ and $p < 0.001$, corrected for multiple comparisons.

DTI parameter

DTI continuous data types were assessed for differences in “central tendency” (e.g., average or median) and “dispersion” (e.g., variance) between groups (VP vs. NP). The group differences were assessed using the non-parametric Wilcoxon rank-sum test for differences in medians between the groups and via the Brown–Forsythe test for group differences in variance of the two groups via the median absolute deviation. The collections named above (“central tendencies”, “dispersions”, “successive differences 1st

order”, “successive differences 2nd order”, “raw entropy,” and “successive difference entropy”) were aggregated into single variables using principal component analysis (PCA) and choosing only the most significant principal component score as the representation of the collection for group difference assessment. The group differences were assessed by the non-parametric Wilcoxon rank-sum test for differences in “medians” between the groups and via the Brown–Forsythe test for group differences in variance of the two groups via the “median absolute deviation”. The correlation of the “collections” to disease parameters, such as “disease duration”, “number of attacks”, “average duration of attacks”, and “number of attacks in the three months prior to examination”, was assessed via projection to latent space PLS analog to previous work [47, 48, 56]. In addition, rank-correlations were assessed as the input matrix for the singular value decomposition, which contained scores with ranks correlated to disease parameters. To test these correlations, we use permutation testing as suggested in the previous work [48], using 1000 permutations of the disease parameter in question and counting each correlation more significant than the reference (unpermuted) correlation as a failure of the test, setting the *p*-value of the test as the number of failures divided by the total number of permutations, i.e., $p < 0.001$.

Interparametric correlations

Correlations between clinical and diagnostic features, NVC distances [mm], structural DTI quantifications, and ELS volumes were assessed with a PLS approach (analog to “Interparametric correlations”). Results were reported at correlation coefficient > 0.5 for all measures and significant in 1000 permutation tests, i.e., $p < 0.001$.

Results

Clinical syndrome and treatment in VP patients

Eighteen VP patients (6 females; aged 28–84 years, mean age 52.6 ± 18.1 years; 17 right-handed (RH), one left-handed (LH)] and 18 age-matched NP (13 females; aged 25–78 years, mean age 50.3 ± 16.5 years; 18 RH) were included in the study. VP patients could be further divided into ten definite (dVP, three females; aged 29–61 years, mean age 52.5 ± 8.8 years; 10 RH) and eight probable VP patients (pVP, four females; aged 49–77 years, mean age 63.6 ± 8.9 years; 7 RH, 1 LH). A detailed description of the VP groups’ symptomatology with accompanying complaints and signs, duration of attacks and disorder, and therapeutic success are given in Table 1.

Eleven patients were treated with carbamazepine (5 dVP: minimal dose 200 mg/d, maximal dose 600 mg/d; 6pVP:

minimal dose 200 mg/d, maximal dose 800 mg/d), 3 patients were treated with lacosamide (2 dVP, 1 pVP: 100 mg/d) and 2 patients received oxcarbazepine (1 dVP, 1 pVP: 900 mg/day). Two patients received a combination of lacosamide (2 dVP: minimal dose 100 mg/d, maximal dose 300 mg/d) with either carbamazepine (200 mg/d) or oxcarbazepine (900 mg/dl).

Clinical examination and neurophysiological testing

In 8/18 VP patients (44.4%; dVP: 3/10, 30%; pVP: 5/8, 62.5%), the neurophysiological testing pattern was unremarkable. 7/18 VP patients (38.9%; dVP: 5/10, 50%; pVP: 2/8, 25%) showed a clear pattern of unilateral reduction of audiovestibular function. The remaining 3/18 VP patients (16.7%; dVP: 2/10, 20%; pVP: 1/8, 12.5%) revealed complex neurophysiological patterns representing decreased as well as increased eighth cranial nerve function, that is, a combination of nerve lesion (= hypofunction) and nerve irritation (= hyperexcitability) within the same side. Beyond that, no significant group differences or correlations with clinical parameters were found. A detailed description of the clinical and neurophysiological results is given in Table 2.

MR imaging approach tailored to VP

Neurovascular compression (NVC) and nerve angulation (NA) (*aim i*)

In 15/18 VP patients (83.3%; dVP: 8/10, 80%; pVP: 7/8, 87.5%) and 10/18 NP (55.6%), a NVC between the eighth cranial nerve and a blood vessel was detected. The contacts were documented between the nerve and the anterior inferior cerebellar artery (AICA; VP: 10/15, NP: 10/10), the posterior inferior cerebellar artery (PICA; 2/15 VP), the superior cerebellar artery (SCA; 1/15 VP), and the vertebral artery (VA; 1/15 VP). In another patient, the NVC was between a vein and the nerve. The VP mean distance between the PE and the NVC was 6.1 ± 2.8 mm (range 1.5–9.6 mm; dVP 6.2 ± 3.1 mm, range 1.8–9.6 mm; pVP 6.0 ± 2.7 mm, range 1.5–9.5 mm), the mean VP diameter of the compressing vessels was 0.7 ± 0.1 mm (dVP 0.7 ± 0.1 mm, range 0.6–0.8 mm; pVP 0.8 ± 0.1 mm, range 0.6–1.0 mm). The NP mean distance between PE and NVC was 6.6 ± 4.3 mm (range 1.3–14.2 mm), between NVC and IAC 9.7 ± 1.3 mm (range 7.8–11.9 mm), and the mean NP diameter 0.8 ± 0.3 mm (range 0.5–1.3 mm). NA at the contact site was seen in 8/15 NVC (53.3%; dVP: 6/8, 75%; pVP: 2/7, 28.5%). In comparison, NA was only seen in 2/10 NVC (20%) in NP.

In 6/18 VP patients (33.3%; dVP: 1/10, 10%; pVP: 5/8, 62.5%), the neurophysiological testing pattern and course of the nerve were unremarkable. Clinical side and NVC were

Table 1 Clinical syndrome and treatment effects

	VP		
	All	Definite	Probable
Vertigo	55.6% Rotational 33.3% To-and-fro 11.1% Lightheadedness	60% Rotational 30% To-and-fro 10% Lightheadedness	50% Rotational 37.5% To-and-fro 12.5% Lightheadedness
Spontaneous onset	16/18 (88.9%)	8/10 (80%)	8/8 (100%)
Provocation of syndrome	44% No provoking factors 11% Ipsilateral head rotation 33% Bilateral head rotation 5% Head inclination 33% Head reclination	50% No provoking factors 20% Ipsilateral head rotation 20% Bilateral head rotation 10% Head inclination -	37.5% No provoking factors - 50% Bilateral head rotation - 12.5% Head reclination
Frequency of attacks	55.6% Several times/day 27.8% 2–3 times/week 11.1% 2–3 times/month 5.6% once/month	60% Several times/day 30% 2–3 times/week 10% 2–3 times/month -	50% Several times/day 25% 2–3 times/week 12.5% 2–3 times/month 12.5% once/month
Attack duration [in seconds]	21.7 ± 42.6 (6–180)	10.5 ± 1.7 (3–60)	35.8 ± 60.0 (3–180)
Total number of attacks	437.5 ± 458.5	549.1 ± 578.9	312.0 ± 251.1
Number of attacks in the last 3 months	60.1 ± 47.1	60.0 ± 39.6	60.3 ± 58.0
Time since the first attack [in yrs]	3.4 ± 3.7	3.1 ± 2.9	3.8 ± 4.6
Time since the last attack [in days]	32.8 ± 57.2 (1–210)	40.1 ± 63.0 (1–210)	23.8 ± 51.6 (1–150)
Accompanying symptoms	14/18 (77.8%)	9/10 (90%)	5/8 (62.5%)
Nausea and/or vomiting	4/18 (22.2%)	2/10 (20%)	2/8 (25%)
Perspiration	1/18 (5.6%)	0/10 (0%)	1/8 (12.5%)
Oscillopsia	14/18 (77.8%)	8/10 (80%)	6/8 (75%)
Disturbances of gait and stance	7/18 (38.9%)	5/10 (50%)	2/8 (25%)
Headache	3/18 (16.7%)	1/10 (10%)	2/8 (25%)
History of migraine	2/18 (11.1%)	1/10 (10%)	1/8 (12.5%)
Hypacusis	3/18 (16.7%)	1/10 (10%)	2/8 (25%)
Tinnitus	4/18 (22.2%)	2/10 (20%)	2/8 (25%)
Feeling of pressure within ear	1/18 (5.6%)	1/10 (10%)	0/8 (0%)
Under therapy with an anticonvulsant ^a	17/18 (94.4%)	10/10 (100%)	7/8 (87.5%)
Improvement under therapy	10/18 (83.3%)	10/10 (100%)	25% No improvement 75% Unknown

^aCarbamazepine (200–600 mg/d), oxcarbazepine (900 mg/d), or lacosamide (100–300 mg/d)

found to correspond in 3/18 VP (16.7%, dVP 3/10, 30%), contradictory in 3/18 VP (16.7%; dVP 2/10, 20%, pVP 1/8, 12.5%), or inconclusive in 6/18 VP (33.3%; dVP 4/10, 40%, pVP 2/8, 25%). A detailed description of the NVC results can be seen in Table 3.

DTI tractography of the vestibular nerve (*aim ii, aim iv*)

Average (I) and localized (II) tensor map approaches showed no significant differences or correlations. However, within the successive difference map approach (III), the most significant group differences (VP vs. NP) were found for the 1st order successive difference aggregated data collections (1st principal component). This means that in the overall effect along the whole nerve (between PE and IAC), VP showed a higher difference between the ipsilateral and contralateral nerve than NP, where both sides were similar. This supports

the theory that there is a measurable structural difference in the affected nerve compared to the non-affected nerve in VP. An overview can be seen in Table 4. Here, VP and NP differed significantly in their DTI parameter median difference (Δ in FA, RD, AD, MD) between the ipsilateral and contralateral side of the 1st order successive difference data (MSSD, $p < 0.05$, corrected for multiple testing). The aggregated data for the ipsilateral and the difference between the ipsilateral vs. contralateral side and the average (mean) are shown in Fig. 2A.

PLS correlations between the disease parameters “disease duration” and “total number of attacks” and the 1st order of successive differences were significant at $p < 0.001$ (no failures in 1000 permutation tests) with an r-squared of 0.596. The scatter plot of the ranked “disease duration” data and ranks of the 1st order successive difference PLS scores with an overlaid trendline can be viewed in Fig. 2B.

Table 2 Clinical and neurophysiological testing

	VP		NP	
	All <i>n</i> = 18	Definite <i>n</i> = 10	Probable <i>n</i> = 8	All <i>n</i> = 18
Age [in years]	52.6 ± 18.1	52.5 ± 8.8	63.6 ± 8.9	50.3 ± 16.5
Age range	28–84	29–61	49–77	25–78
Gender	6 females	3 females	4 females	13 females
Handedness	17 RH, 1 LH	10 RH	7 RH, 1LH	18 RH
Clinical pattern	44.4% Unremarkable 38.9% Lesion 16.7% Lesion & Irrigation	30% Unremarkable 50% Lesion 20% Lesion & Irrigation	62.5% Unremarkable 25% Lesion 12.5% Lesion & Irrigation	100% Unremarkable – –
TN	1/18 (5.6%)	1/10 (10%)	0/8 (0%)	0/18 (0%)
SPN	1/18 (5.6%)	1/10 (10%)	0/8 (0%)	0/18 (0%)
Nystagmus after hyperventilation	5/14 (35.7%)	3/8 (37.5%)	2/6 (33.3%)	0/18 (0%)
Ocular torsion	0/18 (0%)	0/10 (0%)	0/8 (0%)	0/18 (0%)
SVV deviation	3/18 (16.7%)	2/10 (20%)	1/8 (12.5%)	0/18 (0%)
HIT pathological	6/18 (33.3%)	5/10 (50%)	1/8 (12.5%)	0/13 (0%)
HIT AI [%]	7.2 ± 6.1 (0.5–24.4)	9.0 ± 7.5 (0.5–24.4)	5.0 ± 2.7 (1.1–10.8)	5.2 ± 5.3 (0–17.4)
Calorics pathological	4/18 (22.2%)	4/10 (40%)	0/8 (0%)	0/13 (0%)
Calorics AI [%]	23.2 ± 25.3 (4.0–88.7)	26.1 ± 23.2 (4.8–80.4)	19.7 ± 28.9 (4.0–88.7)	13.4 ± 10.3 (2.0–36.2)
cVEMP pathological	3/11 (27.3%)	3/6 (50%)	0/5 (0%)	0/7 (0%)
cVEMP amplitude AI [%]	19.4 ± 14.6 (3.0–52.0)	21.8 ± 18.6 (3.0–52.0)	17.0 ± 11.0 (4.0–31.0)	14.3 ± 13.9 (0.2–37.3)
oVEMP pathological	3/11 (27.3%)	3/6 (50%)	0/5 (0%)	0/7 (0%)
oVEMP amplitude AI [%]	17.0 ± 10.9 (2.0–36.0)	13.2 ± 7.9 (5.0–25.0)	20.8 ± 13.1 (2.0–36.0)	8.3 ± 7.6 (2.1–21.3)
PTA pathological	5/16 (31.3%)	3/9 (33.3%)	2/7 (28.6%)	2/3 (60%)
PTA presbycusis-typical	3/16 (18.8%)	0/9 (0%)	3/7 (42.9%)	2/2 (100%)
AEP	2/5 (40%)	1/2 (50%)	1/3 (33.3%)	0/0 (0%)

Abbreviations: *AEP* auditory evoked potential, *AI* asymmetry index, *cVEMP* cervical VEMP, *HIT* head-impulse test, *LH* left-handed, *oVEMP* ocular VEMP, *PTA* pure tone audiometry, *RH* right-handed, *SPN* spontaneous nystagmus, *SVV* subjective visual vertical, *TN* triggered nystagmus, *VEMP* vestibular evoked myogenic potential

Endolymphatic space (ELS) characterization (aim iii)

Following a 3-point ordinal scale [57], semi-quantitative ELS (sqELS) classification showed no evidence of endolymphatic hydrops (ELH) in either VP or NP. However, in a 4-point ordinal scale [49], a mild ELH (grade 1) was discernible in 11/18 patients (VP 61.1%, dVP 5/10, 50%; pVP 6/8, 75%). This means that the extent of ELH was low. ELH was most pronounced on the ipsilateral side and in definite VP patients (VP: $sqELS_{ipsi}^{VP}$: grade 0.4 ± 0.6 , range 0–1.5; dVP: $sqELS_{ipsi}^{dVP}$: grade 0.5 ± 0.6 , range 0–1.5; pVP: $sqELS_{ipsi}^{pVP}$: grade 0.4 ± 0.6 , range 0–1.5). This pattern was mirrored in the volumetric ELS (vELS) quantification (VP: $vELS_{ipsi}^{VP}$: $9.6 \pm 4.2 \text{ mm}^3$, range 4.7–17.9 mm^3 ; dVP: $vELS_{ipsi}^{dVP}$: $10.2 \pm 4.6 \text{ mm}^3$, range 5.2–17.9 mm^3 ; pVP: $vELS_{ipsi}^{pVP}$: $8.7 \pm 3.7 \text{ mm}^3$, range 4.7–15.4 mm^3). In

comparison, 5/18 NP (27.8%) showed a mild ELH with an altogether lower mean semiquantitative and volumetric ELS quantification ($sqELS_{mean}^{NP}$: grade 0.2 ± 0.4 , range 0–1; $vELS_{mean}^{NP}$: $8.9 \pm 2.5 \text{ mm}^3$, range 5.2–13.9 mm^3). VP and NP differed significantly regarding the extent of the asymmetry index of the inner ear and vestibulum volume ($p < 0.05$, ANOVA, corrected for multiple testing). Definite VP and NP, on the other hand, differed significantly regarding the extent of the asymmetry index of the vestibulum volume and difference in volume between ipsi- and contralateral side ($p < 0.05$, ANOVA, corrected for multiple testing). No correlations were found between electrophysiological data or degree of ELH and disease duration or number of attacks. A detailed description of the ELS results can be seen in Table 5.

Clinical side and ELS quantification lateralization were inconclusive in 13/18 VP (72.2%; dVP 8/10, 80%; pVP 5/8, 62.5%), and found to correspond in 3/18 VP (16.7%, dVP 1/10, 10%; pVP 2/8, 25%). In 2/18 VP patients (11.1%; dVP

Table 3 Neurovascular compression (NVC) and nerve angulation (NA) results

	VP		NP	
	All	Definite	Probable	All
NVC incidence	15/18 (83.3%)	8/10 (80%)	7/8 (87.5%)	10/18 (55.6%)
NVC location				
Cisternal	16/20 (75%)	7/10 (70%)	9/10 (90%)	10/16 (62.5%)
Meatal	4/20 (25%)	3/10 (30%)	1/10 (10%)	6/16 (37.5%)
NVC side				
Unilateral	10/18 (55.6%)	6/10 (60%)	4/8 (50%)	2/10 (20%)
Bilateral	5/18 (27.8%)	2/10 (20%)	3/8 (37.5%)	7/10 (70%)
To clinical side				
Norm	6/18 (33.3%)	1/10 (10%)	5/8 (62.5%)	18/18 (100%)
Corresponding	3/18 (16.7%)	3/10 (30%)	–	–
Contradictory	3/18 (16.7%)	2/10 (20%)	1/8 (12.5%)	–
Inconclusive	6/18 (33.3%)	4/10 (40%)	2/8 (25%)	–
Vessel				
AICA	10/15 (66.7%)	5/8 (62.5%)	5/7 (71.4%)	10/10 (100%)
PICA	2/15 (13.3%)	2/8 (25%)	–	–
SCA	1/15 (6.7%)	1/8 (12.5%)	–	–
VA	1/15 (6.7%)	–	1/7 (14.3%)	–
Venous	1/15 (6.7%)	–	1/7 (14.3%)	–
NA	8/15 (53.3%)	6/8 (60%)	2/7 (28.6%)	2/10 (20%)
PE to NVC [mm]	6.1 ± 2.8 (1.5–9.6)	6.2 ± 3.1 (1.8–9.6)	6.0 ± 2.7 (1.5–9.5)	6.6 ± 4.3 (1.3–14.2)
PE to IAC [mm]	10.0 ± 1.5 (7.5–13.1)	9.9 ± 2.0 (7.5–13.1)	10.1 ± 1.0 (8.8–11.3)	9.7 ± 1.3 (7.8–11.9)
Diameter [mm]	0.7 ± 0.1 (0.6–1.0)	0.7 ± 0.1 (0.6–0.8)	0.8 ± 0.1 (0.6–1.0)	0.8 ± 0.3 (0.5–1.3)

Abbreviations: *AICA* anterior inferior cerebellar artery, *IAC* internal auditory canal, *NA* nerve angulation/distortion, *NVC* neurovascular compression, *PE* point of entry/exit for afferent/efferent fibers out of/into the brainstem, *PICA* posterior inferior cerebellar artery, *SCA* superior cerebellar artery, *VA* vertebral artery

1/10, 10%; pVP 1/8, 12.5%), the neurophysiological testing pattern and ELS were unremarkable. NVC side and ELS quantification lateralization were inconclusive in 12/18 VP (66.6%; dVP 7/10, 70%, pVP 5/8, 62.5%), contradictory in 3/18 VP (16.7%; dVP 2/10, 20%; pVP 1/8, 12.5%), found to correspond in 2/18 VP (11.1%; pVP 2/8, 25%), or normal in 1/18 (5.6%; dVP 1/10, 10%).

Interparametric correlations (*aim iv*)

The distance between PE and NVC (PE-to-NVC [mm]) correlated with audiovestibular function, i.e., neurophysiological testing (Roh 0.72, $p < 0.001$), structural nerve integrity, i.e., DTI SSPs (Roh – 6.638, $p < 0.001$), and inner ear ELS (Roh – 6.604, $p < 0.001$). Scatter plots with trendlines are shown in Fig. 3.

Discussion

The current study focused on a detailed characterization of structures affecting the cisternal part of the eighth cranial nerve to increase the diagnostic value of MRI in

patients with vestibular paroxysmia (VP) using an MR imaging approach tailored to VP. The high-resolution MRI sequences were used to determine neurovascular compression (NVC) and nerve angulation/distortion (NA), structural nerve integrity via diffusion tensor imaging (DTI), and in-vivo non-invasive verification of endolymphatic hydrops (ELH). The findings were the following: 1. Previously established evidence on the typical clinical and heterogeneous diagnostic picture could be confirmed. 2. Nerve angulation (NA) increases NVC diagnostic specificity in VP (*aim i*); 3. DTI showed structural differences in the affected vestibular nerve in VP at group-level ($p < 0.05$), (*aim ii*); 4. Endolymphatic space (ELS) asymmetry index was mildly but significantly increased at group-level ($p < 0.05$), (*aim iii*); 5. “Disease duration” and “total number of attacks” correlated positively with DTI, i.e., with structural nerve integrity (Roh = 0.594, $p < 0.001$), (*aim iv*); 6. Distance between PE (point of entry/exit for afferent/efferent fibers out of/into the brainstem) and NVC (“PE-to-NVC”) correlated positively with audiovestibular function (Roh = – 0.72, $p < 0.001$) and negatively with structural nerve integrity (Roh = – 0.638, $p < 0.001$), or volume of the inner ear ELS (Roh = – 0.604, $p < 0.001$),

Table 4 Structural quantification of the eighth cranial nerve

DTI parameters	VP		NP	
	All	Definite	Probable	All
Fractional anisotropy (FA)				
Ipsilateral	0.1592 ± 0.0385	0.1504 ± 0.0167	0.1701 ± 0.0548	
Mean	0.1604 ± 0.0230	0.1565 ± 0.009	0.1652 ± 0.0336	0.1528 ± 0.0299
Δ	-0.0024 ± 0.0392	-0.0121 ± 0.0242	0.0098 ± 0.0518	0.0018 ± 0.0260
FA MSSD				
Ipsilateral	1.908e-3 ± 2.862e-3	2.473e-3 ± 3.757e-3	1.212e-3 ± 0.847e-3	
Mean	2.674e-3 ± 3.572e-3	2.735e-3 ± 3.37e-3	2.598e-3 ± 4.046e-3	0.855e-3 ± 0.454e-3
Δ	-1.532e-3 ± 6.679e-3*	-0.52e-3 ± 6.893e-3	-2.793e-3 ± 6.632e-3	0.656e-3 ± 0.931e-3*
Radial diffusivity (RD)				
Ipsilateral	2.3997 ± 0.4198	2.4275 ± 0.3895	2.3649 ± 0.4800	
Mean	2.4064 ± 0.3451	2.4486 ± 0.3103	2.3536 ± 0.3996	2.2799 ± 0.2675
Δ	-0.0134 ± 0.3857	-0.0422 ± 0.3677	0.0226 ± 0.4298	0.0952 ± 0.2742
RD MSSD				
Ipsilateral	9.691e-4 ± 1.397e-3	4.734e-4 ± 5.624e-4	1.589e-3 ± 1.882e-3	
Mean	2.541e-3 ± 6.488e-3	3.991e-4 ± 3.512e-4	5.219e-3 ± 9.345e-3	8.471e-4 ± 1.930e-3
Δ	-3.145e-3 ± 1.104e-2*	1.486e-4 ± 5.045e-4	-7.261e-3 ± 1.615e-2	3.975e-4 ± 3.244e-3*
Axial diffusivity (AD)				
Ipsilateral	3.022 ± 0.4824	3.045 ± 0.4975	2.993 ± 0.4953	
Mean	3.0475 ± 0.3979	3.099 ± 0.3898	2.983 ± 0.4250	2.869 ± 0.3001
Δ	-0.0509 ± 0.4389	-0.108 ± 0.4166	0.020 ± 0.4840	0.124 ± 0.3851
AD MSSD				
Ipsilateral	8.618e-4 ± 1.301e-3	4.294e-4 ± 4.750e-4	1.402e-3 ± 1.793e-3	
Mean	2.606e-3 ± 6.760e-3	4.142e-4 ± 3.672e-4	5.346e-3 ± 9.765e-3	8.412e-4 ± 1.902e-3
Δ	-3.488e-3 ± 1.154e-2*	3.048e-5 ± 5.120e-4	-7.886e-3 ± 1.683e-2	3.664e-4 ± 3.293e-3*
Mean diffusivity (MD)				
Ipsilateral	2.607 ± 0.437	2.633 ± 0.424	2.574 ± 0.481	
Mean	2.620 ± 0.362	2.666 ± 0.336	2.563 ± 0.407	2.476 ± 0.273
Δ	-0.026 ± 0.399	-0.064 ± 0.381	0.022 ± 0.441	0.105 ± 0.309
MD MSSD				
Ipsilateral	9.191e-4 ± 1.359e-3	4.493e-4 ± 5.279e-4	1.506e-3 ± 1.848e-3	
Mean	2.553e-3 ± 6.586e-3	3.950e-4 ± 3.447e-4	5.251e-3 ± 9.497e-3	8.379e-4 ± 1.920e-3
Δ	-3.268e-3 ± 1.121e-2*	1.085e-4 ± 4.937e-4	-7.489e-3 ± 1.639e-2	0.385e-3 ± 3.263e-3*
Successive differences SSP (1st PCA)				
Ipsilateral	0.8098 ± 1.3694	0.3259 ± 0.7166	1.4147 ± 1.7724	0.2681 ± 1.1389
Mean	0.5392 ± 0.7161	0.3397 ± 0.5816	0.7887 ± 0.8261	0.2117 ± 0.8312
Δ	0.8684 ± 1.2049*	0.4044 ± 0.5756	1.4485 ± 1.5517	0.2214 ± 1.0932*

*Wilcoxon rank sum test in their medians for VP (all) vs. NP, where $p < 0.05$, or ** if $p < 0.001$

Abbreviations: Δ = difference between ipsilateral and contralateral side, AD axial diffusivity, FA fractional anisotropy, MD mean diffusivity, MSSD Mean of the squared differences of the first (1st) order, PCA principal component analysis, RD radial diffusivity, SSP statistical summary parameter

(aim iv). At the group level, there were significant differences between VP participants and NP. In sum, the predictive value of MRI is increased. However, on a single-subject level, the methodology's specificity is insufficient to diagnose VP.

In the following, we discuss these findings compared to previously published VP studies and the significance of dedicated VP MRI to quantify ELS and vestibular nerve structural integrity, its clinical implications, and recommendations for future studies and methodical limitations.

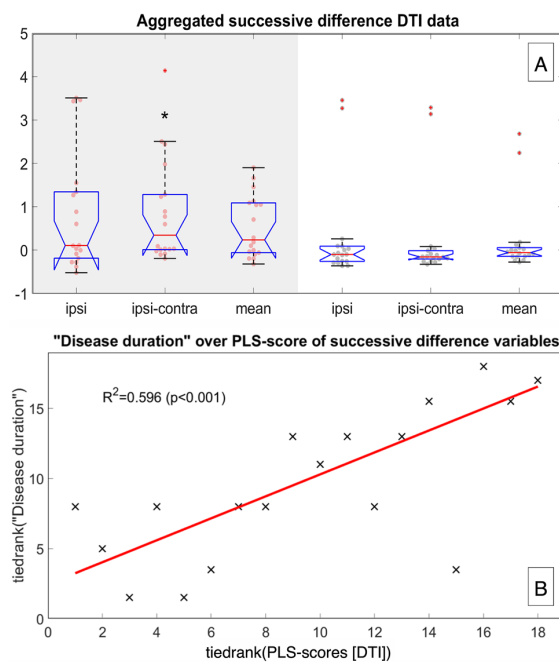


Fig. 2 DTI tractography results. Compiled results of DTI group differences (A) and correlations (B): The upper graphic (A) shows the aggregated group difference data for the ipsilateral, the difference between ipsilateral and contralateral sides, and the average (mean) of both sides as boxplots with overlaid data points. The VP data is shown in red with a gray background, and the NP data is shown in black with a white background. Significant differences in the median between the groups are marked by a black star “*”, with a significance level $p<0.05$. The lower graphic (B) depicts PLS rank-correlations between disease parameter “disease duration” and the 1st order of successive differences. The scatter plot of the ranked “disease duration” data and ranks of the 1st order successive difference PLS scores are shown as black crosses, with an overlaid trendline in red. The explained variance r-squared was 0.596 with significance $p<0.001$ (no failures in 1000 permutation tests)

Confirmation of previously established VP evidence (aim i)

VP pathophysiology seems to be best explained by a “dual”, i.e., combined peripheral and central pathology [10]. While NVC is a necessary factor for the development of clinical symptoms [58–60], a central cranial nerve nuclei pathology with increased excitability or even a dysfunction at the level of thalamic-cortical projections, as well as on a cortical level with a reduced inhibitory projection to the cranial nerve nuclei develop [61, 62]. Furthermore, additional unknown factors are thought to play a role [63].

This study’s clinical and diagnostic results mirror the clinical picture of this vestibular NVC syndrome. The current VP cohort was characterized by the typical monomorphic clinical syndrome [2–4] and accompanied

by a heterogeneous [12, 64] diagnostic neurophysiological picture (25–50% unremarkable, 33–45% pattern of reduction of audiovestibular function [6, 12], 17–30% complex neurophysiological pattern representing decreased as well as increased nerve function [8, 9, 11] as a combination of nerve lesion and nerve irrigation within the same side [10]). NVC was found in 83.3% of the current study and occurred along the whole intracranial part of the nerve, particularly within the root entry and transition zone. Meatal NVC is rarer but did also occur. Most frequently, the compressing vessel could be attributed to the AICA (75%), but other vessels, such as the vertebral artery (VA, 10%), PICA (5%), or a vein (10%), are possible [10]. This was also true in the current study (AICA 66.7%, PICA 13.3%, VA 6.7%, SCA 6.7%, vein 6.7%). However, vascular loops as normal variants without clinical symptoms were found in about 25–30% (and in our control group about 50%) [65]. As an additional feature, NA increased NVC’s specificity in VP [14]. Fittingly, they were 3:1 more frequent in VP than in NP and 2:1 more frequent in definite VP than in probable VP of our study.

Structural abnormalities of the vestibular nerve revealed by DTI (aim ii)

NVC syndromes entail a local peripheral nerve compression. It, therefore, seems reasonable to assume a DTI structural correlation in the affected nerve of VP patients. The current study found measurable DTI structural differences in the median difference between the affected and non-affected side of the first order successive difference data of the eighth cranial nerve in VP at group level ($p<0.05$; Fig. 2A) that correlated with “disease duration” and “total number of attacks” ($p<0.001$; Fig. 2B). Nevertheless, the average and localized tensor map approaches were not successful. Different factors could play a role here. One reason may be the low sensitivity of the method. In the future, this could be resolved by choosing high spatial resolution nerve-specific DTI over whole-brain DTI [66], specialized vestibular nerve DWI acquisition strategies for each subsegment [67], and optimized protocols concerning resolution, phase encoding [68], or the number of b-shells [69]. Another reason may be that although local compression of the peripheral nerve by the peripheral NVC is necessary for developing the clinical symptoms, the microstructural lesion does not remain local or is less pronounced than expected. A 7 Tesla T1-sequence with and without contrast agent in 6 VP patients showed no structural abnormalities [13]. Beyond that, to the best of our knowledge, nothing has been published on structural nerve abnormalities in VP.

In contrast, many studies exist on MR structural nerve abnormalities in the trigeminal NVC syndrome, trigeminal neuralgia (TiN), a disease with similar underlying pathophysiology [70]. The results were inhomogeneous, too.

Table 5 Semi- and 3D-quantification of the endolymphatic space

	VP		NP	
	All	Definite	Probable	All
To clinical side				
Norm	2/18 (11.1%)	1/10 (10%)	1/8 (12.5%)	18/18 (100%)
Corresponding	3/18 (16.7%)	1/10 (10%)	2/8 (25%)	–
Inconclusive	13/18 (72.2%)	8/10 (80%)	5/8 (62.5%)	–
To NVC side				
Norm	1/18 (5.6%)	1/10 (10%)	–	16/18 (88.8%)
Corresponding	2/18 (11.1%)	–	2/8 (25%)	1/18 (11.1%)
Contradictory	3/18 (16.7%)	2/10 (20%)	1/8 (12.5%)	1/18 (11.1%)
Inconclusive	12/18 (66.6%)	7/10 (70%)	5/8 (62.5%)	–
Inner ear				
ELH	11/18 (61.1%)	5/10 (50%)	6/8 (75%)	5/18 (27.8%)
Side of ELH				
Unilateral	7/18 (38.9%)	3/10 (30%)	4/8 (50%)	3/18 (16.7%)
Bilateral	4/18 (22.2%)	2/10 (20%)	2/8 (25%)	2/18 (11.1%)
sqELS [grade]				
Ipsilateral	0.4 ± 0.6 (0–1.5)	0.5 ± 0.6 (0–1.5)	0.4 ± 0.4 (0–1)	0.2 ± 0.4 (0–1)
Contralateral	0.3 ± 0.4 (0–1)	0.3 ± 0.4 (0–1)	0.3 ± 0.4 (0–1)	0.2 ± 0.3 (0–1)
AI [%]	11.1 ± 79.8 (–1–100)	16.7 ± 75.3 (–100–100)	5.6 ± 90.5 (–100–100)	0 ± 81.7 (–100–100)
vELS [mm³]				
Ipsilateral	9.6 ± 4.2 (4.7–17.9)	10.2 ± 4.6 (5.2–17.9)	8.7 ± 3.7 (4.7–15.4)	8.9 ± 2.5 (5.2–13.9)
Contralateral	7.9 ± 2.9 (4.7–13.0)	8.5 ± 3.4 (4.2–13.0)	7.1 ± 2.2 (4.6–10.6)	
Δ	1.7 ± 2.2 (–2.4–6.1)	1.7 ± 2.2 (–0.6–6.1)	1.7 ± 2.4 (–2.4–4.8)	0.1 ± 1.9 (–2.6–3.9)
AI [%]	8.6 ± 11.3 (–20.4–25.9)†	8.3 ± 9.1 (–4.3–20.8)	8.8 ± 14.3 (–20.4–25.9)	0.1 ± 10.8 (–20.3–16.4)†
TFS [mm ³]	275.8 ± 26.3 (232.1–321.7)	277.5 ± 24.3 (247.6–311.3)	273.8 ± 30.3 (232.1–321.7)	261.9 ± 34.3 (193.4–309.3)
Cochlea				
ELH	6/18 (33.3%)	3/10 (30%)	3/8 (37.5%)	2/18 (11.1%)
Side of ELH				
Unilateral	4/18 (22.2%)	2/10 (20%)	2/8 (25%)	1/18 (5.6%)
Bilateral	2/18 (11.1%)	1/20 (10%)	1/8 (12.5%)	1/18 (5.6%)
ELS [grade]				
Ipsilateral	0.4 ± 0.6 (0–2)	0.5 ± 0.7 (0–2)	0.4 ± 0.5 (0–1)	0.2 ± 0.4 (0–1)
Contralateral	0.2 ± 0.4 (0–1)	0.1 ± 0.3 (0–1)	0.3 ± 0.5 (0–1)	0.1 ± 0.3 (0–1)
AI [%]	50 ± 75.6 (–100–100)	75 ± 50 (0–100)	25 ± 95.7 (–100–100)	25 ± 95.7 (–100–100)
ELS [mm³]				
Ipsilateral	2.9 ± 1.5 (1.1–6.5)	3.1 ± 1.8 (1.1–6.5)	2.7 ± 1.2 (1.3–4.4)	2.5 ± 1.2 (0.5–5.2)
Contralateral	2.6 ± 1.3 (1.0–5.6)	2.8 ± 1.3 (1.2–3.4)	2.4 ± 1.2 (1.0–3.9)	
Δ	0.3 ± 1.2 (–1.6–3.2)	0.3 ± 1.4 (–1.5–3.2)	0.4 ± 2.0 (–2.3–4.5)	0.1 ± 1.4 (–2.7–2.7)
AI [%]	4.9 ± 21.9 (–40.8–36.7)	2.2 ± 26.6 (–40.8–36.4)	8.2 ± 15.5 (–13.2–36.7)	5.8 ± 32.7 (–71.4–81.8)
TFS [mm ³]	90.8 ± 9.3 (73.1–104.68)	90.3 ± 9.0 (78.8–104.7)	91.4 ± 10.3 (73.1–104.7)	87.3 ± 15.0 (51.1–120.5)
Vestibulum				
ELH	9/18 (50%)	4/10 (40%)	5/8 (62.5%)	5/18 (27.8%)
Side of ELH				
Unilateral	6/18 (33.3%)	2/10 (20%)	4/8 (50%)	3/18 (16.7%)
Bilateral	3/18 (16.7%)	2/20 (20%)	1/8 (12.5%)	2/18 (11.1%)
ELS [grade]				
Ipsilateral	0.4 ± 0.5 (0–1)	0.4 ± 0.5 (0–1)	0.4 ± 0.5 (0–1)	0.2 ± 0.4 (0–1)
Contralateral	0.4 ± 0.5 (0–1)	0.4 ± 0.5 (0–1)	0.4 ± 0.5 (0–1)	0.2 ± 0.4 (0–1)
AI [%]	0 ± 89.4 (–100–100)	0 ± 89.4 (–100–100)	0 ± 100 (–100–100)	0 ± 89.4 (–100–100)

Table 5 (continued)

	VP		NP	
	All	Definite	Probable	All
ELS [mm ³]				
Ipsilateral	6.7 ± 3.1 (1.6–12.0)	7.1 ± 3.3 (2.9–12.0)	6.1 ± 3.0 (1.6–11.5)	6.6 ± 2.2 (2.9–11.9)
Contralateral	5.3 ± 2.0 (3.0–9.2)	5.7 ± 2.3 (3.0–9.2)	4.8 ± 1.3 (3.5–7.0)	
Δ	1.4 ± 1.6 (–2.3–4.4)	1.4 ± 1.3 (–0.6–3.6)✧	1.4 ± 2.0 (–2.3–4.4)	–0.2 ± 1.7 (–3.7–2.1)✧
AI [%]	8.6 ± 15.6 (–41.1–28.5)✦	9.8 ± 9.0 (–6.4–19.5)✧	7.3 ± 21.3 (–41.1–28.5)	–1.4 ± 14.2 (–32.5–25.8)✦, ✧
TFS [mm ³]	185.0 ± 19.1 (150.3–218.4)	187.1 ± 17.4 (168.1–211.0)	182.4 ± 22.1 (150.3–218.4)	175.8 ± 19.6 (144.4–208.5)

✦ ANOVA for VP (all) vs. NP, where $p < 0.05$, or ✦✦ if $p < 0.001$

✧ ANOVA for VP (definite) vs. NP, where $p < 0.05$, or ✧✧ if $p < 0.001$

Abbreviations: Δ = difference between ipsilateral and contralateral side, AI asymmetry index, ELH endolymphatic hydrops, ELS endolymphatic space, sq semi-quantitative, v volumetric, TFS total fluid space

Some DTI studies showed microstructural alterations in fractional anisotropy (FA) and mean diffusivity (MD) values between affected and non-affected TiN sides [71–73] that could be used for postoperative longitudinal control [74]. However, other studies showed no correlation between DTI parameters and clinical symptoms, such as illness duration or severity of compression [75].

Mild ELH in VP discernible (aim iii)

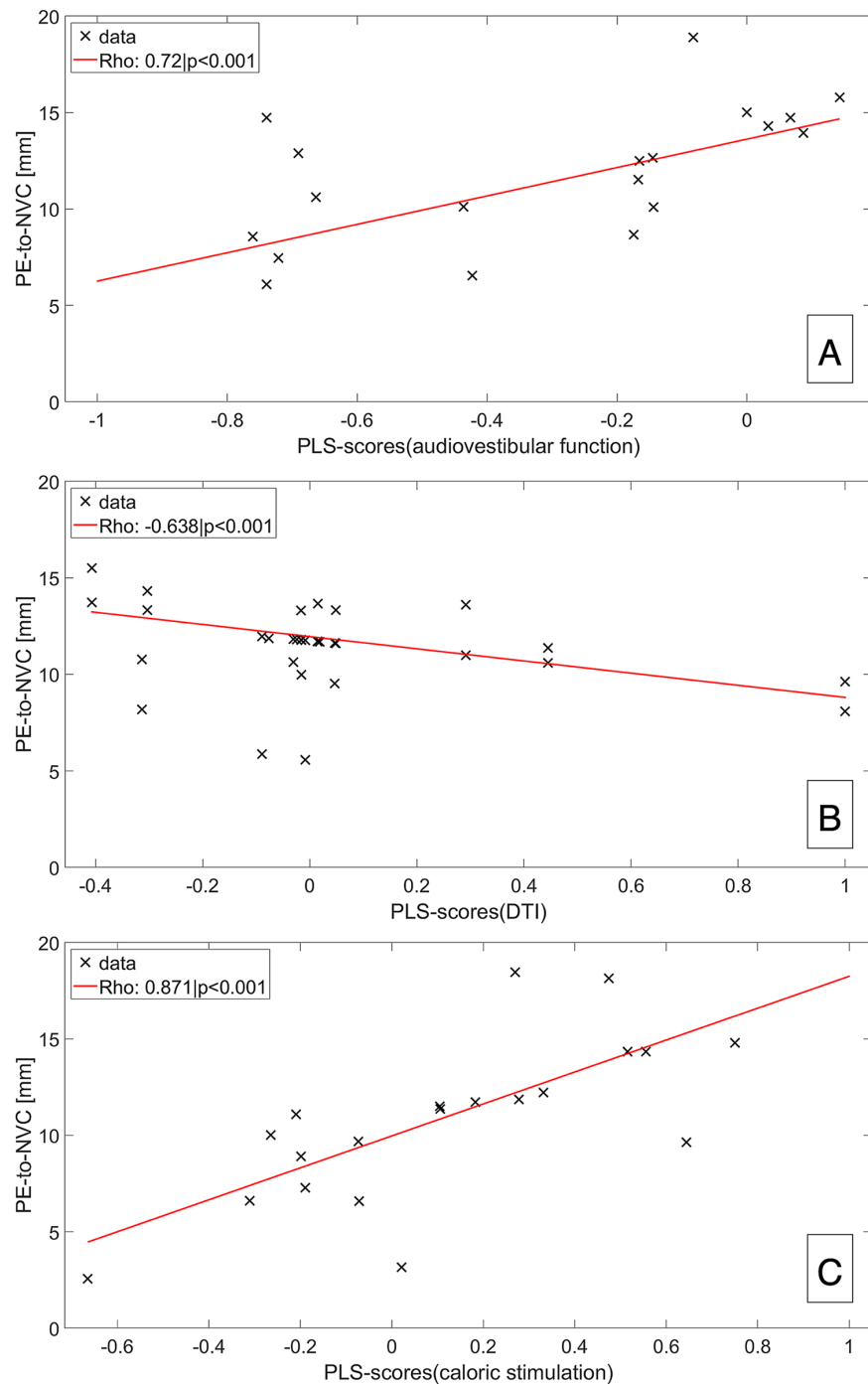
Following the 4-point ordinal scale, semi-quantitative classification of the ELS for the vestibulum and cochlea [49, 76], volumetric quantification in the current study disclosed a mild yet significantly increased asymmetry index of the inner ear and vestibulum when compared to NP. These findings are overlooked by a part of the 3-point ordinal scale ELH classification of the vestibulum [77]. This can be explained by the fact that these classifications were calibrated on patients with Ménière’s disease when ELH was viewed as pathognomonic to MD, which tends to have a larger ELH [17]. Fittingly and further underlying its pathophysiological relevance, varying degrees of ELH are also nearly universally present in post-mortem human temporal bone [78, 79] and iMRI studies on subjects with a history of MD [16, 18, 19, 32]. However, in-vivo iMRI studies also showed a relatively high prevalence in the healthy population (via iMRI [80], as well as in post-mortem studies [81]) and in patients with other vestibular disorders such as vestibular migraine [18, 19], vestibular schwannoma [82], or bilateral vestibulopathy [83]. Consequently, ELH is being re-evaluated as a non-pathognomonic phenomenon that should not directly indicate MD [84]. In this context, finer graduation in the lower ELH grades is useful not to overlook milder cases of ELH, be it in a 3-point ordinal scale [57] or a 4-point ordinal scale ELH classification of the vestibulum [49].

With respect to the current study, VP seems to be another vestibular disorder that can entail mild ELH. Although non-specific, this finding may be one of several parameters that help diagnose the affected side (view Fig. 3). ELH has been tied to many pathophysiological theories, such as post-viral autoimmune mechanisms, anatomic or vascular abnormalities affecting endolymph resorption, and different factors relating to water homeostasis [85–87]. The pathogenetic mechanism for higher inner ear ELS volumes in VP seems to be related to the NVC lying in the root entry zone of the intracisternal part of the eighth cranial nerve ($p < 0.001$). The nerve compression might then lead to a disturbance in the inner ear fluid homeostasis, either directly or via a central pathology inducing hyperexcitability within the cranial nerve nuclei or reduced inhibitory projection to the cranial nerve nuclei.

Interparametric analyses corroborate NVC syndrome (aim iv)

The nearer the NVC was to the PE, the poorer audiovestibular function ($p < 0.001$) and nerve structural integrity ($p < 0.001$), and the larger inner ear ELS ($p < 0.001$) were. The intracisternal part of the eighth nerve starts covered by central myelin (i.e., oligodendrocytes, also called root entry zone), then 6–15 mm as measured from the PE [88] oligodendrocytes change into Schwann cells [89], which is called the transition zone. The present interparametric analyses corroborate the pathophysiological theory [2, 10] that the intracisternal part of the eighth cranial nerve covered by central myelin (i.e., oligodendrocytes) seems to be particularly vulnerable for deficits induced by NVC and that the NVC seems to be a necessary precondition factor to develop VP.

Fig. 3 Interparametric correlations. Scatter plot depiction with trendlines of the correlations of “distance between PE and NVC (PE-to-NVC [mm])” and the eighth cranial nerve (A) audiovestibular function, i.e. neurophysiological testing (caloric stimulation, HIT and PTA), (B) structural nerve integrity (DTI SSPs, or deviations of successive DTI differences), and inner ear ELS volumes (C). A decreasing distance between PE to NVC can be translated into the transition zone of the eighth nerve (6–15 mm as measured from the PE, where oligodendrocytes change into Schwann cells [89]), and the root-entry zone from 6 mm downwards [88]. In consequence, the positive correlation of PE-to-NVC to audiovestibular function (A, Roh 0.72, $p < 0.001$) indicates better function the more the NVC lies outside the root-entry area of the intracisternal part of the eighth cranial nerve, and not covered by central myelin (oligodendrocytes), but peripheral myelin (Schwann cells). Conversely, the negative correlation of PE-to-NVC to nerval structural microstructure DTI SSPs (B, Roh -6.638 , $p < 0.001$), or inner ear ELS volumes (C, Roh -6.604 , $p < 0.001$) indicates less nerve deterioration, or less ELS volume the higher the PE-to-NVC distance. Altogether, these correlations link the subtle clinical, diagnostic, DTI-proxy for nerve microstructure, and ELS volume findings in VP to NVC, and in particular to NVC being in the root-entry zone. Abbreviations: *ELS* endolymphatic space, *NVC* neurovascular compression, *PE* point of entry/exit for afferent/efferent fibers out of/into the brainstem, *PE-to-NVC* distance between PE and NVC [mm], *SSP* summary statistic parameters, or deviations in successive differences.



Clinical implications and recommendations for future studies

In VP, no “vestibular” symptom has a precise meaning in topology or nosology [1], which makes corroborating

evidence from quantifiable features all the more critical. The current VP study should be understood as a proof-of-concept study for using MR imaging tailored to VP as a complementary clinical tool to investigate the vestibular end organ. On a single-subject level, MRI tailored to VP

can deliver additional quantifiable features for diagnosing VP. Especially the verification of NA and mild ELH can increase the overall predictive value of MRI. Nevertheless, the specificity of the methodology is not yet sufficient to diagnose VP by MR imaging.

The improvement of the MR sequences, especially DTI (as mentioned in “Mild ELH in VP discernible, (*aim iii*)”), holds potential. This study’s sequence acquisition parameters represent a compromise between novel technical possibilities, resolution, and reasonable scan time while enabling a wide range of clinical applications. Novel MR neurography imaging techniques might prove helpful for the investigation of the structural integrity of the vestibular nerve, such as high-resolution isotropic [90], driven equilibrium (drive) [91], or 3D cranial nerve [92] MR imaging. In addition, similar to trigeminal nerve analyses, atlas-based segmentation might prove helpful [93]. Another approach to improve the MRI investigation of the neurovascular compression site could be the addition of magnetic resonance subtraction [94]. Furthermore, techniques beyond DTI tractography might unlock the mesoscopic potential of diffusion-weighted imaging [95]. Another aspect would be to investigate the structural and functional connectivity and disturbances in cortical networks since there also seems to be a central aspect in the pathophysiology of VP.

Methodological limitations

Two major limitations of the current study need to be considered: First, the limited number of subjects included, and second, the circumstance that iMRI imaging for the control group (NP) could only be done in patients with other (neurological) pathologies that did not affect the peripheral or central vestibulocochlear systems. First, given the variation in symptomatology, a higher number of VP participants would be desirable. If possible, 20 participants per clinical pattern should be included. Second, influences of the NP’s underlying neurological pathologies on the ELS appeared unlikely (view inclusion and exclusion criteria, Sect. 2.2.) but cannot entirely be excluded. However, ethical considerations did not allow us to include healthy volunteers without a medical indication for an iMRI with contrast agent. The decision to avoid unnecessary contrast agent application was based on prior findings of signal intensity increases in the dentate nucleus and globus pallidus on T1-weighted MR images after applying MR contrast agents that are still under investigation [96–98]. Third, the study lacks histological confirmation of endolymphatic hydrops since the in-vivo acquisition of histological specimens is currently not possible.

Conclusion

This study is the first to link eighth cranial nerve function, microstructure, and endolymphatic space changes in VP patients to clinical features and neurovascular compression in the root-entry zone (correlation coefficient > 0.5, $p < 0.001$). Significant differences were reached at group level (ANOVA, $p < 0.05$, corrected for multiple testing). However, moderate specificity of MR NVC and NA evidence, DTI quantification, or ELH verification means they do not suffice to diagnose VP on a single-subject level.

Acknowledgements We thank K. Göttlinger for copyediting the manuscript.

Author contributions EK, JG, acquisition, and analysis of the data, drafting the manuscript; RB, BEW, conception, and design of the study, analysis of the data, drafting the manuscript; MD, conception, and design of the study, drafting the manuscript, providing funding; VK, conception, and design of the study, acquisition, and analysis of the data, drafting the manuscript, providing funding.

Funding Open Access funding enabled and organized by Projekt DEAL. This work was partially funded by the German Foundation of Neurology (Deutsche Stiftung Neurologie, DSN), Verein zur Förderung von Wissenschaft und Forschung an der Medizinischen Fakultät der LMU (Association for the Promotion of Science and Research at the LMU Medical Faculty), and the German Federal Ministry of Education and Research (BMBF) (Grant 01 EO 0901) via the German Center for Vertigo and Balance Disorders (DSGZ, grant number 01 EO 1401).

Declarations

Conflicts of interest There are no conflicts of interest.

Open Access This article is licensed under a Creative Commons Attribution 4.0 International License, which permits use, sharing, adaptation, distribution and reproduction in any medium or format, as long as you give appropriate credit to the original author(s) and the source, provide a link to the Creative Commons licence, and indicate if changes were made. The images or other third party material in this article are included in the article’s Creative Commons licence, unless indicated otherwise in a credit line to the material. If material is not included in the article’s Creative Commons licence and your intended use is not permitted by statutory regulation or exceeds the permitted use, you will need to obtain permission directly from the copyright holder. To view a copy of this licence, visit <http://creativecommons.org/licenses/by/4.0/>.

References

1. Brandt T, Dieterich M, Strupp M (2013) Vertigo and dizziness: common complaints, 2nd edn. Springer-Verlag, London
2. Brandt T, Dieterich M (1994) Vestibular paroxysmia: vascular compression of the eighth nerve? *Lancet* 343:798–799. [https://doi.org/10.1016/s0140-6736\(94\)91879-1](https://doi.org/10.1016/s0140-6736(94)91879-1)
3. Jannetta PJ, Møller MB, Møller AR (1984) Disabling positional vertigo. *N Engl J Med* 310:1700–1705. <https://doi.org/10.1056/NEJM198406283102604>

4. Møller MB, Møller AR (1990) Vascular compression syndrome of the eighth nerve. Clinical correlations and surgical findings. *Neurol Clin* 8:421–439
5. Strupp M, Lopez-Escamez JA, Kim J-S et al (2016) Vestibular paroxysmia: diagnostic criteria. *J Vestib Res* 26:409–415. <https://doi.org/10.3233/VES-160589>
6. Hüfner K, Barresi D, Glaser M et al (2008) Vestibular paroxysmia: diagnostic features and medical treatment. *Neurology* 71:1006–1014. <https://doi.org/10.1212/01.wnl.0000326594.91291.f8>
7. Straube A, Büttner U, Brandt T (1994) Recurrent attacks with skew deviation, torsional nystagmus, and contraction of the left frontalis muscle. *Neurology* 44:177–178. <https://doi.org/10.1212/wnl.44.1.177>
8. Jannetta PJ (1975) Neurovascular cross-compression in patients with hyperactive dysfunction symptoms of the eighth cranial nerve. *Surg Forum* 26:467–469
9. Strupp M, Planck JH, Arbusow V et al (2000) Rotational vertebral artery occlusion syndrome with vertigo due to “labyrinthine excitation.” *Neurology* 54:1376–1379. <https://doi.org/10.1212/wnl.54.6.1376>
10. Best C, Gawehn J, Krämer HH et al (2013) MRI and neurophysiology in vestibular paroxysmia: contradiction and correlation. *J Neurol Neurosurg Psychiatry* 84:1349–1356. <https://doi.org/10.1136/jnnp-2013-305513>
11. Arbusow V, Strupp M, Dieterich M et al (1998) Alternating episodes of vestibular nerve excitation and failure. *Neurology* 51:1480–1483. <https://doi.org/10.1212/wnl.51.5.1480>
12. Ryu H, Yamamoto S, Sugiyama K, Nozue M (1998) Neurovascular compression syndrome of the eighth cranial nerve. What are the most reliable diagnostic signs? *Acta Neurochir (Wien)* 140:1279–1286. <https://doi.org/10.1007/s007010050250>
13. Rommer PS, Wiest G, Kronnerwetter C et al (2015) 7-Tesla MRI demonstrates absence of structural lesions in patients with vestibular paroxysmia. *Front Neuroanat* 9:81. <https://doi.org/10.3389/fnana.2015.00081>
14. Sivarasan N, Touska P, Murdin L, Connor S (2019) MRI findings in vestibular paroxysmia—an observational study. *J Vestib Res* 29:137–145. <https://doi.org/10.3233/VES-190661>
15. Leal PRL, Roch JA, Hermier M et al (2011) Structural abnormalities of the trigeminal root revealed by diffusion tensor imaging in patients with trigeminal neuralgia caused by neurovascular compression: a prospective, double-blind, controlled study. *Pain* 152:2357–2364. <https://doi.org/10.1016/j.pain.2011.06.029>
16. Boegle R, Gerb J, Kierig E et al (2021) Intravenous delayed gadolinium-enhanced MR imaging of the endolymphatic space: a methodological comparative study. *Front Neurol* 12:647296. <https://doi.org/10.3389/fneur.2021.647296>
17. Nakashima T, Pyykkö I, Arroll MA et al (2016) Meniere’s disease. *Nat Rev Dis Primers* 2:16028. <https://doi.org/10.1038/nrdp.2016.28>
18. Oh S-Y, Dieterich M, Lee BN et al (2021) Endolymphatic hydrops in patients with vestibular migraine and concurrent Meniere’s disease. *Front Neurol* 12:594481. <https://doi.org/10.3389/fneur.2021.594481>
19. Nakada T, Yoshida T, Suga K et al (2014) Endolymphatic space size in patients with vestibular migraine and Ménière’s disease. *J Neurol* 261:2079–2084. <https://doi.org/10.1007/s00415-014-7458-9>
20. Oldfield RC (1971) The assessment and analysis of handedness: the Edinburgh inventory. *Neuropsychologia* 9:97–113. [https://doi.org/10.1016/0028-3932\(71\)90067-4](https://doi.org/10.1016/0028-3932(71)90067-4)
21. Dill T (2008) Contraindications to magnetic resonance imaging. *Heart* 94:943–948. <https://doi.org/10.1136/hrt.2007.125039>
22. Dieterich M, Brandt T (1993) Ocular torsion and tilt of subjective visual vertical are sensitive brainstem signs. *Ann Neurol* 33:292–299. <https://doi.org/10.1002/ana.410330311>
23. Halmagyi GM, Curthoys IS (1988) A clinical sign of canal paresis. *Arch Neurol* 45:737–739. <https://doi.org/10.1001/archneur.1988.00520310043015>
24. Schneider E, Villgratner T, Vockeroth J et al (2009) EyeSeeCam: an eye movement-driven head camera for the examination of natural visual exploration. *Ann NY Acad Sci* 1164:461–467. <https://doi.org/10.1111/j.1749-6632.2009.03858.x>
25. Strupp M, Kim J-S, Murofushi T et al (2017) Bilateral vestibulopathy: diagnostic criteria consensus document of the classification committee of the Bárány society. *J Vestib Res* 27:177–189. <https://doi.org/10.3233/VES-170619>
26. Jongkees LB, Maas JP, Philipszoon AJ (1962) Clinical nystagmography. A detailed study of electro-nystagmography in 341 patients with vertigo. *Pract Otorhinolaryngol (Basel)* 24:65–93
27. Agrawal Y, Van de Berg R, Wuys F et al (2019) Presbyvestibulopathy: diagnostic criteria consensus document of the classification committee of the Bárány Society. *J Vestib Res* 29:161–170. <https://doi.org/10.3233/VES-190672>
28. Długaiczek J, Habs M, Dieterich M (2020) Vestibular evoked myogenic potentials in vestibular migraine and Ménière’s disease: cVEMPs make the difference. *J Neurol* 267:169–180. <https://doi.org/10.1007/s00415-020-09902-4>
29. Curthoys IS, Długaiczek J (2020) Physiology, clinical evidence and diagnostic relevance of sound-induced and vibration-induced vestibular stimulation. *Curr Opin Neurol* 33:126–135. <https://doi.org/10.1097/WCO.0000000000000770>
30. Ertl M, Boegle R, Kirsch V, Dieterich M (2016) On the impact of examiners on latencies and amplitudes in cervical and ocular vestibular-evoked myogenic potentials evaluated over a large sample ($N = 1038$). *Eur Arch Otorhinolaryngol* 273:317–323. <https://doi.org/10.1007/s00405-015-3510-3>
31. Matsumoto M, Nishimura T (1998) Mersenne twister: a 623-dimensionally equidistributed uniform pseudo-random number generator. *ACM Trans Model Comput Simul* 8:3–30. <https://doi.org/10.1145/272991.272995>
32. Naganawa S, Yamazaki M, Kawai H et al (2010) Visualization of endolymphatic hydrops in Ménière’s disease with single-dose intravenous gadolinium-based contrast media using heavily T(2)-weighted 3D-FLAIR. *Magn Reson Med Sci* 9:237–242. <https://doi.org/10.2463/mrms.9.237>
33. Tournier J-D, Smith R, Raffelt D et al (2019) MRtrix3: A fast, flexible and open software framework for medical image processing and visualisation. *Neuroimage* 202:116137. <https://doi.org/10.1016/j.neuroimage.2019.116137>
34. Veraart J, Novikov DS, Christiaens D et al (2016) Denoising of diffusion MRI using random matrix theory. *Neuroimage* 142:394–406. <https://doi.org/10.1016/j.neuroimage.2016.08.016>
35. Cordero-Grande L, Christiaens D, Hutter J et al (2019) Complex diffusion-weighted image estimation via matrix recovery under general noise models. *Neuroimage* 200:391–404. <https://doi.org/10.1016/j.neuroimage.2019.06.039>
36. Fedorov A, Beichel R, Kalpathy-Cramer J et al (2012) 3D Slicer as an image computing platform for the Quantitative Imaging Network. *Magn Reson Imaging* 30:1323–1341. <https://doi.org/10.1016/j.mri.2012.05.001>
37. Smith SM (2002) Fast robust automated brain extraction. *Hum Brain Mapp* 17:143–155. <https://doi.org/10.1002/hbm.10062>
38. Schilling KG, Blaber J, Huo Y et al (2019) Synthesized b0 for diffusion distortion correction (Synb0-DisCo). *Magn Reson Imaging* 64:62–70. <https://doi.org/10.1016/j.mri.2019.05.008>
39. Andersson JLR, Skare S, Ashburner J (2003) How to correct susceptibility distortions in spin-echo echo-planar images: application to diffusion tensor imaging. *Neuroimage* 20:870–888. [https://doi.org/10.1016/S1053-8119\(03\)00336-7](https://doi.org/10.1016/S1053-8119(03)00336-7)
40. Andersson JLR, Graham MS, Drobnyak I et al (2018) Susceptibility-induced distortion that varies due to motion: correction

- in diffusion MR without acquiring additional data. *Neuroimage* 171:277–295. <https://doi.org/10.1016/j.neuroimage.2017.12.040>
41. Tustison N, Avants B, Cook P et al (2010) N4ITK: improved N3 bias correction. *IEEE Trans Med Imaging* 29:1310–1320. <https://doi.org/10.1109/tmi.2010.2046908>
 42. Maier-Hein KH, Neher PF, Houde J-C et al (2017) The challenge of mapping the human connectome based on diffusion tractography. *Nat Commun* 8:1349. <https://doi.org/10.1038/s41467-017-01285-x>
 43. Yeh F-C, Verstyne TD, Wang Y et al (2013) Deterministic diffusion fiber tracking improved by quantitative anisotropy. *PLoS ONE* 8:e80713. <https://doi.org/10.1371/journal.pone.0080713>
 44. Yeh F-C (2020) Shape analysis of the human association pathways. *Neuroimage* 223:117329. <https://doi.org/10.1016/j.neuroimage.2020.117329>
 45. Berrett TB, Samworth RJ, Yuan M (2019) Efficient multivariate entropy estimation via k-nearest neighbour distances. *Ann Statist*. <https://doi.org/10.1214/18-AOS1688>
 46. McIntosh AR, Lobaugh NJ (2004) Partial least squares analysis of neuroimaging data: applications and advances. *Neuroimage* 23:S250–S263. <https://doi.org/10.1016/j.neuroimage.2004.07.020>
 47. McIntosh AR, Bookstein FL, Haxby JV, Grady CL (1996) Spatial pattern analysis of functional brain images using partial least squares. *Neuroimage* 3:143–157. <https://doi.org/10.1006/nimg.1996.0016>
 48. Cyran CAM, Boegle R, Stephan T et al (2016) Age-related decline in functional connectivity of the vestibular cortical network. *Brain Struct Funct* 221:1443–1463. <https://doi.org/10.1007/s00429-014-0983-6>
 49. Boegle R, Gerb J, Kierig E et al (2021) Intravenous delayed Gadolinium-enhanced MR imaging of the endolymphatic space: A methodical comparative study. *Front Neurol* <https://doi.org/10.3389/fneur.2021.647296>
 50. Ahmadi S-A, Frei J, Vivar G et al (2022) IE-Vnet: deep learning-based segmentation of the inner ear's total fluid space. *Front Neurol* 13:663200. <https://doi.org/10.3389/fneur.2022.663200>
 51. Milletari F, Frei J, Aboulatta M et al (2019) Cloud deployment of high-resolution medical image analysis with TOMAAT. *IEEE J Biomed Health Inform* 23:969–977. <https://doi.org/10.1109/JBHI.2018.2885214>
 52. Gerb J, Ahmadi SA, Kierig E et al (2020) VOLT: a novel open-source pipeline for automatic segmentation of endolymphatic space in inner ear MRI. *J Neurol* 267:185–196. <https://doi.org/10.1007/s00415-020-10062-8>
 53. Schindelin J, Arganda-Carreras I, Frise E et al (2012) Fiji: an open-source platform for biological-image analysis. *Nat Methods* 9:676–682. <https://doi.org/10.1038/nmeth.2019>
 54. Nizamutdinov V (2015) Neural network and fuzzy logic based plugins for imagej
 55. Legland D, Arganda-Carreras I, Andrey P (2016) MorphoLibJ: integrated library and plugins for mathematical morphology with ImageJ. *Bioinformatics* 32:3532–3534. <https://doi.org/10.1093/bioinformatics/btw413>
 56. Garrett DD, Kovacevic N, McIntosh AR, Grady CL (2011) The importance of being variable. *J Neurosci* 31:4496–4503. <https://doi.org/10.1523/JNEUROSCI.5641-10.2011>
 57. Nakashima T, Naganawa S, Pyykkö I et al (2009) Grading of endolymphatic hydrops using magnetic resonance imaging. *Acta Otolaryngol Suppl*. <https://doi.org/10.1080/00016480902729827>
 58. Gardner WJ (1966) Cross talk—the paradoxical transmission of a nerve impulse. *Arch Neurol* 14:149–156. <https://doi.org/10.1001/archneur.1966.00470080033005>
 59. Nielsen VK (1984) Pathophysiology of hemifacial spasm: I. Ephaptic transmission and ectopic excitation. *Neurology* 34:418–426. <https://doi.org/10.1212/wnl.34.4.418>
 60. Granit R, Leksell L, Skoglund CR (1944) Fibre interaction in injured or compressed region of nerve. *Brain* 67:125–140. <https://doi.org/10.1093/brain/67.2.125>
 61. Esteban A, Molina-Negro P (1986) Primary hemifacial spasm: a neurophysiological study. *J Neurol Neurosurg Psychiatry* 49:58–63. <https://doi.org/10.1136/jnnp.49.1.58>
 62. Ishikawa M, Ohira T, Namiki J et al (1997) Electrophysiological investigation of hemifacial spasm after microvascular decompression: F waves of the facial muscles, blink reflexes, and abnormal muscle responses. *J Neurosurg* 86:654–661. <https://doi.org/10.3171/jns.1997.86.4.0654>
 63. Möller AR (1999) Vascular compression of cranial nerves: II: pathophysiology. *Neurol Res* 21:439–443
 64. Bergsneider M, Becker DP (1995) Vascular compression syndrome of the vestibular nerve: a critical analysis. *Otolaryngol Head Neck Surg* 112:118–124. [https://doi.org/10.1016/s0194-5998\(95\)70310-1](https://doi.org/10.1016/s0194-5998(95)70310-1)
 65. Teh CS-L, Noordiana SH, Shamini S, Prepageran N (2021) Vascular loops: the innocent bystander for vestibular Paroxysmia. *Ann Otol Rhinol Laryngol*. <https://doi.org/10.1177/00034894211037211>
 66. Danyluk H, Sankar T, Beaulieu C (2021) High spatial resolution nerve-specific DTI protocol outperforms whole-brain DTI protocol for imaging the trigeminal nerve in healthy individuals. *NMR Biomed* 34:e4427. <https://doi.org/10.1002/nbm.4427>
 67. Xie G, Zhang F, Leung L et al (2020) Anatomical assessment of trigeminal nerve tractography using diffusion MRI: a comparison of acquisition b-values and single- and multi-fiber tracking strategies. *Neuroimage Clin* 25:102160. <https://doi.org/10.1016/j.nicl.2019.102160>
 68. Cheng J, Basser PJ (2018) Director Field Analysis (DFA): exploring local white matter geometric structure in diffusion MRI. *Med Image Anal* 43:112–128. <https://doi.org/10.1016/j.media.2017.10.003>
 69. Jeurissen B, Tournier J-D, Dhollander T et al (2014) Multi-tissue constrained spherical deconvolution for improved analysis of multi-shell diffusion MRI data. *Neuroimage* 103:411–426. <https://doi.org/10.1016/j.neuroimage.2014.07.061>
 70. Jannetta PJ (1981) Cranial nerve vascular compression syndromes (other than tic douloureux and hemifacial spasm). *Clin Neurosurg* 28:445–456. https://doi.org/10.1093/neurosurgery/28.cn_suppl_1.445
 71. Chai W, You C, Zhang W et al (2019) Diffusion tensor imaging of microstructural alterations in the trigeminal nerve due to neurovascular contact/compression. *Acta Neurochir (Wien)* 161:1407–1413. <https://doi.org/10.1007/s00701-019-03851-2>
 72. DeSouza DD, Hodaie M, Davis KD (2016) Structural magnetic resonance imaging can identify trigeminal system abnormalities in classical trigeminal neuralgia. *Front Neuroanat* 10:95. <https://doi.org/10.3389/fnana.2016.00095>
 73. Zhang Y, Mao Z, Cui Z et al (2018) Diffusion tensor imaging of axonal and myelin changes in classical trigeminal neuralgia. *World Neurosurg* 112:e597–e607. <https://doi.org/10.1016/j.wneu.2018.01.095>
 74. Wu M, Qiu J, Jiang X et al (2020) Diffusion tensor imaging reveals microstructural alteration of the trigeminal nerve root in classical trigeminal neuralgia without neurovascular compression and correlation with outcome after internal neurectomy. *Magn Reson Imaging* 71:37–44. <https://doi.org/10.1016/j.mri.2020.05.006>
 75. Lutz J, Thon N, Stahl R et al (2016) Microstructural alterations in trigeminal neuralgia determined by diffusion tensor imaging are independent of symptom duration, severity, and type of neurovascular conflict. *J Neurosurg* 124:823–830. <https://doi.org/10.3171/2015.2.JNS142587>
 76. Kirsch V, Becker-Bense S, Berman A et al (2018) Transient endolymphatic hydrops after an attack of vestibular migraine: a

- longitudinal single case study. *J Neurol* 265:51–53. <https://doi.org/10.1007/s00415-018-8870-3>
77. Baráth K, Schuknecht B, Naldi AM et al (2014) Detection and grading of endolymphatic hydrops in Menière disease using MR imaging. *Am J Neuroradiol* 35:1387–1392. <https://doi.org/10.3174/ajnr.A3856>
 78. Rauch SD, Merchant SN, Thedinger BA (1989) Meniere's syndrome and endolymphatic hydrops. Double-blind temporal bone study. *Ann Otol Rhinol Laryngol* 98:873–883. <https://doi.org/10.1177/000348948909801108>
 79. Frayssse BG, Alonso A, House WF (1980) Menière's disease and endolymphatic hydrops: clinical-histopathological correlations. *Ann Otol Rhinol Laryngol Suppl* 89:2–22. <https://doi.org/10.1177/00034894800896s201>
 80. Ito T, Inui H, Miyasaka T et al (2019) Endolymphatic volume in patients with meniere's disease and healthy controls: three-dimensional analysis with magnetic resonance imaging. *Laryngoscope* 4:653–658. <https://doi.org/10.1002/lio2.313>
 81. Brantberg K, Trees N, Baloh RW (2005) Migraine-associated vertigo. *Acta Otolaryngol* 125:276–279. <https://doi.org/10.1080/00016480510003165>
 82. Eliezer M, Poillon G, Maquet C et al (2019) Sensorineural hearing loss in patients with vestibular schwannoma correlates with the presence of utricular hydrops as diagnosed on heavily T2-weighted MRI. *Diagn Interv Imaging* 100:259–268. <https://doi.org/10.1016/j.diii.2019.01.006>
 83. Eliezer M, Hautefort C, Van Nechel C et al (2020) Electrophysiological and inner ear MRI findings in patients with bilateral vestibulopathy. *Eur Arch Otorhinolaryngol* 277:1305–1314. <https://doi.org/10.1007/s00405-020-05829-8>
 84. van der Lubbe MFJA, Vaidyanathan A, Van Rompaey V et al (2020) The “hype” of hydrops in classifying vestibular disorders: a narrative review. *J Neurol* 267:197–211. <https://doi.org/10.1007/s00415-020-10278-8>
 85. Salt AN, Plontke SK (2010) Endolymphatic hydrops: pathophysiology and experimental models. *Otolaryngol Clin North Am* 43:971–983. <https://doi.org/10.1016/j.otc.2010.05.007>
 86. Ishiyama G, Lopez IA, Ishiyama P et al (2017) The blood labyrinthine barrier in the human normal and Meniere's disease macula utricule. *Sci Rep* 7:253. <https://doi.org/10.1038/s41598-017-00330-5>
 87. Møller MN, Kirkeby S, Cayé-Thomasen P (2017) Innate immune defense in the inner ear—mucines are expressed by the human endolymphatic sac. *J Anat* 230:297–302. <https://doi.org/10.1111/joa.12559>
 88. Lang J (1982) Anatomy, length and blood vessel relations of “central” and “peripheral” paths of intracisternal cranial nerves. *Zentralbl Neurochir* 43:217–258
 89. De Ridder D, Møller A, Verlooy J et al (2002) Is the root entry/exit zone important in microvascular compression syndromes? *Neurosurgery* 51:427–434. <https://doi.org/10.1097/00006123-20028000-00023>
 90. Wen J, Desai NS, Jeffery D et al (2018) High-resolution isotropic three-dimensional MR imaging of the extraforaminal segments of the cranial nerves. *Magn Reson Imaging Clin N Am* 26:101–119. <https://doi.org/10.1016/j.mric.2017.08.007>
 91. Ciftci E, Anik Y, Arslan A et al (2004) Driven equilibrium (drive) MR imaging of the cranial nerves V–VIII: comparison with the T2-weighted 3D TSE sequence. *Eur J Radiol* 51:234–240. <https://doi.org/10.1016/j.ejrad.2003.10.019>
 92. Van der Cruyssen F, Croonenborghs T-M, Hermans R et al (2021) 3D cranial nerve imaging, a novel MR neurography technique using black-blood STIR TSE with a pseudo steady-state sweep and motion-sensitized driven equilibrium pulse for the visualization of the extraforaminal cranial nerve branches. *Am J Neuroradiol* 42:578–580. <https://doi.org/10.3174/ajnr.A6904>
 93. Zhang F, Xie G, Leung L et al (2020) Creation of a novel trigeminal tractography atlas for automated trigeminal nerve identification. *Neuroimage* 220:117063. <https://doi.org/10.1016/j.neuroimage.2020.117063>
 94. Liao Z, Zou L, Peng W et al (2021) Improving the accuracy of pre-operative evaluation of neurovascular conflict in trigeminal neuralgia using magnetic resonance subtraction. *Neuroradiology* 63:295–303. <https://doi.org/10.1007/s00234-020-02624-4>
 95. Novikov DS, Fieremans E, Jespersen SN, Kiselev VG (2019) Quantifying brain microstructure with diffusion MRI: theory and parameter estimation. *NMR Biomed* 32:e3998. <https://doi.org/10.1002/nbm.3998>
 96. Adin ME, Kleinberg L, Vaidya D et al (2015) Hyperintense dentate nuclei on T1-weighted MRI: relation to repeat gadolinium administration. *Am J Neuroradiol* 36:1859–1865. <https://doi.org/10.3174/ajnr.A4378>
 97. Moser FG, Watterson CT, Weiss S et al (2018) High signal intensity in the dentate nucleus and globus pallidus on unenhanced T1-weighted MR images: comparison between gadobutrol and linear gadolinium-based contrast agents. *Am J Neuroradiol* 39:421–426. <https://doi.org/10.3174/ajnr.A5538>
 98. Errante Y, Cirimele V, Mallio CA et al (2014) Progressive increase of T1 signal intensity of the dentate nucleus on unenhanced magnetic resonance images is associated with cumulative doses of intravenously administered gadodiamide in patients with normal renal function, suggesting dechelation. *Invest Radiol* 49:685–690. <https://doi.org/10.1097/RLI.0000000000000072>

Literaturverzeichnis

- Ahmadi, S.-A. *et al.* (2022) 'IE-Vnet: Deep Learning-Based Segmentation of the Inner Ear's Total Fluid Space', *Frontiers in Neurology*, 13. Available at: <https://www.frontiersin.org/articles/10.3389/fneur.2022.663200>.
- Angelaki, D.E. *et al.* (2004) 'Neurons compute internal models of the physical laws of motion', *Nature*, 430(6999), pp. 560–564. Available at: <https://doi.org/10.1038/nature02754>.
- Bagger-Sjöbäck, D., Friberg, U. and Rask-Anderson, H. (1986) 'The human endolymphatic sac. An ultrastructural study.', *Arch Otolaryngol Head Neck Surg*, 112(4), pp. 398–409. Available at: <https://doi.org/10.1001/archotol.1986.03780040038008>.
- Baier, B. *et al.* (2012) 'Neural correlates of disturbed perception of verticality', *Neurology*, 78(10), pp. 728–735. Available at: <https://doi.org/10.1212/wnl.0b013e318248e544>.
- Baier, B. *et al.* (2016) 'Vestibular thalamus Two distinct graviceptive pathways', *Neurology*, 86(2), pp. 134–140. Available at: <https://doi.org/10.1212/wnl.0000000000002238>.
- Bandettini, P.A. *et al.* (1992) 'Time course EPI of human brain function during task activation', *Magnetic Resonance in Medicine*, 25(2), pp. 390–397. Available at: <https://doi.org/10.1002/mrm.1910250220>.
- Baumgärtner, U. *et al.* (2010) 'Multiple somatotopic representations of heat and mechanical pain in the operculo-insular cortex: a high-resolution fMRI study.', *Journal of neurophysiology*, 104(5), pp. 2863–2872. Available at: <https://doi.org/10.1152/jn.00253.2010>.
- Beckmann, C.F. *et al.* (2005) 'Investigations into resting-state connectivity using independent component analysis', *Philos Trans R Soc Lond B Biol Sci*, 360(1457), pp. 1001–1013. Available at: <https://doi.org/10.1098/rstb.2005.1634>.
- Beckmann, C.F. (2012) 'Modelling with independent components.', *Neuroimage*, 62(2), pp. 891–901. Available at: <https://doi.org/10.1016/j.neuroimage.2012.02.020>.
- Beckmann, C.F. and Smith, S.M. (2004) 'Probabilistic Independent Component Analysis for Functional Magnetic Resonance Imaging', *IEEE Transactions on Medical Imaging*, 23(2), pp. 137–152. Available at: <https://doi.org/10.1109/tmi.2003.822821>.
- Berthoz, A. *et al.* (1995) 'Spatial memory of body linear displacement: what is being stored?', *Science*, 269(5220), pp. 95–98. Available at: <https://doi.org/10.1126/science.7604286>.
- Best, C. *et al.* (2013) 'MRI and neurophysiology in vestibular paroxysmia: Contradiction and correlation', *Journal of Neurology, Neurosurgery and Psychiatry*, 84(12), pp. 1349–1356. Available at: <https://doi.org/10.1136/jnnp-2013-305513>.
- Biswal, B. *et al.* (1995) 'Functional connectivity in the motor cortex of resting human brain using echo-planar MRI.', *Magn Reson Med*, 34(4), pp. 537–541. Available at: <https://doi.org/10.1002/mrm.1910340409>.
- Blum, P.S. *et al.* (1979) 'Thalamic components of the ascending vestibular system', *Experimental Neurology*, 64(3), pp. 587–603. Available at: [https://doi.org/10.1016/0014-4886\(79\)90234-6](https://doi.org/10.1016/0014-4886(79)90234-6).
- Boegle, R. *et al.* (2021) 'Intravenous Delayed Gadolinium-Enhanced MR Imaging of the Endolymphatic Space: A Methodological Comparative Study', *Frontiers in Neurology*, 12, p. 647296. Available at: <https://doi.org/10.3389/fneur.2021.647296>.
- Bottini, G. *et al.* (1995) 'Modulation of conscious experience by peripheral sensory stimuli', *Nature*, 376(6543), pp. 778–781. Available at: <https://doi.org/10.1038/376778a0>.
- Brandt, T. (1998) 'Reciprocal inhibitory visual-vestibular interaction. Visual motion stimulation deactivates the parieto-insular vestibular cortex', *Brain*, 121(9), pp. 1749–1758. Available at: <https://doi.org/10.1093/brain/121.9.1749>.
- Brandt, T. *et al.* (2002) 'Visual-vestibular and visuovisual cortical interaction: new insights from fMRI and pet.', *Annals of the New York Academy of Sciences*, 956, pp. 230–241. Available at: <https://doi.org/10.1111/j.1749->

6632.2002.tb02822.x.

Brandt, T. and Dieterich, M. (1994a) 'Vestibular paroxysmia: vascular compression of the eighth nerve?', *The Lancet*, 343(8900), pp. 798–799. Available at: [https://doi.org/10.1016/S0140-6736\(94\)91879-1](https://doi.org/10.1016/S0140-6736(94)91879-1).

Brandt, T. and Dieterich, M. (1994b) 'VIIIth nerve vascular compression syndrome: vestibular paroxysmia', *Bailliere's Clinical Neurology*, 3(3), pp. 565–575.

Brandt, T. and Dieterich, M. (1999) 'The vestibular cortex. Its locations, functions, and disorders', *Annals of the New York Academy of Sciences*, 871, pp. 293–312. Available at: <https://doi.org/10.1111/j.1749-6632.1999.tb09193.x>.

Brandt, T., Dieterich, M. and Danek, A. (1994) 'Vestibular cortex lesions affect the perception of verticality.', *Annals of neurology*, 35, pp. 403–412. Available at: <https://doi.org/10.1002/ana.410350406>.

Brandt, T., Dieterich, M. and Strupp, M. (2013) 'Zentrale Schwindelsyndrome', in T. Brandt, M. Dieterich, and M. Strupp (eds) *Vertigo – Leitsymptom Schwindel*. Berlin, Heidelberg: Springer Berlin Heidelberg, pp. 79–100. Available at: https://doi.org/10.1007/978-3-642-24963-1_3.

Bucher, S.F. *et al.* (1998) 'Cerebral functional magnetic resonance imaging of vestibular, auditory, and nociceptive areas during galvanic stimulation', *Annals of Neurology*, 44(1), pp. 120–125. Available at: <https://doi.org/10.1002/ana.410440118>.

Büttner, U. and Lang, W. (1979) 'The vestibulocortical pathway: neurophysiological and anatomical studies in the monkey.', *Progress in brain research*, 50, pp. 581–588. Available at: [https://doi.org/10.1016/S0079-6123\(08\)60856-0](https://doi.org/10.1016/S0079-6123(08)60856-0).

Büttner-Ennever, J.A. (1992) 'Patterns of connectivity in the vestibular nuclei', *Annals of the New York Academy of Sciences*, 656, pp. 363–378. Available at: <https://doi.org/10.1111/j.1749-6632.1992.tb25222.x>.

Büttner-Ennever, J.A. (1999) 'A review of otolith pathways to brainstem and cerebellum.', *Annals of the New York Academy of Sciences*, 871, pp. 51–64.

Buxton, R.B. and Frank, L.R. (1997) 'A model for the coupling between cerebral blood flow and oxygen metabolism during neural stimulation', *Journal of Cerebral Blood Flow and Metabolism*, 17(1), pp. 64–72. Available at: <https://doi.org/10.1097/00004647-199701000-00009>.

Buxton, R.B., Wong, E.C. and Frank, L.R. (1998) 'Dynamics of blood flow and oxygenation changes during brain activation: the balloon model.', *Magnetic resonance in medicine*, 39(6), pp. 855–864. Available at: <https://doi.org/10.1002/mrm.1910390602>.

Carpenter, M.B. (1963) 'The Vestibular Nuclei and Their Connections, Anatomy and Functional Correlations.', *Archives of Neurology*, 8(3), pp. 345–346. Available at: <https://doi.org/10.1001/archneur.1963.00460030129016>.

Chen, Y.-J. and Young, Y.-H. (2016) 'Secondary Endolymphatic Hydrops After Acoustic Trauma', *Otology & Neurotology*, 37(5), p. 428. Available at: <https://doi.org/10.1097/mao.0000000000001036>.

Cinciute, S. (2019) 'Translating the hemodynamic response: Why focused interdisciplinary integration should matter for the future of functional neuroimaging', *PeerJ*, 2019(3). Available at: <https://doi.org/10.7717/peerj.6621>.

Conrad, J., Baier, B. and Dieterich, M. (2014) 'The role of the thalamus in the human subcortical vestibular system', *Journal of Vestibular Research: Equilibrium and Orientation*, 24(5), pp. 375–385. Available at: <https://doi.org/10.3233/ves-140534>.

Davis, T.L. *et al.* (1998) 'Calibrated functional MRI: Mapping the dynamics of oxidative metabolism', *Proceedings of the National Academy of Sciences of the United States of America*, 95(4), pp. 1834–1839. Available at: <https://doi.org/10.1073/pnas.95.4.1834>.

De Ridder, D. *et al.* (2002) 'Is the root entry/exit zone important in microvascular compression syndromes?', *Neurosurgery*, 51(2), pp. 427–33; discussion 433–4. Available at: <https://doi.org/10.1097/00006123-200208000-00023>.

Dieterich, M. *et al.* (2003) 'Dominance for vestibular cortical function in the non-dominant hemisphere', *Cerebral Cortex (New York, N.Y.: 1991)*, 13(9), pp. 994–1007. Available at: <https://doi.org/10.1093/cercor/13.9.994>.

- Dieterich, M. *et al.* (2005) 'Thalamic infarctions cause side-specific suppression of vestibular cortex activations', *Brain*, 128(9), pp. 2052–2067. Available at: <https://doi.org/10.1093/brain/awh551>.
- Dieterich, M. and Brandt, T. (1993) 'Thalamic infarctions: differential effects on vestibular function in the roll plane', *Neurology*, 43(9), pp. 1732–1740. Available at: <https://doi.org/10.1212/wnl.43.9.1732>.
- Dieterich, M. and Brandt, T. (2015) 'The bilateral central vestibular system: its pathways, functions, and disorders.', *Annals of the New York Academy of Sciences*, 1343, pp. 1–17. Available at: <https://doi.org/10.1111/nyas.12585>.
- Eickhoff, S.B. *et al.* (2015) 'Connectivity-based parcellation: Critique and implications', *Human Brain Mapping*, 36(12). Available at: <https://doi.org/10.1002/hbm.22933>.
- Emri, M. *et al.* (2003) 'Cortical projection of peripheral vestibular signaling.', *Journal of neurophysiology*, 89(5), pp. 2639–2646. Available at: <https://doi.org/10.1152/jn.00599.2002>.
- Esteban, A. and Molina-Negro, P. (1986) 'Primary hemifacial spasm: a neurophysiological study', *Journal of Neurology, Neurosurgery, and Psychiatry*, 49(1), pp. 58–63. Available at: <https://doi.org/10.1136/jnnp.49.1.58>.
- Fasold, O. *et al.* (2002) 'Human vestibular cortex as identified with caloric stimulation in functional magnetic resonance imaging.', *NeuroImage*, 17(3), pp. 1384–1393. Available at: <https://doi.org/doi:10.1006/nimg.2002.1241>.
- Feigenspan, A. (2017) 'Hören und Gleichgewicht', in A. Feigenspan (ed.) *Prinzipien der Physiologie*. Berlin, Heidelberg: Springer Berlin Heidelberg, pp. 599–638. Available at: https://doi.org/10.1007/978-3-662-54117-3_14.
- Ferster, A.P.O.C. *et al.* (2017) 'Secondary Endolymphatic Hydrops', *Otology and Neurotology*, 38(5), pp. 774–779. Available at: <https://doi.org/10.1097/mao.0000000000001377>.
- Fetter, M. (2010) 'Elektrookulographie - Vestibuläres System', *Das Neurophysiologie-Labor*, 32(3), pp. 129–140. Available at: <https://doi.org/10.1016/j.neulab.2010.04.005>.
- Gerb, J. *et al.* (2020) 'VOLT: a novel open-source pipeline for automatic segmentation of endolymphatic space in inner ear MRI', *Journal of Neurology*, 267(1), pp. 185–196. Available at: <https://doi.org/10.1007/s00415-020-10062-8>.
- Greicius, M.D. *et al.* (2009) 'Resting-state functional connectivity reflects structural connectivity in the default mode network.', *Cerebral Cortex*, 19(1), pp. 72–78. Available at: <https://doi.org/10.1093/cercor/bhn059>.
- Guldin, W.O., Akbarian, S. and Grüsser, O.J. (1992) 'Cortico-cortical connections and cytoarchitectonics of the primate vestibular cortex: a study in squirrel monkeys (*Saimiri sciureus*).', *The Journal of comparative neurology*, 326(3), pp. 375–401. Available at: <https://doi.org/10.1002/cne.903260306>.
- Guldin, W.O. and Grüsser, O.J. (1998) 'Is there a vestibular cortex?', *Trends in Neurosciences*, 21(6), pp. 254–259. Available at: [https://doi.org/10.1016/S0166-2236\(97\)01211-3](https://doi.org/10.1016/S0166-2236(97)01211-3).
- Gürkov, R. *et al.* (2016) 'What is Menière's disease? A contemporary re-evaluation of endolymphatic hydrops', *Journal of Neurology*, 263, pp. 71–81. Available at: <https://doi.org/10.1007/s00415-015-7930-1>.
- Homann, G. *et al.* (2015) 'Semi-Quantitative vs. Volumetric Determination of Endolymphatic Space in Menière's Disease Using Endolymphatic Hydrops 3T-HR-MRI after Intravenous Gadolinium Injection', *Plos One*, 10(3), p. e0120357. Available at: <https://doi.org/10.1371/journal.pone.0120357>.
- Hüfner, K. *et al.* (2008) 'Vestibular paroxysmia: diagnostic features and medical treatment.', *Neurology*, 71(13), pp. 1006–14. Available at: <https://doi.org/10.1212/01.wnl.0000326594.91291.f8>.
- Hyvärinen, A. (2013) 'Independent component analysis: recent advances', *Philosophical Transactions. Series A, Mathematical, Physical, and Engineering Sciences*, 371(1984), p. 20110534. Available at: <https://doi.org/10.1098/rsta.2011.0534>.
- Inamoto, R. *et al.* (2009) 'Endolymphatic sac is involved in the regulation of hydrostatic pressure of cochlear endolymph', *American Journal of Physiology. Regulatory, Integrative and Comparative Physiology*, 297(5), pp. R1610-1614. Available at: <https://doi.org/10.1152/ajpregu.00073.2009>.
- Ishikawa, M. *et al.* (1997) 'Electrophysiological investigation of hemifacial spasm after microvascular decompression: F waves of the facial muscles, blink reflexes, and abnormal muscle responses', *Journal of Neurosurgery*, 86(4), pp.

654–661. Available at: <https://doi.org/10.3171/jns.1997.86.4.0654>.

Jannetta, P.J. (1975) 'Neurovascular cross-compression in patients with hyperactive dysfunction symptoms of the eighth cranial nerve', *Surgical Forum*, 26, pp. 467–469.

Jannetta, P.J. (1979) 'Microsurgery of Cranial Nerve Cross-Compression', in *Neurosurgery, Volume 26, Issue CN_suppl_1, 1 January 1979, Pages 607–615*. Available at: https://doi.org/doi.org/10.1093/neurosurgery/26.CN_suppl_1.607.

Jannetta, P.J. *et al.* (1986) 'Neurosurgical treatment of vertigo by microvascular decompression of the eighth cranial nerve', *Clinical neurosurgery*, 33, pp. 645–665.

Jannetta, P.J., Møller, M.B. and Møller, A.R. (1984) 'Disabling Positional Vertigo', *New England Journal of Medicine*, 310(26), pp. 1700–1705. Available at: <https://doi.org/10.1056/nejm198406283102604>.

Karamitros, A. *et al.* (2022) 'Vestibular paroxysmia: Clinical features and imaging findings; a literature review', *Journal of Neuroradiology = Journal De Neuroradiologie*, 49(2), pp. 225–233. Available at: <https://doi.org/10.1016/j.neurad.2021.07.007>.

Kathleen E. Cullen (2014) 'The vestibular system: multimodal integration and encoding of self-motion for motor control', *Trends in Neurosciences*, 35(3), pp. 1–7. Available at: <https://doi.org/10.1016/j.tins.2011.12.001>.The.

Kimura, R.S. and Schuknecht, H.F. (2010) 'Membranous Hydrops in the Inner Ear of the Guinea Pig after Obliteration of the Endolymphatic Sac', *Practica Oto-Rhino-Laryngologica*, 27(6), pp. 343–354. Available at: <https://doi.org/10.1159/000274693>.

Kirsch, V. *et al.* (2015) 'Structural and functional connectivity mapping of the vestibular circuitry from human brainstem to cortex', *Brain Structure and Function*, 221(3), pp. 1291–308. Available at: <https://doi.org/10.1007/s00429-014-0971-x>.

Kirsch, V *et al.* (2018) 'High-resolution MRI of the inner ear enables syndrome differentiation and specific treatment of cerebellar downbeat nystagmus and secondary endolymphatic hydrops in a postoperative ELST patient', *Journal of Neurology*, 265(S1), pp. 48–50. Available at: <https://doi.org/10.1007/s00415-018-8858-z>.

Kirsch, Valerie *et al.* (2018) 'Transient endolymphatic hydrops after an attack of vestibular migraine: a longitudinal single case study', *Journal of Neurology*, 265(S1), pp. 51–53. Available at: <https://doi.org/10.1007/s00415-018-8870-3>.

Kiviniemi, V. *et al.* (2003) 'Independent component analysis of nondeterministic fMRI signal sources', *NeuroImage*, 19(2), pp. 253–260. Available at: [https://doi.org/10.1016/S1053-8119\(03\)00097-1](https://doi.org/10.1016/S1053-8119(03)00097-1).

Kwong, K.K. *et al.* (1992) 'Dynamic magnetic resonance imaging of human brain activity during primary sensory stimulation.', *Proceedings of the National Academy of Sciences*, 89(12), pp. 5675–5679. Available at: <https://doi.org/10.1073/pnas.89.12.5675>.

Le Bihan, D. (1995) 'Molecular diffusion, tissue microdynamics and microstructure', *NMR in biomedicine*, 8(7–8), pp. 375–386. Available at: <https://doi.org/10.1002/nbm.1940080711>.

Le Bihan, D. *et al.* (2001) 'Diffusion tensor imaging: Concepts and applications', *Journal of Magnetic Resonance Imaging*, 13(4), pp. 534–546. Available at: <https://doi.org/10.1002/jmri.1076>.

Le Bihan, D. (2003) 'Looking into the functional architecture of the brain with diffusion MRI', *Nat. Rev. Neurosci*, 4(6), pp. 469–480. Available at: <https://doi.org/10.1038/nrn1119>.

Le Bihan, D. and van Zijl, P. (2002) 'From the diffusion coefficient to the diffusion tensor', *NMR in biomedicine*, 15(7–8), pp. 431–434. Available at: <https://doi.org/10.1002/nbm.798>.

Leal, P.R.L. *et al.* (2019) 'Diffusion tensor imaging abnormalities of the trigeminal nerve root in patients with classical trigeminal neuralgia: a pre- and postoperative comparative study 4 years after microvascular decompression', *Acta Neurochirurgica*, 161(7), pp. 1415–1425. Available at: <https://doi.org/10.1007/s00701-019-03913-5>.

Liu, F. *et al.* (2011) 'Noninvasive evaluation of endolymphatic space in healthy volunteers using magnetic resonance imaging', *Acta Oto-Laryngologica*, 131(3), pp. 247–257. Available at: <https://doi.org/10.3109/00016489.2010.524938>.

- Logothetis, N.K. (2003) 'MR imaging in the non-human primate: studies of function and of dynamic connectivity.', *Current opinion in neurobiology*, 13(5), pp. 630–642. Available at: <https://doi.org/10.1016/j.conb.2003.09.017>.
- Lopez, C. and Blanke, O. (2011) 'The thalamocortical vestibular system in animals and humans', *Brain Research Reviews*, 67(1–2), pp. 119–146. Available at: <https://doi.org/10.1016/j.brainresrev.2010.12.002>.
- Lopez, C., Blanke, O. and Mast, F.W. (2012) 'The human vestibular cortex revealed by coordinate-based activation likelihood estimation meta-analysis', *Neuroscience*, 212, pp. 159–179. Available at: <https://doi.org/10.1016/j.neuroscience.2012.03.028>.
- Lopez, C., Halje, P. and Blanke, O. (2008) 'Body ownership and embodiment: Vestibular and multisensory mechanisms', *Neurophysiologie Clinique*, 38(3), pp. 149–161. Available at: <https://doi.org/10.1016/j.neucli.2007.12.006>.
- Markowski, J. et al. (2011) 'Assessment of vestibulocochlear organ function in patients meeting radiologic criteria of vascular compression syndrome of vestibulocochlear nerve--diagnosis of disabling positional vertigo', *Medical Science Monitor: International Medical Journal of Experimental and Clinical Research*, 17(3), pp. CR169-173. Available at: <https://doi.org/10.12659/msm.881452>.
- Merboldt, K.-D., Hanicke, W. and Frahm, J. (1985) 'Self-diffusion NMR imaging using stimulated echoes', *Journal of Magnetic Resonance (1969)*, 64(3), pp. 479–486. Available at: [https://doi.org/10.1016/0022-2364\(85\)90111-8](https://doi.org/10.1016/0022-2364(85)90111-8).
- Merfeld, D.M., Zupan, L. and Peterka, R.J. (1999) 'Humans use internal models to estimate gravity and linear acceleration', *Nature*, 398(6728), pp. 615–618. Available at: <https://doi.org/10.1038/19303>.
- Mittelstaedt, H. (1999) 'The role of the otoliths in perception of the vertical and in path integration', *Annals of the New York Academy of Sciences*, 871, pp. 334–344. Available at: <https://doi.org/10.1111/j.1749-6632.1999.tb09196.x>.
- Møller, A.R. (1991) 'The cranial nerve vascular compression syndrome: II. A review of pathophysiology', *Acta Neurochirurgica*, 113(1–2), pp. 24–30. Available at: <https://doi.org/10.1007/BF01402110>.
- Naganawa, S. et al. (2008) 'Separate visualization of endolymphatic space, perilymphatic space and bone by a single pulse sequence; 3D-inversion recovery imaging utilizing real reconstruction after intratympanic Gd-DTPA administration at 3 Tesla', *European Radiology*, 18(5), pp. 920–924. Available at: <https://doi.org/10.1007/s00330-008-0854-8>.
- Naganawa, S. et al. (2013) 'Imaging of Ménière's disease after intravenous administration of single-dose gadodiamide: Utility of multiplication of MR cisternography and HYDROPS image', *Magnetic Resonance in Medical Sciences*, 12(1), pp. 63–68. Available at: <https://doi.org/10.2463/mrms.2012-0027>.
- Nakashima, T. et al. (2007) 'Visualization of endolymphatic hydrops in patients with Meniere's disease', *Laryngoscope*, 117(3), pp. 415–420. Available at: <https://doi.org/10.1097/mlg.0b013e31802c300c>.
- Nakashima, T. et al. (2009) 'Grading of endolymphatic hydrops using magnetic resonance imaging.', *Acta otolaryngologica. Supplementum*, (560), pp. 5–8. Available at: <https://doi.org/10.1080/00016480902729827>.
- Ogawa, S. et al. (1990) 'Brain magnetic resonance imaging with contrast dependent on blood oxygenation.', *Proceedings of the National Academy of Sciences*, 87(24), pp. 9868–9872. Available at: <https://doi.org/10.1073/pnas.87.24.9868>.
- Ogawa, Seiji et al. (1990) 'Oxygenation-sensitive contrast in magnetic resonance image of rodent brain at high magnetic fields', *Magnetic Resonance in Medicine*, 14(1), pp. 68–78. Available at: <https://doi.org/10.1002/mrm.1910140108>.
- Ogawa, S. et al. (1993) 'Functional brain mapping by blood oxygenation level-dependent.', *Biophys*, 64(3), pp. 803–12.
- Ogawa, S. and Lee, T. -M (1990) 'Magnetic resonance imaging of blood vessels at high fields: In vivo and in vitro measurements and image simulation', *Magnetic Resonance in Medicine*, 16(1), pp. 9–18. Available at: <https://doi.org/10.1002/mrm.1910160103>.
- Okazaki, Y. et al. (2017) 'Significance of Endolymphatic Hydrops in Ears With Unilateral Sensorineural Hearing Loss',

- Otology & Neurotology*, 38(8), p. 1076. Available at: <https://doi.org/10.1097/mao.0000000000001499>.
- Parnes, L.S. *et al.* (1990) 'Vascular relationships of the vestibulocochlear nerve on magnetic resonance imaging.', *The American journal of otology*, 11(4), pp. 278–281.
- Pauling, L. and Coryell, C.D. (1936) 'The Magnetic Properties and Structure of Hemoglobin, Oxyhemoglobin and Carbonmonoxyhemoglobin', *Proceedings of the National Academy of Sciences*, 22(4), pp. 210–216. Available at: <https://doi.org/10.1073/pnas.22.4.210>.
- Pierpaoli, C. *et al.* (1996) 'Diffusion tensor MR imaging of the human brain', *Radiology*, 201(3), pp. 637–648. Available at: <https://doi.org/10.1148/radiology.201.3.8939209>.
- Pierpaoli, C. and Basser, P.J. (1996) 'Toward a quantitative assessment of diffusion anisotropy', *Magnetic Resonance in Medicine*, 36(6), pp. 893–906. Available at: <https://doi.org/10.1002/mrm.1910360612>.
- Pozzo, T., Berthoz, A. and Lefort, L. (1990) 'Head stabilization during various locomotor tasks in humans. I. Normal subjects.', *Experimental brain research*, 82(1), pp. 97–106. Available at: <https://doi.org/10.1007/bf00230842>.
- Radue, E.-W. *et al.* (2016) 'Introduction to Magnetic Resonance Imaging for Neurologists', *CONTINUUM: Lifelong Learning in Neurology*, 22(5), pp. 1379–1398. Available at: <https://doi.org/10.1212/con.0000000000000391>.
- Rojoa, D. *et al.* (2021) 'Meta-analysis of the normal diffusion tensor imaging values of the median nerve and how they change in carpal tunnel syndrome', *Scientific Reports*, 11(1), p. 20935. Available at: <https://doi.org/10.1038/s41598-021-00353-z>.
- Salt, A.N. and Plontke, S.K. (2010) 'Endolymphatic hydrops: pathophysiology and experimental models', *Otolaryngologic Clinics of North America*, 43(5), pp. 971–983. Available at: <https://doi.org/10.1016/j.otc.2010.05.007>.
- Sano, R. *et al.* (2012) 'Contrast enhancement of the inner ear in magnetic resonance images taken at 10 minutes or 4 hours after intravenous gadolinium injection', *Acta Oto-Laryngologica*, 132(3), pp. 241–246. Available at: <https://doi.org/10.3109/00016489.2011.639085>.
- Schneider, F. and Fink, G.R. (2013) *Funktionelle MRT in Psychiatrie und Neurologie*. Available at: <https://doi.org/10.1007/978-3-642-29800-4>.
- Schwarz, D.W. (1976) 'Clinically relevant physiology of the vestibulo-ocular reflex', *The Journal of Otolaryngology*, 5(5), pp. 425–436.
- Sivaranan, N. *et al.* (2019) 'MRI findings in vestibular paroxysmia - An observational study', *Journal of Vestibular Research: Equilibrium & Orientation*, 29(2–3), pp. 137–145. Available at: <https://doi.org/10.3233/ves-190661>.
- Smith, P.F., Darlington, C.L. and Zheng, Y. (2010) 'Move it or lose it - Is stimulation of the vestibular system necessary for normal spatial memory?', *Hippocampus*, 20(1), pp. 36–43. Available at: <https://doi.org/10.1002/hipo.20588>.
- Smith, S.M. *et al.* (2009) 'Correspondence of the brain's functional architecture during activation and rest', *Proceedings of the National Academy of Sciences*, 106(31), pp. 13040–13045. Available at: <https://doi.org/10.1073/pnas.0905267106>.
- Straube, A. and Brandt, T. (1987) 'Importance of the visual and vestibular cortex for self-motion perception in man (circularvection)', *Human Neurobiology*, 6(3), pp. 211–218.
- Strupp, M. *et al.* (2013) 'Teaching NeuroImages: Compression of the eighth cranial nerve causes vestibular paroxysmia', *Neurology*, 80(7). Available at: <https://doi.org/10.1212/wnl.0b013e318281cc2c>.
- Strupp, M. *et al.* (2017) 'Vestibular paroxysmia: Diagnostic criteria', *Journal of Vestibular Research: Equilibrium and Orientation*, 26(5–6), pp. 409–415. Available at: <https://doi.org/10.3233/ves-160589>.
- Taylor, D.G. and Bushell, M.C. (1985) 'The spatial mapping of translational diffusion coefficients by the NMR imaging technique', *Physics in Medicine and Biology*, 30(4), pp. 345–349. Available at: <https://doi.org/10.1088/0031-9155/30/4/009>.
- Thulborn, K.R. *et al.* (1982) 'Oxygenation dependence of the transverse relaxation time of water protons in whole blood at high field', *BBA - General Subjects*, 714(2), pp. 265–270. Available at:

4165(82)90333-6.

Vallar, G. *et al.* (1993) 'Exploring somatosensory hemineglect by vestibular stimulation', *Brain*, 116(3), p. 756. Available at: <https://doi.org/10.1093/brain/116.3.756>.

Van Essen, D.C. and Glasser, M.F. (2014) 'In vivo architectonics: A cortico-centric perspective', *NeuroImage*, 93, pp. 157–164. Available at: <https://doi.org/10.1016/j.neuroimage.2013.04.095>.

Wenzel, R. *et al.* (1996) 'Deactivation of human visual cortex during involuntary ocular oscillations. A PET activation study.', *Brain : a journal of neurology*, 119 (Pt 1, pp. 101–110. Available at: <https://doi.org/10.1093/brain/119.1.101>.

Wolbarsht, M.L. (1966) 'Structure and Function in the Nervous Systems of Invertebrates. Volumes 1 and 2. Theodore Holmes Bullock, G. Adrian Horridge', *The Quarterly Review of Biology*, 41(2), pp. 242–242. Available at: <https://doi.org/10.1086/405046>.

Yang, Y. *et al.* (2011) 'Binocular Disparity Tuning and Visual-Vestibular Congruency of Multisensory Neurons in Macaque Parietal Cortex', *Journal of Neuroscience*, 31(49), pp. 17905–17916. Available at: <https://doi.org/10.1523/jneurosci.4032-11.2011>.

Yuan, X. *et al.* (2022) 'Microstructural changes of the vestibulocochlear nerve in patients with Ménière's disease using diffusion tensor imaging', *Frontiers in Neurology*, 13, p. 915826. Available at: <https://doi.org/10.3389/fneur.2022.915826>.

Zu Eulenburg, P. *et al.* (2012) 'Meta-analytical definition and functional connectivity of the human vestibular cortex', *NeuroImage*, 60(1), pp. 162–169. Available at: <https://doi.org/10.1016/j.neuroimage.2011.12.032>.

Zwergal, A. *et al.* (2009) 'Parallel ascending vestibular pathways: Anatomical localization and functional specialization', *Annals of the New York Academy of Sciences*, 1164, pp. 51–59. Available at: <https://doi.org/10.1111/j.1749-6632.2009.04461.x>.

Abbildungsverzeichnis

Abbildung 1: Das Innenohr besteht neben der Cochlea aus den drei Bogengängen sowie dem Sakkulus und Utrikulus. In Anlehnung an Abb. 14.19 aus (Feigenspan, 2017).	8
Abbildung 2: Lage und Anordnung der Bogengänge. Beachtenswert ist, dass der anteriore Bogengang der einen Seite in einer Achse liegt mit dem posterioren Bogengang der anderen Seite. In Anlehnung an (Fetter, 2010).	9
Abbildung 3: Die Auslenkung der Stereozilien in Richtung der Kinozilie führt zu einer Depolarisation, die durch eine erhöhte Glutamat Freisetzung die Aktionspotenzialfrequenz erhöht. Entgegengesetzt löst eine Hyperpolarisation eine Abnahme der Aktionspotenzialfrequenz in Vergleich zur Ruhedefrequenz aus. In Anlehnung an Abb. 14.22 aus (Feigenspan, 2017).	10
Abbildung 4: Darstellung der Makulaorgane mit den Stereozilien der Haarzellen die in die gallertartige Statolithenmembran reichen. In Anlehnung an Abb. 14.24 aus (Feigenspan, 2017).	11
Abbildung 5: Darstellung der Root-Entry-Zone des Nervus vestibulocochlearis mit Wechsel der Myelinscheide von Schwann'schen Zellen auf Oligodendrozyten. Eigene Darstellung.	11
Abbildung 6: Schematische Darstellung der komplexen Verbindungen der Nuclei vestibularis anhand des vestibulookklären Reflexes. Zu erkennen sind die Verbindungen über den Drei-Neuronen-Reflexbogen zu den Augenmuskelkernen, die Verbindungen über den Thalamus zum parieto-insulären Kortex sowie die Verbindungen entlang des Tractus vestibulospinalis für die vestibulospinalen Reflexe. In Anlehnung an Abb. 1.2 aus (Brandt, Dieterich and Strupp, 2013).	13
Abbildung 7: Darstellung der Hämoglobin Konzentrationen sowie des korrespondierenden BOLD Signals. Die Erhöhung des zerebralen Blutflusses bewirkt einen Anstieg des oxygenierten Hämoglobins. Auf der rechten Seite ist das BOLD Signal dargestellt, welches auf der Abnahme des paramagnetischen desoxygeniertem Hämoglobin basiert. In Anlehnung an Abb. 1 (Cinciute, 2019).	18
Abbildung 8: Schematische Darstellung der unabhängigen Komponentenanalyse. Die fMRT-Daten werden in einer zweidimensionalen Matrix dargestellt. Die Voxel werden als Spalten angeordnet, die Zeit als Zeilen. Mithilfe der ICA wird diese Matrix in das Produkt zweier Matrizen umgewandelt. Die eine Matrix stellt dabei die zeitlichen Verläufe der Signale dar. Die andere Matrix zeigt die Regionen, die zeitlich kohärent sind. In Anlehnung an Abb. 15.20 aus (Schneider and Fink, 2013).	19
Abbildung 9: Darstellung eines gesunden Nervens mit Myelinscheide und dichter Anordnung, wodurch die Diffusion in der Längsachse des Nervens eingeschränkt ist. Auf der rechten Seite Darstellung eines geschädigten Nervens mit veränderter Mikrostruktur und vermehrter Diffusion senkrecht zur Längsachse des Nervens. In Anlehnung an Abb. 1 (Rojoa <i>et al.</i> , 2021).	20

Danksagung

An dieser Stelle möchte ich mich bei allen herzlich bedanken, die mich bei dieser Arbeit unterstützt und begleitet haben. Zunächst gilt mein Dank Frau Prof. Dr. med. Marianne Dieterich für die Annahme dieser Arbeit als Dissertation und für die kontinuierliche Unterstützung und Förderung in der Arbeitsgruppe. Einen besonderen Dank möchte ich auch meiner Betreuerin und langjährigen Mentorin Dr. med. Valerie Kirsch für die anhaltende fachliche sowie persönliche Unterstützung aussprechen. Weiterhin möchte ich mich herzlich bei Geraldine Tauber, Johannes Gerb, Andrea Stadie und Ute Coates für die gute Zusammenarbeit bedanken.